JOHANNES GUTENBERG-UNIVERSITY MAINZ
Institute for Nuclear Physics

MASTER THESIS

Optimization of the π^0 reconstruction selections for the Belle II experiment

AUTHOR
Sebastian Stengel

SUPERVISOR
Prof. Dr. Sfienti

COSUPERVISOR
Dr. Ferber

NOVEMBER 2019

Sailing away, beyond the reach of anyone
Far beyond the dreams of everyone
No light to follow
A shot in the dark
Does anybody know?

Avenged Sevenfold

AUTHOR'S DECLARATION

Herewith I, Sebastian Stengel (Student ID: 2709673), declare that I have completed the present thesis, entitled:

"Optimization of the π^0 reconstruction selections for the Belle II experiment"

independently, making use only of the specified literature and aids; it is entirely the product of my own scholarly work, unless stated otherwise. Any inaccuracies of fact or faults in reasoning are my own and accordingly I take full responsibility. Sentences or parts of sentences quoted literally are marked as quotations; identification of other references with regard to the statement and scope of the work is quoted. The thesis in this form or in any other form has not been submitted to an examination body and has not been published.

DATE: ..... SIGNED: .....

TABLE OF CONTENTS

INTRODUCTION

The purpose of this thesis is to provide optimized selections for the π^0 reconstruction in the *Belle II analysis software framework* (basf2). basf2 provides generic selections on photons and on π^0s reconstructed via $\pi^0 \to \gamma\gamma$, which are designed to provide a certain π^0 reconstruction efficiency. The goal is to define optimized selections for 60 %, 50 %, 40 %, 30 %, 20 %, and 10 % π^0 reconstruction efficiency, the optimization criterion being the maximization of the purity of the π^0 sample.

The *Belle II* experiment is located at the *SuperKEKB* collider in Tsukuba, Japan, and is a next-generation B-factory. B-factories are particle collider experiments designed to produce a large number of B-mesons. In *Belle II*, electrons and positrons are collided at the mass of the $\Upsilon(4S)$-resonance, which is $\sim 0.2\,\%$ above the energy of two B-mesons. B-mesons have many hadronic decay channels into lighter mesons, like D-mesons or kaons, often yielding π^0s as byproducts. In fact, one third of B-meson decay products are π^0s or other neutral particles decaying into photons. This makes the π^0 reconstruction crucial for *Belle II*.

This thesis starts with a motivation for the *Belle II* experiment in the form of a summary of the Standard Model of particle physics in Chapter 1. It describes what the Standard Model can explain and where it fails to provide an explanation of physics.
Chapter 2 gives an overview of the *Belle II* experiment, the *SuperKEKB* collider and the *Belle II* subdetectors. The electromagnetic calorimeter (ECL) of the *Belle II* detector is treated in more detail in Chapter 3, since it is the subdetector of relevance to the π^0 reconstruction. Chapter 3 also explains how data from the ECL is processed in basf2 to provide suitable information for the user. This information can be interpreted as photons and is used in the π^0 reconstruction, which is explained in Chapter 4. Chapters 3 and 4 also give an overview on the photon and π^0 variables used for the π^0 reconstruction selections, respectively.
Chapter 5 describes a study on the photon and π^0 variables, investigating which variables are suitable to be used for the optimization of the π^0 reconstruction selections. Using the results from Chapter 5, Chapter 6 performs a full grid scan on the chosen variables and provides optimized suggestions for the use as new π^0 reconstruction selections.
Chapter 7 compares data and Monte Carlo for these suggestions, and Chapter 8 closes this thesis with a conclusion.

CHAPTER 1

PHYSICS MOTIVATION

The Standard Model of particle physics is the most accurate theoretical model to describe fundamental particles and how they interact. When it was developed in the early 1970s, it incorporated the knowledge about subatomic particles at the time and even predicted the existence of additional particles and processes. The Standard Model includes the description of all known fundamental particles and three of the four fundamental forces: the electromagnetic, the weak, and the strong force.

Since the gravitational force is not included in the Standard Model, one can see that the Standard Model is indeed the most accurate theory, but not a complete one. Besides gravity, there are other processes that are not included in the Standard Model as well as observations the Standard Model fails to explain.

While Section 1.1 gives a brief overview on the main aspects of the Standard Model, Section 1.2 lists some of the phenomena that are not explained by it.

1.1 The Standard Model

The Standard Model of particle physics is based on two basic ideas: matter is made of fundamental particles, where 'fundamental' means having no internal structure, and these particles interact by exchanging other particles associated with the fundamental forces. It includes the description of the electromagnetic, the weak, and the strong interaction as well as the *Higgs mechanism*, which is responsible for giving the fundamental particles their mass.

The theory of the electromagnetic force (*quantum electrodynamics*, QED) and the description of the weak interaction got merged by Sheldon Glashow in 1961. Once Steven Weinberg and Abdus Salam were able to add the *Higgs mechanism* in 1967, the *electroweak theory* was born.

After combining the electroweak theory with the theory of the strong interaction (*quantum chromodynamics*, QCD) in 1975, Abraham Pais and Sam Treiman gave the Standard Model its modern form.

The fundamental particles that form matter are *fermions* and the force-exchanging particles as well as the Higgs particle are *bosons*. These terms refer to their spin, which can be described as an internal angular momentum of the particle. While fermions have a half-integer spin (in units of the reduced Planck constant $\hbar$), bosons carry integer spin. Every particle also has an anti-particle with the same mass but opposite electric charge. Figure 1.1 shows all fundamental particles (anti-particles are not pictured).

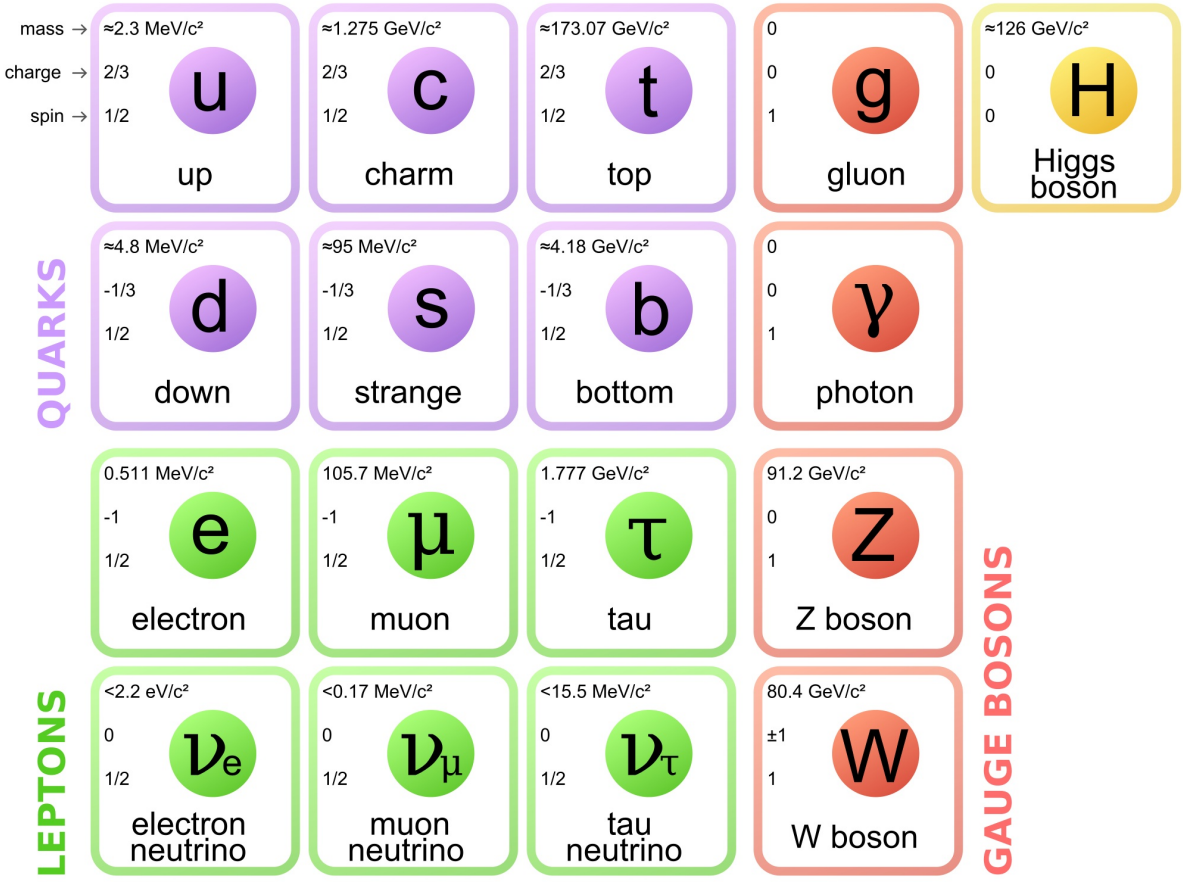

FIGURE 1.1. Fundamental particles included in the Standard Model. Quarks, leptons, and the bosons are color-coded. The first three columns show the three fermion generations, the fourth column lists the force carriers, and the fifth column contains the Higgs boson. For every particle its mass, charge, and spin is given. Figure from [1].

The fermions of the Standard Model can be classified into two families, where both of them contain six particles: the leptons and the quarks. The quark family is made of the up- (u), down- (d), charm- (c), strange- (s), top- (t), and bottom-quark (b). The lepton family contains the electron (e), the muon (μ), and the tau (τ), as well as the corresponding neutrinos (ν_e, ν_μ, ν_τ). Furthermore both families can be divided into three generations of particles. The particles of different generations only differ in mass, all other physical properties are equal. Remarkably, all visible matter in the universe is made of first generation particles.

The six quarks interact via all of the three mentioned interactions. In addition to its *flavor* (u, d, c, s, t or b), a quark carries a *color*, which represents the charge of the strong interaction. The phenomenon that quarks are never observed alone but only in bound states is called *color confinement* and leads to three different colors. In a bound state, the color charges of the single quarks add up to zero. This can be achieved by combining a quark and its anti-quark, which yields a *meson*, or by combining three quarks (or three anti-quarks) of different color, which yields a *baryon*. But also combinations of more quarks are possible. In fact particles made of four (*tetraquarks*) or five (*pentaquarks*) quarks have recently been observed by the Belle and LHCb experiments [2–5].

Quarks also have an electric charge, where in each generation there is one quark with an electric charge of $+\frac{2}{3}$ (in units of the elementary charge e) and one with an electric charge of $-\frac{1}{3}$.

The six leptons do not interact via the strong interaction. The electron, muon, and tau interact electromagnetically and weakly, the three neutrinos in contrast only interact via the weak force. The electromagnetic charge of the electron, muon and tau is -1, respectively.

All fermions in the Standard Model as well as their anti-particles have spin $\frac{1}{2}$.

The gauge bosons are the force carriers of the three fundamental interactions included in the Standard Model and all of them have spin 1.

The *gluon* mediates the strong interaction and is the only boson in the Standard Model with color charge. It comes in 8 different color combinations (due to the underlying SU(3) symmetry which is 8-dimensional) and has no electromagnetic charge.

The *photon* carries the electromagnetic force, is massless, and has no electromagnetic charge.

The weak interaction is represented by two bosons: the *W-boson* and the *Z-boson*. Both of them carry mass, but only the W-boson has an electromagnetic charge.

The last particle is the *Higgs-boson* which is a scalar boson (spin 0) with no electromagnetic charge. Due to the interaction with the Higgs-boson, the other massive fundamental particles gain their mass which is described by the Higgs-mechanism.

1.2 Beyond the Standard Model

The Standard Model is able to explain almost every result in particle physics, but some important questions remain unanswered and several processes and observations are still unexplained.

Unanswered questions are: Why are there three different generations of particles that only differ in mass? Why does nature need two more generations when all visible matter is made of up-quarks, down-quarks and electrons?
Why is the Standard Model described by 19 constant parameters (masses and coupling constants) which have unrelated and arbitrary values? Why are the values of the constant parameters the way we measure them and not different?

The major gap in the Standard Model is that it does not contain gravity. All attempts of combining the Standard Model with the theoretical description of gravity (*general theory of relativity*) failed so far. Also not included in the Standard Model is the observation of *neutrino-oscillation*. When a neutrino oscillates, it changes its flavour (electron-, muon- or tau-neutrino) and to do so, it needs to carry mass, while the Standard Model considers neutrinos as massless particles.

Another observation the Standard Model fails to explain is the *matter-antimatter asymmetry* in the universe. Theoretically, matter and antimatter should occur in equal amounts in the universe, if there is no process that treats matter and antimatter differently. Up to now there is no mechanism in the Standard Model that sufficiently explains this asymmetry.

As if that were not enough, there are the concepts of *dark matter* and *dark energy*. Cosmological observations [6–8] indicate that the visible matter in our universe (the matter interacting with photons) is not the only form of matter but that there is a different kind. While visible matter makes up $\sim 5\%$ of universe´s energy density, dark matter is responsible for $\sim 26\%$. The remaining $\sim 69\%$ come in form of dark energy, which is considered as a constant energy density for the vacuum, that leads to the accelerating expansion of the universe. While there is no explanation for dark energy yet, there are several attempts to describe dark matter: *WIMPs* (weakly interacting massive particles) [9], *ALPs* (axion-like particles) [10], *sterile neutrinos* [11], as well as some more. Further detail is beyond the scope of this thesis, but can be found in the references provided.

CHAPTER 2

THE BELLE II EXPERIMENT

The occurence of *CP-violation* is said to be the central element in describing the matter-antimatter asymmetry in the universe. After this asymmetry was first discovered in certain decays of neutral K-mesons by James Cronin and Val Fitch in 1964 [12], it has been observed by the *BaBar* and *Belle* experiments in B-meson decays [13–15] as well as in the decays of D-mesons [16].

These two famous experiments belong to the class of *B-factories*, which are particle collider experiments designed to produce and detect a large number of B-mesons. Both of them collide electrons and positrons at the mass of the $\Upsilon(4S)$-resonance at roughly 10.58 GeV which is just enough energy to create two B-mesons. Since there are no other particles produced, all the tracks and clusters in an event can be assigned to one B-meson or the other meaning a clean, low-background environment. To make a statement about the CP-violation, the order in which the two B-mesons decay must be known. But since the B-mesons at a symmetric $\Upsilon(4S)$ accelerator are almost produced at rest, the distance they travel before they decay is too short to be accurately resolved. One can circumvent this issue by inducing an asymmetric collision in which the produced B-mesons are boosted along one axis and therefore travel a longer distance before they decay. Of course this yields other problems like requiring two separate beam pipes for electrons and positrons respectively and a more complicated interaction region.

Yet *BaBar* and *Belle* took on this challenge in the 1990s resulting in lots of important publications during and after their operation. While the *BaBar* experiment ceased operation in 2008, the *Belle* experiment got upgraded to *Belle II* which runs at a 40 times higher peak luminosity than its predecessor. The challenges associated with this upgrade, the underlying electron-positron collider *SuperKEKB* and the *Belle II* detector itself are described in the following sections.

2.1 From Belle to Belle II

The dominant reason for the upgrade from *KEKB* and *Belle* to *SuperKEKB* and *Belle II* is an increase in peak luminosity by a factor of 40. This enormous change has an impact on the experiment. While section 2.1.1 treats the luminosity upgrade and how it is achieved theoretically, section 2.1.2 describes the problems associated with the upgrade and its technical realization.

2.1.1 Luminosity Upgrade

The luminosity L of a collider is expressed by

$$L = \frac{\gamma_\pm}{2er_e}\left(\frac{I_\pm \xi_{y\pm}}{\beta^*_{y\pm}}\right)\left(\frac{R_L}{R_{\xi_y}}\right) \quad , \tag{2.1}$$

where γ is the Lorentz factor, e is the elementary electric charge, r_e is the classical electron radius, I is the beam current, ξ_y is the vertical beam-beam parameter, β^*_y is the vertical beta function, and R_L and R_{ξ_y} represent reduction factors for the luminosity and the vertical beam-beam parameter. The suffix $\pm$ specifies the positron (+) and the electron (-).
The ratio of R_L and R_{ξ_y} is usually not far from unity and therefore the luminosity L is mainly determined by the beam current I, the vertical beam-beam parameter ξ_y, and the vertical beta function β_y meaning that the desired value for the luminosity can be tuned using these three parameters.

The target peak luminosity at *SuperKEKB* is $8 \times 10^{35}\,\mathrm{cm}^{-2}\mathrm{s}^{-1}$. To achieve this, it was decided that the vertical beam-beam parameter ξ_y shall roughly stay the same, while the beam current I shall be doubled and the vertical beta function β_y shall be decreased by a factor 20 using a *Nano-Beam* scheme. Table 2.1 shows the choice of the three parameters for *SuperKEKB* compared to the values at former *KEKB*. The peak luminosity and the beam energies are also shown.

	KEKB achieved	SuperKEKB design
Energy [GeV] (+/-)	3.5/8.0	4.0/7.0
ξ_y (+/-)	0.129/0.090	0.090/0.088
β^*_y [mm] (+/-)	5.9/5.9	0.27/0.41
I [A] (+/-)	1.64/1.19	3.60/2.62
L [$10^{34}\,\mathrm{cm}^{-2}\mathrm{s}^{-1}$]	2.11	80

TABLE 2.1. Collider parameters for *KEKB* and *SuperKEKB*. Except for the luminosity L, two values per accelerator are given: One for the positron beam (+) and one for the electron beam (-). Values taken from [17].

The schedule for the peak luminosity and the integrated luminosity can be found in Figure 2.1. More details on the *Nano-Beam* scheme, how the three parameters are exactly determined and what changes to the *KEKB* collider setup this entails can be found in [17].

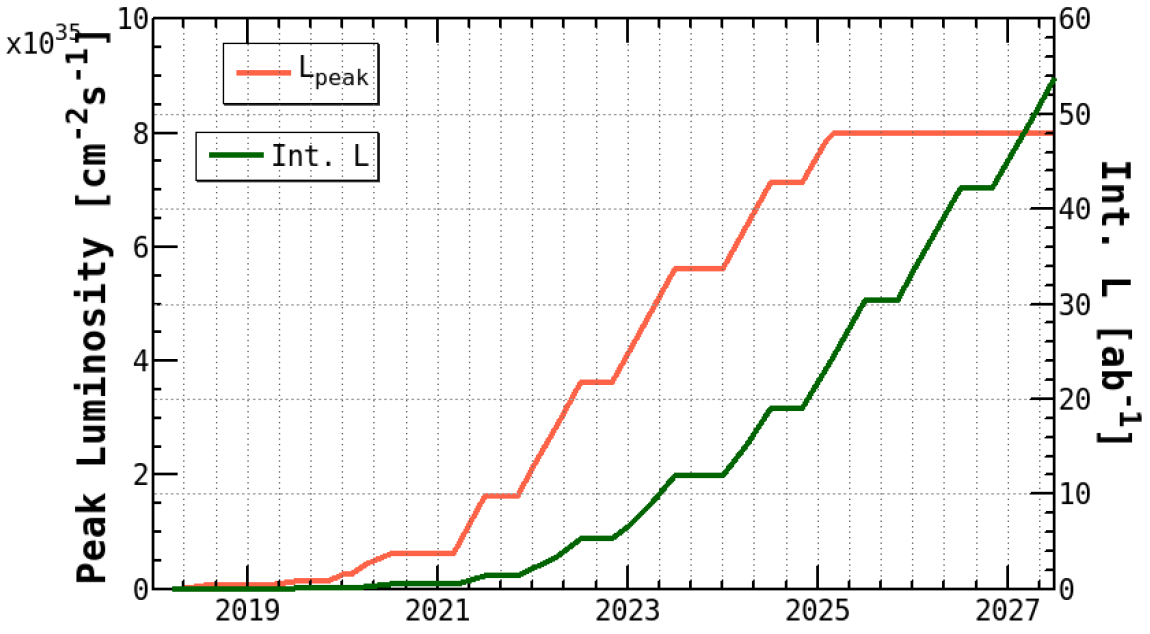

FIGURE 2.1. Schedule for the luminosity reached at SuperKEKB. Peak luminosity is visualized in orange, integrated luminosity in green. Figure taken from [18].

2.1.2 Beam-related background and changes to the Belle detector

The peak luminosity increase by a factor 40 from *KEKB* to *SuperKEKB* is accompanied by a large increase of beam-related background. This does not only yield higher expected background rates but also means that major changes to the experiment's setup are inevitable.

The main sources for beam-related background are briefly described in the following, further information can be found in [17, 19, 20].

- **Touschek scattering** is the Coulomb scattering of two particles from the same beam. After interacting, one particle ends up with a higher than nominal, and the other one with a lower than nominal energy. Thus the two particles do not fit the trajectory requirements anymore and are lost. Depending on their location, the particles may hit some material and cause additional electromagnetic showers or enter the detector region directly. The first case is treated with vertical and horizontal collimators located at various positions around the storage ring. Heavy-metal shields are placed in the VXD volume to mitigate the effect of the second.

- **Beam-gas scattering:** Since a vacuum is never perfect, residual gas molecules will be present in the beam pipe. The scattering of a beam particle on one of these molecules occurs in two ways: Coulomb scattering and Bremsstrahlung. The first one causes the beam

particle to change its direction, while the second one results in an energy change of the beam particle and the emission of a photon. The Coulomb-scattered beam particles are comparable with the Touschek-scattered particles and therefore treated by the same countermeasures, collimators and heavy-metal shields. The rate of the Bremsstrahlung particles is negligible compared to the rate of Touschek-scattered particles, thus no additional countermeasures are applied for these.

- **Synchrotron radiation** occurs if a charged particle is radially accelerated. Thus it is a special form of Bremsstrahlung and proportional to the beam pipe curvature and amount of injected particles. To counteract this, the interaction region of *Belle II* is designed to avoid direct hits of Synchrotron radiation. First, ridge structures are placed on the inner surface of the incoming pipes and second, the inner surface of the beryllium beampipe is coated with a gold layer. Additionally, the incoming electron and positron beams are nearly on the magnetic axes of the quadrupole magnets, which reduces the emission of Synchrotron radiation.

- **Radiative-Bhabha process:** The process $e^+e^- \to e^+e^-\gamma$ is the most important background source in most of the sub-detectors and is proportional to the luminosity of the collider. The particles travel approximately along the beam line and interact with the iron of the accelerator magnets. This yields low-energy photons and neutrons entering the detector. Additionally, the beam particles lose energy and thus hit the beam pipe, which results in unwanted electromagnetic showers. To mitigate this effect, the incoming and outgoing beams have their own quadrupole magnets, respectively. To reduce the neutron rate, additional neutron shielding is placed in the accelerator tunnel.

- **Two-photon process:** The process $e^+e^- \to \gamma\gamma \to e^+e^-e^+e^-$ is also proportional to the collider's luminosity. The created e^+e^- pairs have very low momentum and therefore can spiral around the solenoid filed lines leaving multiple hits in the detectors. Furthermore the primary e^+e^- pairs that lose much energy or scatter at large angles are lost and result in unwanted electromagnetic showers.

- **Injection background:** This background occurs when a charge is injected to a circulating beam bunch. The bunch is perturbed by the injection yielding a short background rise.

Due to these background sources, the background-level at *SuperKEKB* is expected to be significantly higher than at *KEKB*. Therefore, several changes were made to the *Belle* detector. The key changes are listed in the following. More details can again be found in [17, 19, 20].

- Due to the Nano-Beam scheme, the beam pipe radius at the interaction point has been reduced from 15 mm to 10 mm. Thus, the vertex detector could be placed closer to the interaction point.

- The innermost part of the old silicon strip detector has been replaced with a two-layer pixel detector and the rest of it has been extended to have a larger radius.

- The volume of the central drift chamber has been enlarged and its cell sizes have been reduced. Also new readout electronics are used for the central drift chamber to handle the higher trigger rates.

- The particle identification system has been upgraded using Cherenkov imaging besides the use of new electronics.

- The electronics of the electromagnetic calorimeter have been upgraded.

- Parts of the resistive plate chambers (RPCs) in the K_L and μ detector have been replaced with scintillators.

In order to handle the development of such a large project like *Belle II*, its lifetime is divided into three phases:

Phase 1 The beam commissioning phase ran from February to June 2016. In this period, beam background measurements were taken with the *BEAST II* detector [19].

Phase 2 From February to July 2018, the collision of the two beams was tuned. Therefore, the *Belle II* detector was in place except for the vertex detector. Calibration data was taken.

Phase 3 The final phase of *Belle* II started in April 2019. This is the full physics run with the whole detector installed. At the time of writing this thesis, the VXD is only partly installed. This will be fixed in the next long enough collider shut-down.

2.2 The SuperKEKB accelerator

Located at the KEK laboratory in Tsukuba, Japan, the electron-positron collider *SuperKEKB* is meant to herald the start of the second-generation B-factory era as the upgrade of the former *KEKB* accelerator. It operates at a center of mass energy of 10.58 GeV which is slightly above the $\Upsilon(4S)$ resonance and aims at a peak luminosity of $8 \times 10^{35}\,\mathrm{cm}^{-2}\mathrm{s}^{-1}$ as well as an integrated luminosity of $50\,\mathrm{ab}^{-1}$. Figure 2.2 schematically shows the *SuperKEKB* collider. It can be separated into two major parts: the linear preaccelerator and the storage ring which includes the electron ring (HER, high energy ring) and the positron ring (LER, low energy ring).

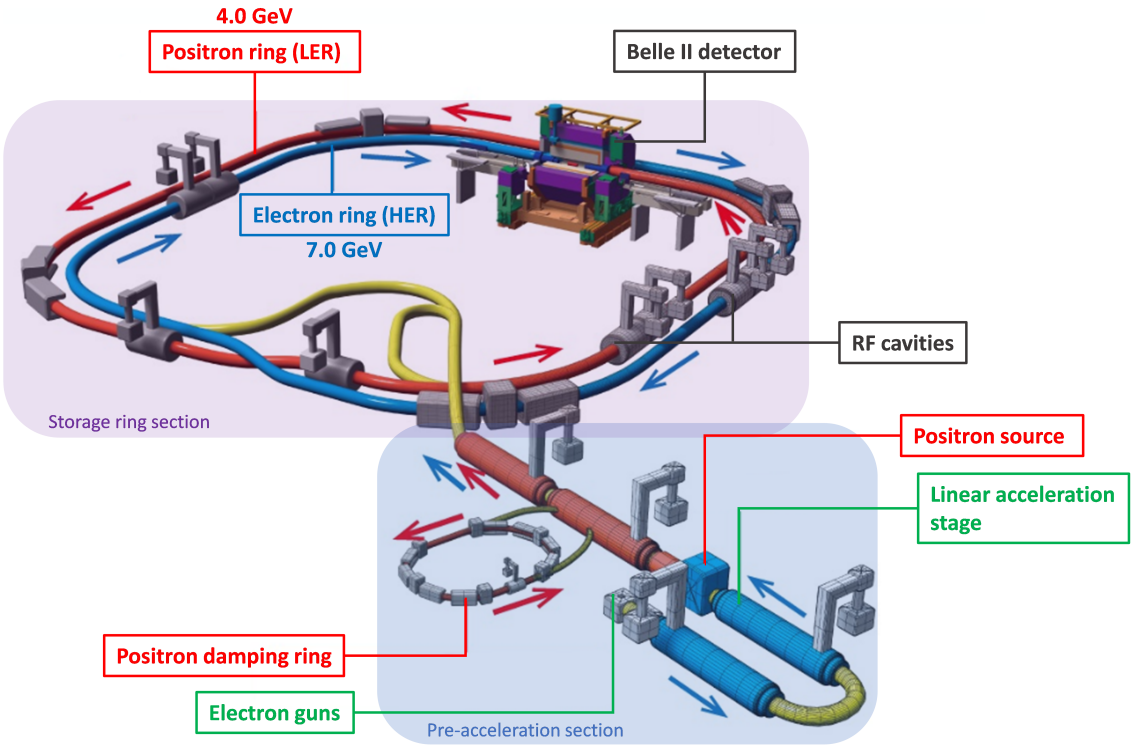

FIGURE 2.2. Schematic figure of the *SuperKEKB* electron-positron-collider. Figure adapted from [21].

The preaccelerator section starts with two different electron guns. One of them produces the electrons that are later on injected into the HER, the other one delivers higher intensity electrons for the production of the positrons directed to the LER. After being emitted by the electron guns, the electrons first go through a J-shaped acceleration stage followed by a linear acceleration stage and the positron source. The electrons that are meant to enter the HER skip this positron source and are accelerated to 7 GeV by a row of consecutive linear acceleration stages before they are injected into the HER. The higher energy electrons enter the positron source with 4 GeV and irradiate a tungsten target to generate positrons. These positrons are then accelerated to 1 GeV and enter a damping ring which reduces their emittance. Following this, the positrons are accelerated to 4 GeV and injected into the LER. The acceleration of the positrons happens by the same consecutive linear acceleration stages by which the HER electrons are accelerated.

The storage ring section is composed of the HER and the LER which both have a circumference of 3 km. Each of them is equipped with radiofrequency (RF) cavities to keep the electron and positron beam energies at 7 GeV and 4 GeV, respectively. The beams are then collided with a crossing angle of 83 mrad in the center of the Belle II detector.

More detailed information on the *SuperKEKB* collider can be found in [17].

2.3 The Belle II detector

The *Belle II* detector is the centerpiece of the experiment. It has a size of 7 m x 7.5 m and can be divided into three acceptance regions: the forward end-cap (FWD), the barrel (BRL) and the backward end-cap (BWD). The detector is built to measure the properties of all final state particles produced in the e^+e^--collisions except for neutrinos. Since this affects many different particles, various detection strategies are applied. Therefore, the *Belle II* detector is an interaction of the five following sub-detectors of which each fulfills a certain task: The vertex detectors (VXD), the central drift chamber (CDC), the particle identification (PID), the electromagnetic calorimeter (ECL) and the K_L and μ detector (KLM). Each of these sub-detectors has several functions, which will be explained in the following. More detailed information on the *Belle II* detector and its sub-detectors can be found in [17].

- **VXD:** The main purpose of the vertex detectors is to measure the vertices of the two B-meson decays per event for the measurement of mixing-induced CP asymmetry. The vertex detectors are also able to reconstruct low-p_t tracks, down to a few tens of MeV/c, that do not leave enough (or any) hits in the CDC. The vertex detectors are the pixel detector (PXD) and the silicon vertex detector (SVD).
  The PXD is made of two layers of sensors based on the DEPFET (DEPleted Field Effect Transistor) technology where the inner layer consists of 8 and the outer layer of 12 sensors. The SVD surrounds the PXD and consists of four layers of double-sided silicon strip detectors with 187 sensors in total. In addition to B-meson decays, the SVD measures vertex information in the decays of D-mesons and τ-leptons and is also able to reconstruct K_S mesons that decay outside of the PXD volume.

- **CDC:** The CDC is placed around the SVD and plays three major roles. First, it is responsible for the reconstruction of charged tracks and the precise measurement of the momenta of these tracks. Second, it provides particle identification information by measuring the energy loss of tracks within its gas volume. Therefore tracks that do not reach the PID can be identified using only the information known from the CDC. Finally, it delivers efficient and reliable trigger signals for charged particles.
  The CDC is built of more than 14 thousand sense wires and more than 42 thousand field wires arranged in 56 layers and filled with a $50:50$ mixture of helium (He) and ethane (C_2H_6). In order to supply a 1.5 T magnetic field for the CDC, a superconducting solenoid surrounds the ECL. Together with the VXD, the CDC makes up the tracking system of Belle II.

- **PID:** The PID has the task to separate between kaons and pions but also to differentiate between pions, muons and electrons in the low-energy region. It consists of two components: the TOP (time of propagation) detector in the barrel region and the ARICH (aerogel ring imaging Cherenkov) detector located in the forward-endcap.

- **ECL:** The main task of the ECL is the absorption and therefore detection of electromagnetic showers with high efficiency as well as the precise determination of the shower energy and angular coordinates. Since one third of B-meson decay products are π^0's or other neutral particles that decay into photons, the ECL is the instrument for the neutral reconstruction in Belle II. It also identifies electrons providing additional information to the information measured with the tracking system, and together with the KLM detector also K_L^0 mesons. Furthermore it generates a proper signal for the triggers and serves as an online and offline luminosity monitor. The ECL is described in more detail in Chapter 3.
- **KLM:** The KLM detector is supposed to identify K_L^0 mesons and muons. It consists of an alternating sandwich structure of detector components and 4.7 cm thick iron plates in between. The iron plates serve as the magnetic flux return for the solenoid and provide additional interaction length for the K_L^0 mesons to shower hadronically. Since resistive plate chambers are not efficient enough in some KLM regions (the amount of background is just too high), scintillators are used as detectors in the end-caps as well as in the first two layers in the barrel. The remaining layers in the barrel are equipped with RPCs.

A cross-section of the *Belle II* detector with labeled sub-detectors can be seen in Figure 2.3.

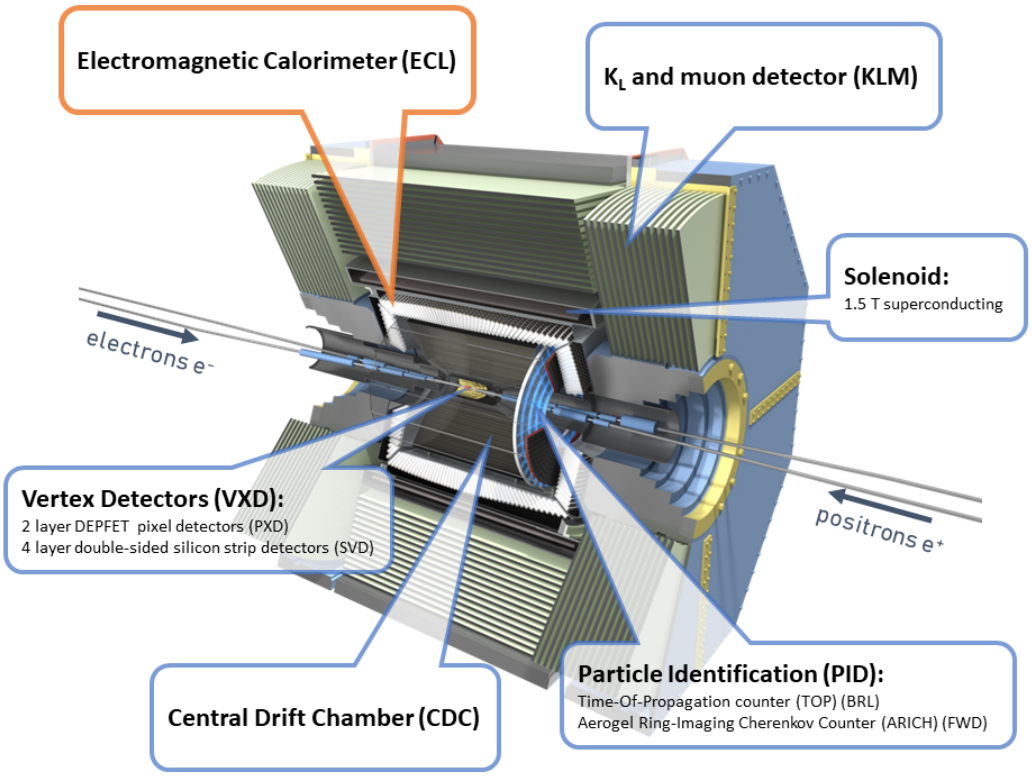

FIGURE 2.3. Cross-section of the *Belle II* detector. The single sub-detectors are labeled. Figure adapted from [21].

CHAPTER 3

FROM THE ECL TO THE PHOTON VARIABLES IN BASF2

The *Belle II electromagnetic calorimeter* (ECL) is the most important piece of the *Belle II* detector concerning the reconstruction of π^0s and therefore this thesis. In order to present the study that has been performed for this thesis in a proper and understandable way, this Chapter is organized as follows. Section 3.1 describes the ECL in more detail, while Section 3.2 treats how data from the ECL makes its way to and through the *Belle II analysis software framework* (basf2). Section 3.3 gives an overview on the photon variables that have been used for this thesis and Section 3.4 closes this chapter with the current generic photon selections that are implemented in basf2.

3.1 The Belle II electromagnetic calorimeter

The ECL serves several tasks:

- detection of electromagnetic showers with high efficiency;
- determination of the shower energy and angular coordinates;
- separation of electrons and hadrons;
- K_L^0 detection together with the KLM detector;
- generation of a trigger signal;
- online and offline luminosity measurements.

To fulfil these tasks, the ECL has to be a hermetic detector that fully covers the interaction point, except for the regions close to the beam pipe which host the vertex detectors, accelerator material, and cables. Therefore the ECL covers the whole polar angle region from 12.4° to 155.1°.

The ECL is comprised of three regions: the barrel (BRL), the forward endcap (FWD), and the backward endcap (BWD). The barrel is 3 m long and has an inner radius of 1.25 m. The annular endcaps close the barrel at $z = 1.96\,\text{m}$ (FWD) and $z = -1.02\,\text{m}$ (BWD) from the interaction point at $z = 0$, where positive z-values go into the direction of the electron beam. Between the three parts there are two small gaps of $\sim 1°$ which are used as a guide for the cables and CO_2 cooling pipes of the inner detectors.

The calorimeter crystals are made of Thallium-doped Cesium Iodide (CsI(Tl)) because of its high light output, relatively short radiation length, good mechanical properties and its moderate price. The calorimeter is built of 8736 crystals, of which 6624 make up the barrel and 2112 the endcaps. In the barrel, each crystal is a truncated pyramid with an average cross section of about $6\,\text{cm} \times 6\,\text{cm}$ and a length of about 30 cm, which corresponds to 16.2 radiation lengths of CsI(Tl). The shapes of the endcap crystals are more complex and are described in detail in [22]. In total there are 29 different crystal cross section shapes in the barrel and 69 in the endcaps. All the crystals are oriented to a region in the vicinity of the interaction point in a non-projective geometry to leave minimal projective gaps between the crystals. This is done to prevent particles coming from the interaction point from propagating through the gaps between the crystals without being detected.

Each crystal is wrapped with a layer of 200 μm thick Gore-Tex porous teflon and covered by a laminated sheet of 25 μm thick aluminium and 25 μm thick mylar. Two $10\,\text{mm} \times 20\,\text{mm}$ Hamamatsu Photonics photodiodes are glued at the rear surface of each crystal for the readout of the scintillation light. The signal of each photodiode is amplified by a preamplifier providing two independent output signals for each crystal which are summed and sent to an external shaper board. This signal then goes to the ECL trigger module as well as to a waveform-digitizer where it is processed to be treated by basf2.

Figure 3.1 shows a schematic view of the ECL surrounding the inner subdetectors. Further details on the structure of the ECL and its electronics can be found in [17, 22–26].

3.2 Data processing for the ECL

A particle enters an ECL crystal and generates scintillation light. This light is the signal to start a row of computing processes. These processes end with the final data objects that are used in an analysis. For the purpose of the coming chapters, the steps from the initial crystal signal to the final data object will be explained. Section 3.2.1 describes the steps from producing scintillation light to the input signal for basf2 and Section 3.2.2 explains how basf2 treats the given input and forms it into the final data object.

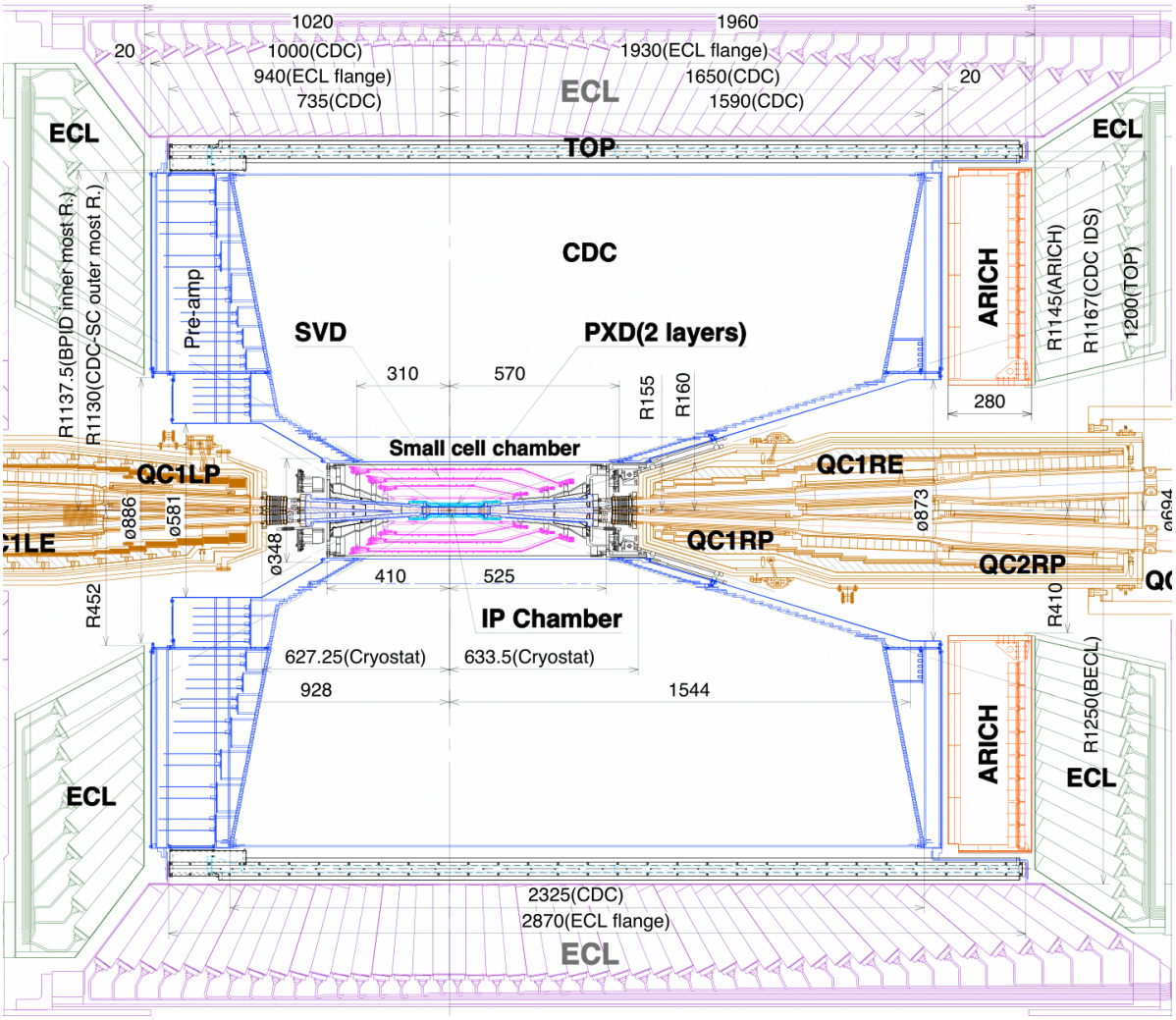

FIGURE 3.1. Schematic view of the ECL and the inner subdetectors. The ECL barrel is shown in light purple, the ECL endcaps in light green. The orientation of the ECL crystals towards the vicinity of the interaction point gets clear. Figure adapted from [27].

3.2.1 From an ECL crystal to the basf2 framework

The scintillation light of each of the 8736 ECL crystals is read out by two Hamamatsu Photonics S2744-08 photodiodes. Each of the two signals is amplified by a preamplifier before the two signals are summed and sent to an external shaper board.

The shaper board consists of a shaping amplifier (Shaper) and a 18-bit flash ADC (Digitizer). The output of the Shaper is used as the input for the Digitizer as well as an input for the ECL trigger. The digitized signal coming from the Digitizer is composed of 31 data points: 15 of them are used to define a baseline for the signal peak, and the remaining 16 make up the signal peak. The

signal is read out by a FPGA, which performs a photon template fit on the 16 signal peak points. The fit results from the FPGA, a signal amplitude and a signal time, are sent to the Collector module, which collects the data of several shaper boards. The Collector module also contains a test pulse generator for the calibration of the response of each ECL crystal. From the Collector module, the data is sent to the COPPER module which then provides the raw data of each crystal for basf2.

The raw data of a single crystal is called an *ECLDigit* and has the form of a 32-bit word. It contains the amplitude of the signal (18-bit), its timing information (12-bit) and a status information (2-bit) of the photon template fit performed by the FPGA. Figure 3.2 shows a schematic view of the signal flow from an ECL crystal to the storage of an ECLDigit. [21, 26, 27]

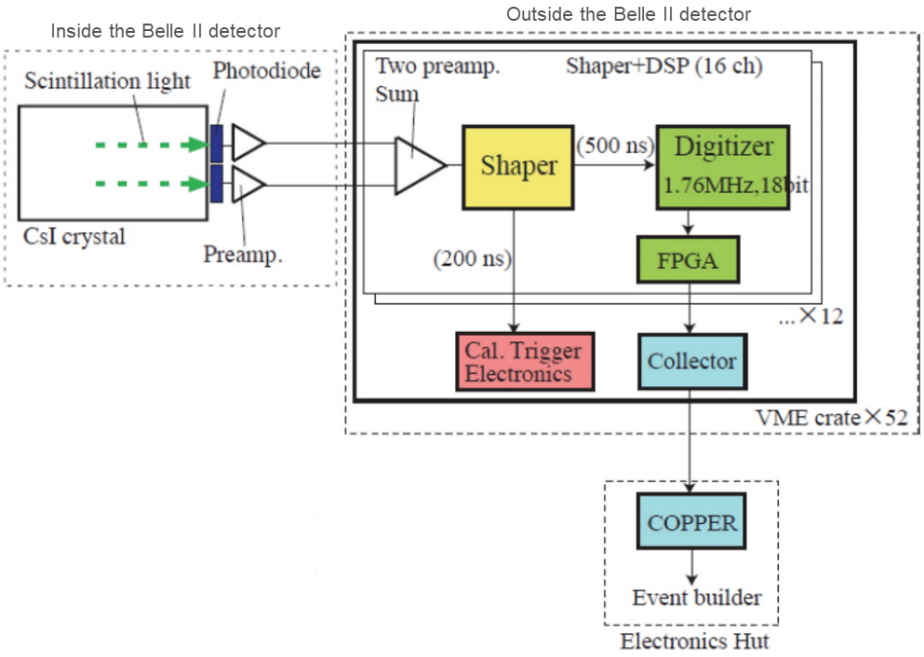

FIGURE 3.2. Schematic view of the signal flow from the production of scintillation light in an ECL crystal to the storage of an ECLDigit for each crystal in the basf2 framework. Figure adapted from [27].

3.2.2 Inside the basf2 framework

A full ECL readout is one ECLDigit for each ECL crystal. The ECLDigits are firstly converted into so-called *ECLCalDigits*: The 18-bit amplitude information is converted into an energy, in GeV, and the timing information into an absolute time, in ns. This is the so-called *crystal energy calibration*. Figure 3.3 shows a schematic and simplified grid of ECLCalDigits, where empty cells are below the readout threshold of $\sim 0.2\,\text{MeV}$.

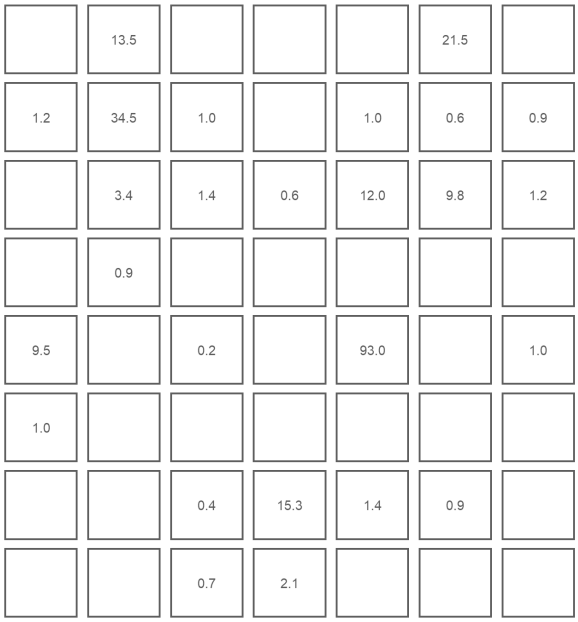

FIGURE 3.3. Schematic and simplified grid of ECLCalDigits. Empty cells are below the readout threshold of ~ 0.2 MeV. Figure adapted from [27].

In the next step, ECLCalDigits are grouped into *ECLConnectedRegions*, which is explained in the following. All ECLCalDigits with energies > 10 MeV are found, which can be seen in Figure 3.4. For each of these ECLCalDigits, the algorithm iteratively adds all direct neighbours with an energy > 0.5 MeV to the ECLCalDigit. In further iterations also next neighbours with energies > 1.5 MeV are added to gradually form an ECLConnectedRegion. The algorithm stops if there are no neighbours with more than 1.5 MeV left. A visualization of the algorithm's result is shown in Figure 3.5. During this process, it is possible that two or more ECLConnectedRegions are merged to one larger ECLConnectedRegion, which can be seen in Figure 3.6.

Now for each ECLConnectedRegion, *Local Maxima* are labeled. These are ECLCalDigits within the ECLConnectedRegion with an energy > 10 MeV and the highest energy among their direct neighbours. This step is shown in Figure 3.7.

Next, the ECLConnectedRegions are split into *ECLShowers*. The number of ECLShowers resulting from an ECLConnectedRegion is equal to the number of Local Maxima contained in this ECLConnectedRegion, and since in almost every physical case the information of an ECLShower is contained in a 5x5 grid of ECLCalDigits around the Local Maximum excluding its corner crystals, this is the maximum size of an ECLShower. This means that for ECLConnectedRegions containing only one Local Maximum, this step is almost redundant: only its size is reduced to the 5x5 crystal grid excluding its corners. In the case of an ECLConnectedRegion containing more than one Local Maximum, the energies of the single ECLCalDigits are distributed to the resulting ECLShowers. To do so, the ECLConnectedRegion is split by iteratively finding a stable

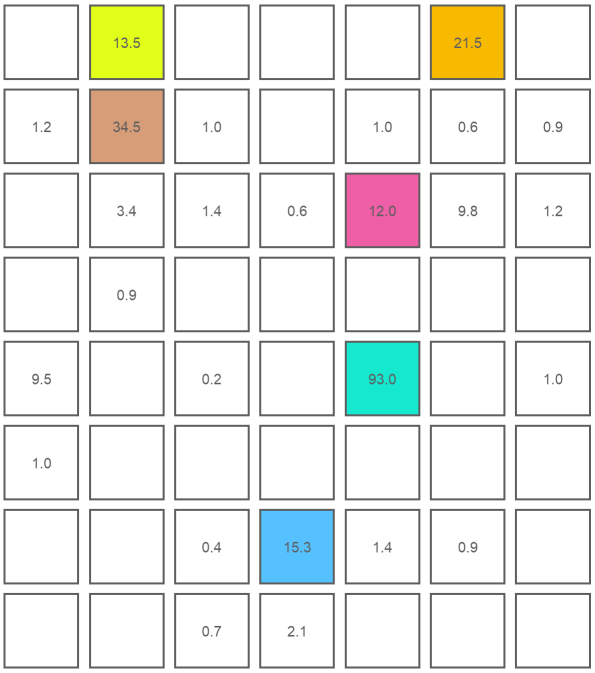

FIGURE 3.4. All ECLCalDigits with energies > 10 MeV are found. Figure adapted from [27].

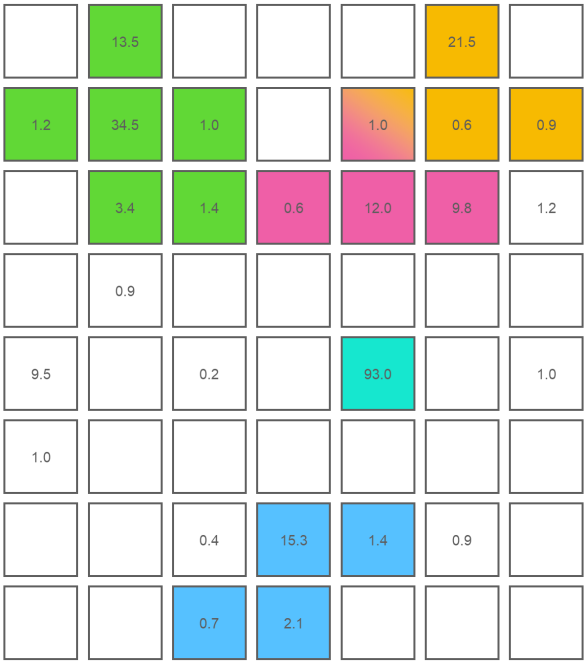

FIGURE 3.5. Visualization of the algorithm producing ECLConnectedRegions. In a first step, all direct neighbours with energies > 0.5 MeV are attached and in further steps all next neighbours with energies > 1.5 MeV. Figure adapted from [27].

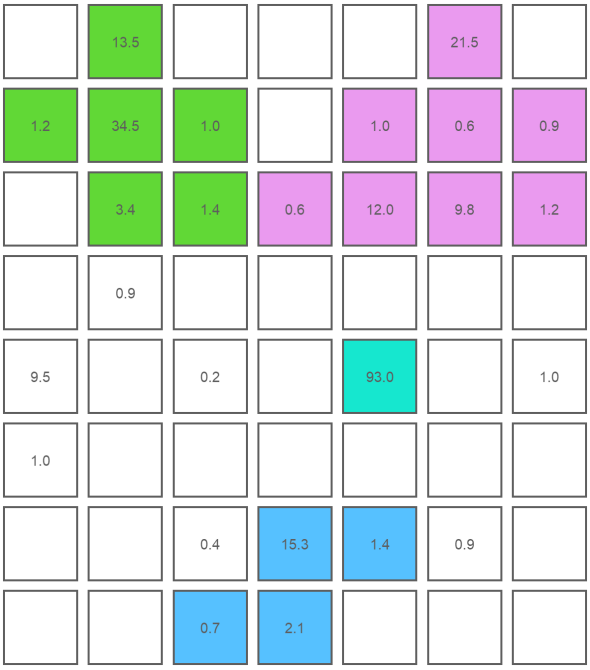

FIGURE 3.6. Merging of two or more ECLConnectedRegions. Compare to Figure 3.5. Figure adapted from [27].

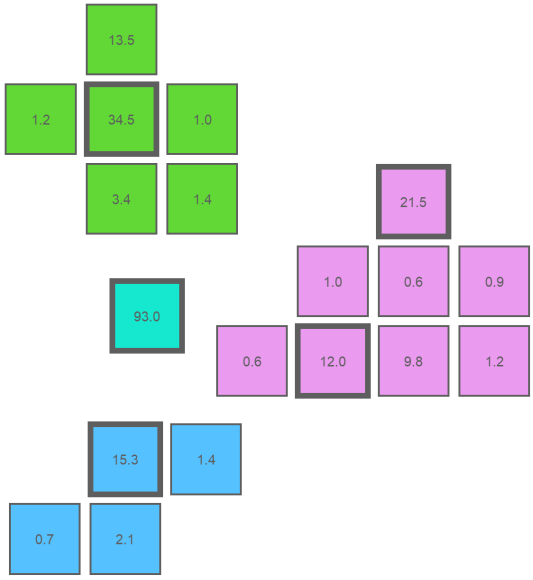

FIGURE 3.7. For each ECLConnectedRegion so called Local Maxima are labeled. These are ECLCalDigits with energies > 10 MeV and the highest energy among their direct neighbours. Figure adapted from [27].

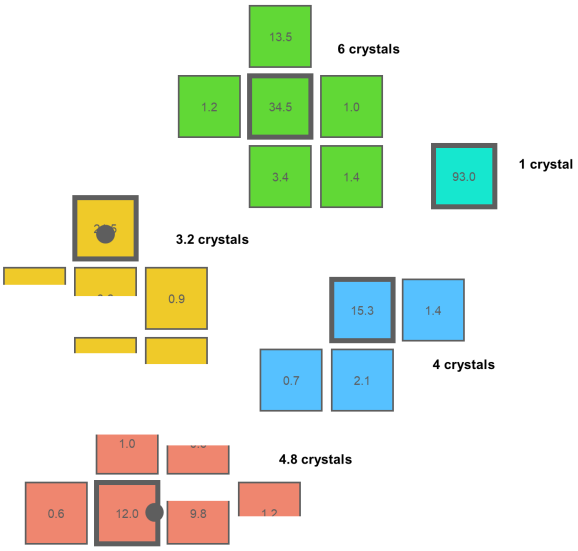

FIGURE 3.8. The ECLConnectedRegions have been split into ECLShowers. The amount of ECLShowers per ECLConnectedRegion equals the amount of Local Maxima within the ECLConnectedRegion. Note that the ECLShowers not necessarily contain an integer amount of crystals anymore. Figure adapted from [27].

center of gravity. In this process, each ECLCalDigit within the ECLConnectedRegion is given a number of weights that add up to 1 and correspond to a respective Local Maximum. The result is one ECLShower per Local Maximum which contains several weighted ECLCalDigits. This can be seen in Figure 3.8.

Weighting the ECLCalDigits raises the question: how do the energy and timing information get propagated from the individual crystals to the shower data object? The energy of an ECLShower is the sum of the n most energetic crystals within the ECLShower up to a certain n, where n depends on an initial rough energy estimation and a background estimation, and can be between 1 and 21. The timing information of the ECLShower is just the timing information of the Local Maximum of the ECLShower. An additional problem is the definition of the position of the ECLShower. For the position of an ECLShower, a (θ, ϕ, R) coordinate is reconstructed, where R is given by the position of the Local Maximum of the ECLShower.

The last conversion step is from an ECLShower to an *ECLCluster*. While an ECLShower is the ECL-internal dataobject that contains additional debug information, an ECLCluster is the final dataobject which is stored and available on user level for analysis. Only ECLShowers with a total energy > 20 MeV are converted into ECLClusters. At this point, one more cut is applied: For ECLShowers with a total energy of < 50 MeV, the variable t/dt99 (see 3.3 for details) is cut to be between -1 and 1 for saving disc space. [21, 27, 28]

3.3 Photon variables

After saving specific information for each ECL crystal and converting this information to ECLClusters, basf2 is able to calculate many variables describing the ECLCluster. These variables are referred to as *photon variables* since ECLClusters not matched to a CDC track are assumed to be photons and are candidates for the reconstruction of π^0s (photon hypothesis).

All of these ECLCluster variables have a limited precision p to save disc space. The precision is always better than the precision of the ECL data acquisition. However, if the ECLCluster variables are histogrammed, binning effects are likely to occur. This can be seen in Figures 3.11 to 3.18.
To prevent these binning effects, the *intrinsic binning* $n_{intrinsic}$ or a multiple of it can be used. It is calculated via

$$n_{intrinsic} = \frac{\max - \min}{2^p + 1} \quad , \tag{3.1}$$

where p is the integer precision of the photon variable and max and min are the maximum and minimum of the desired range of the histogram, respectively. The precision p for the different variables can be found in [29].
Additionally, the ECLCluster variables are clipped at the lower and upper boundaries. Values below the lower boundary will be set to the lower bound, values above the upper bound will be set to the higher bound.

Among the ECLCluster variables there is a category of variables named *shower shape variables*. These variables quantify the shape of an ECLCluster, e.g. to distinguish electromagnetic showers from hadronic ones.

The most important photon variables with respect to this thesis are explained in the following. [27, 28, 30]

3.3.1 clusterE and clusterReg

The energy of the whole ECLCluster is called *clusterE*. Note that only ECLClusters with energies larger than 20 MeV are stored. Photon energy distributions always show a low energy tail due to longitudinal and transverse leakage in the ECL crystals. This tail can be further modified by beam backgrounds and the clustering algorithm described in Section 3.2. Therefore, the peak position of the photon energy distributions is corrected to match the true photon energy in Monte Carlo.

For this thesis, the clusterE variable is combined with the *clusterReg* variable. The clusterReg variable gives the detector region for an ECLCluster. This means that different clusterE cuts are applied for the different detector regions. It returns 1 if the ECLCluster is in the forward endcap, 2 if it is in the barrel, and 3 if it is in the backward endcap. It also can return 11 if the ECLCluster is in the gap between the forward endcap and the barrel or 13 if it is in the gap

between the backward endcap and the barrel. The clusterE cut for a gap is always the same as for the corresponding endcap. This results in three different clusterE cuts: one for the barrel, one for the forward endcap and the corresponding gap and one for the backward endcap and the corresponding gap.

Figure 3.9[1] shows the clusterE distribution for a $\Upsilon(4S) \to B^0\overline{B^0}$ Monte Carlo sample. No truth-matching[2] is applied. Figure 3.10 shows the same distribution but zoomed. The $|t/dt99| < 1$ cut for energies < 50 MeV is clearly visible. Also the fact that only ECLShowers with energies > 20 MeV get converted to ECLClusters can be seen.

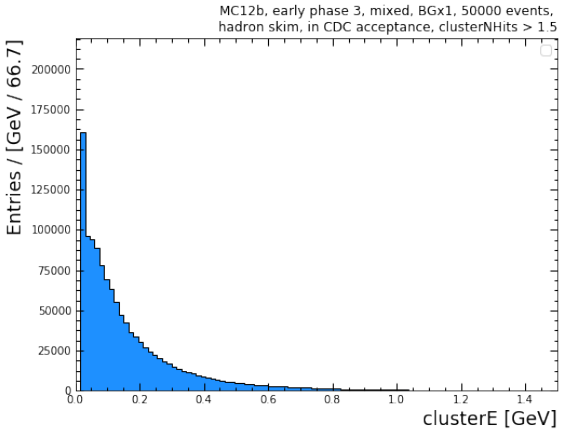

FIGURE 3.9. clusterE distribution for a MC12b, early phase3, mixed sample with 50,000 events. The following cuts are applied: hadron skim, in CDC acceptance which is 0.2967 rad < clusterTheta < 2.6180 rad and clusterNHits > 1.5. Note that no truth-matching is applied for the ECLClusters.

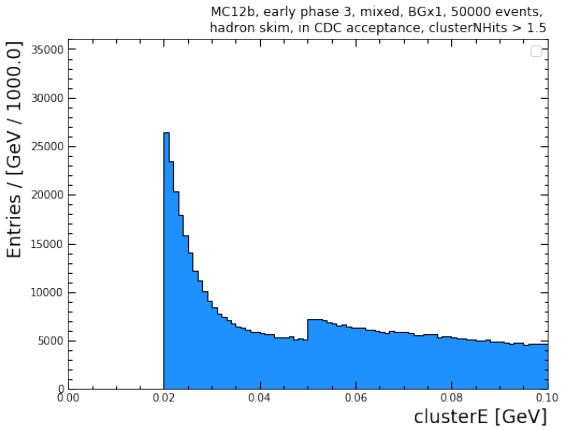

FIGURE 3.10. Zoomed version of Figure 3.9. The 20 MeV cut in the conversion from ECLShowers to ECLClusters and the timing cut for ECLClusters with clusterE < 50 MeV are clearly visible.

3.3.2 t/dt99

The variable $t/dt99$ is calculated by dividing the variable t (clusterTiming) by the variable dt99 (clusterErrorTiming). The photon timing t is given by the fitted time of the recorded waveform of the highest energetic crystal in the ECLCluster, and contains several corrections, like the time-of-flight correction. dt99 is a measure for the photon timing uncertainty. It is designed so that $|t/dt99| < 1.0$ gives a 99% photon efficiency for true photons in Monte Carlo. Note that the

[1] The meanings of the sample details given in the Figure description are described in Chapter 5.
[2] Truth-matching is explained in Chapter 4

t/dt99 variable is very energy- and background-dependent, and that the selection $|t/dt99| < 1.0$ is already applied for photons with energies below 50 MeV on software level. This can be clearly seen in the t/dt99 distribution in Figure 3.11.

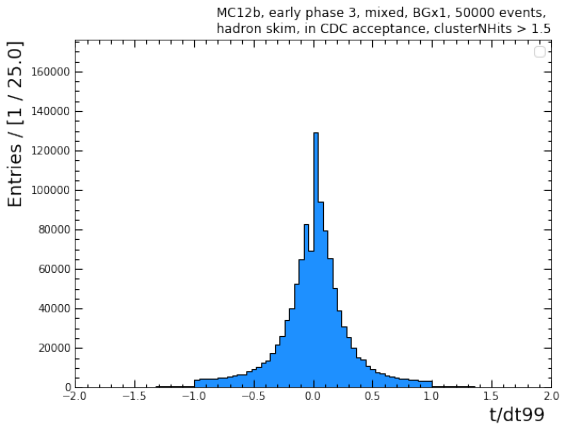

FIGURE 3.11. t/dt99 distribution for the same sample used for Figure 3.9 with the same cuts applied. The $|t/dt99| < 1$ cut for ECLClusters with clusterE < 50 MeV is apparent.

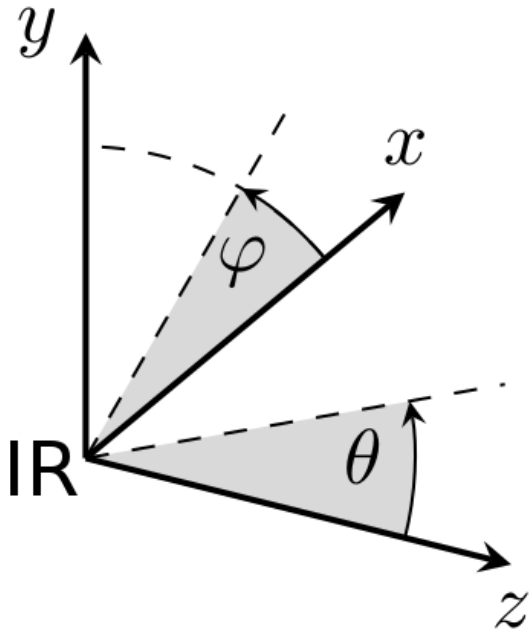

FIGURE 3.12. Visualization of the Belle II coordinate system. The definition of the cartesian and spherical coordinates is shown. Coordinates refer to the origin in the interaction region (IR). Figure adapted from [31].

3.3.3 clusterTheta and clusterPhi

clusterTheta gives the polar angle θ of the ECLCluster, *clusterPhi* gives its azimuthal angle ϕ. Both are taken from the geometric position of the centroid of the ECLCluster, which is the logarithmically weighted average of all crystal positions in the ECLCluster evaluated at the crystal centres. clusterPhi ranges from $-\pi$ to π, clusterTheta from 0 to π.

An insight on the coordinate system of Belle II is necessary here. The origin of the coordinate system is defined by the interaction point within the interaction region. The cartesian coordinates are defined as follows: the z-axis goes into the direction of the electron beam. This is also the direction of the magnetic field in the Belle II detector. The y-axis goes vertically in the direction of the hall ceiling and the x-axis is defined perpendicular to the two other axes to obtain a right-handed coordinate system. The Belle II coordinate system is visualized in Figure 3.12. It

also shows the definition of the spherical coordinates Θ (clusterTheta) and ϕ (clusterPhi).

The different detector regions are defined by their clusterTheta ranges. One important example is the CDC acceptance, which ranges from clusterTheta = 0.297 rad to clusterTheta = 2.618 rad. This range is very important for the ECL, since only in this range tracking information from the CDC is available. Tracks are used to distinguish ECLClusters left by charged particles from neutral particles.
Also the three ECL regions are defined via their clusterTheta range. The ECL forward-endcap ranges from 0.297 rad to 0.546 rad, the ECL barrel from 0.562 rad to 2.246 rad, and the ECL backward-endcap from 2.281 rad to 2.618 rad.

3.3.4 clusterNHits

This variable gives the amount of ECL crystals contributing to the ECLCluster. This variable is not necessarily an integer. After an ECLConnectedRegion gets split, the resulting ECLShowers are not necessarily made of an integer amount of ECLCalDigits anymore. *clusterNHits* gives the sum of the weights of the ECLCalDigits within the ECLShower. See Section 3.2 for details.

3.3.5 clusterE1E9

clusterE1E9 belongs to the category of shower shape variables and gives the ratio of the energy contained in the central crystal of the ECLCluster to the energy contained in the 3x3 crystal grid around the central crystal. Therefore this number lies between 0 and 1. Since photons tend to deposit their energy in small circular clusters, clusterE1E9 tends towards unity for photons (~ 0.8). For broader hadronic clusters, it tends towards smaller values. Figure 3.13 shows the clusterE1E9 distribution for the $\Upsilon(4S) \to B^0\overline{B^0}$ Monte Carlo sample.

3.3.6 clusterE9E21

clusterE9E21 belongs to the category of shower shape variables and gives the ratio of the energy contained in the 3x3 crystal grid around the central crystal of the ECLCluster to the energy contained in the 5x5 crystal grid around the central crystal, excluding the 4 corners. The corners are not taken into account since they typically do not contain any relevant information. This variable also lies between 0 and 1 and tends to unity for photons as well as to smaller values for hadronic clusters, although less sharply than clusterE1E9. The clusterE9E21 distribution for the $\Upsilon(4S) \to B^0\overline{B^0}$ Monte Carlo sample can be seen in Figure 3.14.

3.3.7 clusterLAT

clusterLAT quantifies the lateral energy distribution of the ECLCluster. It is defined via

$$S = \frac{\sum_i^3 w_i E_i r_i^2}{\sum_i^3 w_i E_i r_i^2 + w_0 E_0 r_0^2 + w_1 E_1 r_0^2} \quad , \tag{3.2}$$

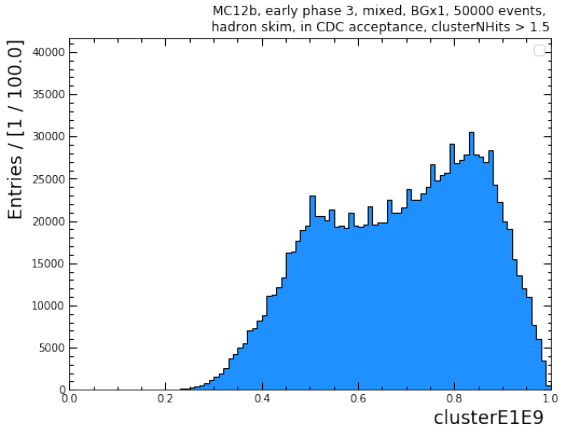

FIGURE 3.13. clusterE1E9 distribution for the same sample used for Figure 3.9 with the same cuts applied. Note the binning effects mentioned earlier.

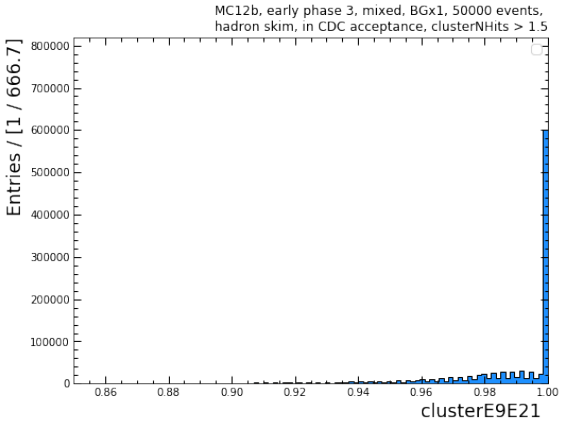

FIGURE 3.14. clusterE9E21 distribution for the same sample used for Figure 3.9 with the same cuts applied. Note the binning effects mentioned earlier.

where E_i are the energies of the crystals in the ECLCluster sorted by energy (E_0 is the maximum), w_i is the corresponding weight to the i-th crystal after the splitting of the respective ECLConnectedRegion into ECLShowers (see 3.2 for details), r_i is the distance of the i-th crystal to the center of the ECLCluster, and $r_0 \sim 6\,\text{cm}$ is the average distance between two crystal centers. clusterLAT has values between 0 and 1. It peaks around 0.3 for radially symmetric electromagnetic showers and has larger values for hadronic showers or electrons with a nearby radiative or Bremsstrahlung photon. Note that clusterLAT is only calculated for ECLClusters containing more than 3 crystals (clusterNHits > 3). For all other clusters the clusterLAT variable is set to 0, which leads to a sharp peak at 0. clusterLAT is a member of the group of shower shape variables. Figure 3.15 shows the clusterLAT distribution for the $\Upsilon(4S) \to B^0\overline{B^0}$ Monte Carlo sample.

3.3.8 clusterAbsZernikeMoment40, clusterAbsZernikeMoment51 and clusterZernikeMVA

For each ECLCluster several Zernike moments are calculated, of which two are directly available in basf2. Qualitatively speaking, Zernike moments are a measure of "how circular" a distribution in a plane is. Applied to ECLClusters, the Zernike moments can distinguish between particles interacting electromagnetically and hadronically and are therefore shower shape variables. For all ECLClusters, *clusterAbsZernikeMoment40* and *clusterAbsZernikeMoment51* are calculated via

$$|Z_{nm}| = \frac{n+1}{\pi} \frac{1}{\sum_i w_i E_i} \left| \sum_i R_{nm}(\rho_i) e^{-im\alpha_i} w_i E_i \right| \quad , \tag{3.3}$$

where n and m are integer numbers defining the Zernike moment, E_i is the energy of the i-th crystal belonging to the ECLCluster, w_i is the weight of the i-th crystal after the splitting of the respective ECLConnectedRegion into ECLShowers (see 3.2 for details), R_{nm} is the related Zernike polynomial, ρ_i is the radial distance of the i-th crystal in the perpendicular plane, and α_i is the polar angle of the i-th crystal in the perpendicular plane.
$|Z_{40}|$ can have values between 0 and 1.6 and $|Z_{51}|$ between 0 and 1.2. The values are lower for hadronic showers and tend to higher values for electromagnetic showers. Figure 3.16 and Figure 3.17 show the clusterAbsZernikeMoment40 and clusterAbsZernikeMoment51 distributions for the $\Upsilon(4S) \rightarrow B^0\overline{B^0}$ Monte Carlo sample.

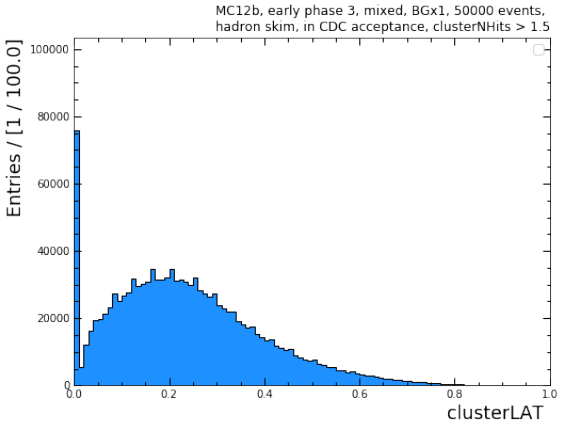

FIGURE 3.15. clusterLAT distribution for the same sample used for Figure 3.9 with the same cuts applied. Note the binning effects mentioned earlier and the peak at 0.

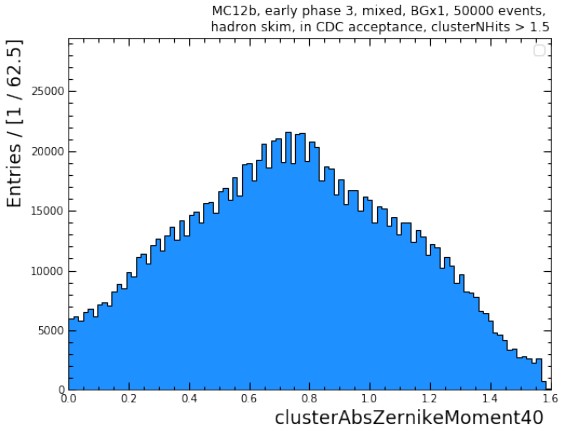

FIGURE 3.16. clusterAbsZernikeMoment40 distribution for the same sample used for Figure 3.9 with the same cuts applied. Note the binning effects mentioned earlier.

In addition, for each ECLCluster, the output of a multivariate analysis (MVA) classifier is evaluated. This is the *clusterZernikeMVA* variable. The classifier is trained to distinguish between photon and K_L^0 showers. 11 different Zernike moments serve as the inputs for this MVA. clusterZernikeMVA can have values between 0 and 1, where photon clusters tend to 1 and K_L showers tend to 0. clusterZernikeMVA belongs to the category of shower shape variables. The distribution of clusterZernikeMVA for the $\Upsilon(4S) \rightarrow B^0\overline{B^0}$ Monte Carlo sample can be seen in Figure 3.18.
More details on how the three Zernike variables are calculated can be found in [30].

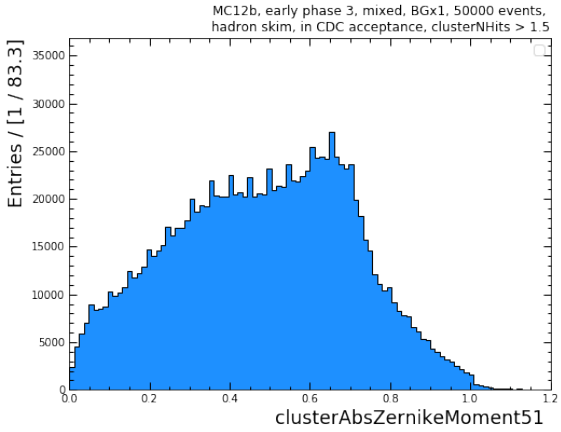

FIGURE 3.17. clusterAbsZernikeMoment51 distribution for the same sample used for Figure 3.9 with the same cuts applied. Note the earlier mentioned binning effects.

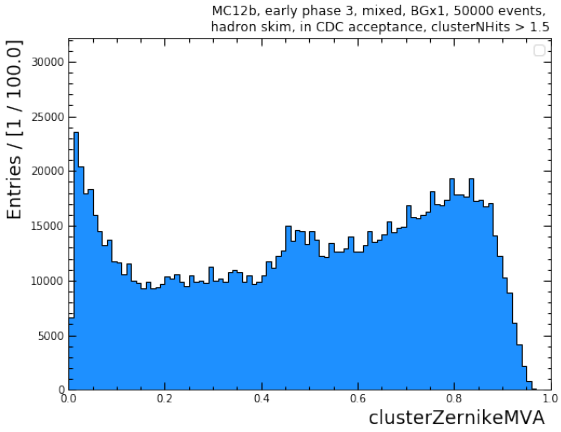

FIGURE 3.18. clusterZernikeMVA distribution for the same sample used for Figure 3.9 with the same cuts applied. Note the earlier mentioned binning effects.

3.4 Generic photon lists in basf2

For the use in different analyses, basf2 provides several default photon selections that contain cuts on different photon variables. Some of these selections are explicitly made for yielding a certain π^0 reconstruction efficiency when reconstructing π^0s out of photons from these selections.

All of these default selections contain the CDC acceptance cut 0.2967 rad < clusterTheta < 2.6180 rad. Additionally, a region-dependent clusterE cut is applied, as well as t/dt99 and clusterE1E9 cuts for photons with energies > 100 MeV. The definitions of the selections are shown in Table 3.1. By construction, the cut on a given variable gets tighter for lower efficient selections.

Photon selection	**clusterE cut in BRL**	**clusterE cut in FWD**	**clusterE cut in BWD**	**|t/dt99| cut**	**clusterE1E9 cut**
gamma:pi0eff60	> 20 MeV	> 30 MeV	> 30 MeV	< 1.0	> 0.3
gamma:pi0eff50	> 30 MeV	> 50 MeV	> 50 MeV	< 1.0	> 0.3
gamma:pi0eff40	> 30 MeV	> 75 MeV	> 75 MeV	< 0.5	> 0.5
gamma:pi0eff30	> 50 MeV	> 75 MeV	> 75 MeV	< 0.5	> 0.7
gamma:pi0eff20	> 75 MeV	> 75 MeV	> 75 MeV	< 0.1	> 0.7

TABLE 3.1. Overview on the differences of the current implemented generic photon seletions in basf2 that are used to yield a certain π^0 reconstruction efficiency. All the variables additionally contain the CDC acceptance cut on clusterTheta. The t/dt99 and clusterE1E9 cuts are only applied for photons with clusterE > 100 MeV.

CHAPTER 4

FROM NEUTRAL PIONS TO THE PION VARIABLES IN BASF2

The goal of this thesis is to provide optimized standard particle selections for the π^0 reconstruction in basf2. In order to work properly on a particle reconstruction, one has to understand the particle first. This chapter describes properties of the π^0 and how it is handled in basf2. Section 4.1 gives an overview on the physics of π^0s as well as the π^0 reconstruction procedure in basf2 and Section 4.2 describes the π^0 variables used for this thesis.

4.1 Neutral pions

The neutral pion (π^0) has a special status in the world of particle physics. It is the lightest hadron observed in nature. As a meson, it can be made up of an up quark and an anti-up quark or of a down quark and an anti-down quark. In fact, it is defined as the lowest-energy superposition of these two states.

The π^0 was the first particle to be discovered with an accelerator, in 1950. Over the years, the properties of the π^0 have been measured with increasing precision. It has a mass of $134.9766 \pm 0.0006\,\mathrm{MeV/c^2}$ and a mean lifetime of $(8.52 \pm 0.18) \times 10^{-17} s$.

The π^0 predominantly decays in two ways. The most important decay channel is the *two-photon decay*, $\pi^0 \to \gamma\gamma$. Having a branching ratio of $98.823 \pm 0.034\,\%$, this means that to first approximation every π^0 decays in this manner. The second most common decay channel is the so-called *Dalitz decay*. In this channel the π^0 decays via $\pi^0 \to e^+e^-\gamma$, but with a branching ratio of $1.174 \pm 0.035\,\%$ it already is negligible compared to the two-photon decay. There are several other decay channels listed by the particle data group (PDG) [32] with branching ratios in the orders of 10^{-4} to 10^{-9}. But since these decay channels are not taken into account for the π^0 reconstruction in basf2 and therefore this thesis, they are not further considered. [32, 33]

4.1.1 Neutral pions in B-decays

Neutral pions play a major role in the decays of B-mesons and therefore in the event reconstruction of Belle II. B-mesons have many hadronic decay channels into lighter mesons, like D-mesons or kaons, with several of these channels decaying into π^0s in the final state. The D-mesons, in turn, often yield kaons as well as π^0s. The kaons often decay into π^0s, which can eventually lead to many π^0s produced by one B-meson. In fact, one third of B-meson decay products are π^0s or other neutral particles decaying into photons. This makes the π^0 reconstruction, as well as the overall ECL reconstruction, crucial for *Belle II*.

Another reason for the importance of the π^0 reconstruction in *Belle II* is driven by the experiment setup itself. As mentioned in Chapter 2, the *SuperKEKB* collision energy at the mass of the $\Upsilon(4S)$-resonance is just enough to create two B-mesons, which implies a clean and low-background environment. Therefore, all particles created in an event can be assigned to one of the two produced B-mesons. In order to make the most out of this setup, it is vital to reconstruct every particle involved. [32]

4.1.2 Neutral pions in basf2

After having seen how the π^0 decays, the question arises how this is reconstructed in basf2. This Section describes how two photon-hypothesis ECLClusters are combined to reconstruct the properties of the π^0.

The first thing to mention is the decay channel used for the reconstruction. In principal, every decay channel can be used. This choice is up to the user and depends on the respective analysis. For this thesis, only the two-photon decay of the π^0, $\pi^0 \to \gamma\gamma$, is used. Since it has a branching ratio of 98.823%, all other decay channels are neglected.

An important issue is the combinatorics of the reconstruction. For the reconstruction of π^0s, only ECLClusters that don't have any tracking information from the CDC, and therefore are not produced by charged particles, are used, i.e. only ECLClusters produced from neutrals. Before combining two of these ECLClusters into a π^0, no additional cuts are applied. Also, there are no constraints on which ECLClusters get combined, meaning that each ECLCluster gets combined with every other one. This leads to an enormous amount of reconstructed π^0 candidates, which makes it quickly problematic to handle them.

The clusters are combined as follows. For each of the two ECLClusters, a θ and a ϕ angle is calculated, which are called *theta* and *phi* in basf2. Note that these angles are not the same as the clusterTheta and clusterPhi angles described in Section 3.3. theta and phi are calculated by connecting the photon vertex with the centroid position of the ECLCluster as described in Section 3.3. The photon vertex is an external information and taken as the average beam spot

position. Note that this position is usually not the origin of the *Belle II* coordinate system[1]. With the two angles it is possible to calculate the direction vector of the ECLCluster associated with the photon candidate. Together with the energy of the ECLCluster and the fact that a photon is massless, this allows to compute the four-momentum of the photon candidate. The four-momenta of the two photon candidates are now added to obtain the four-momentum of the reconstructed π^0 candidate. This, in turn, constrains the properties like mass, momentum, and direction of the π^0 candidate.

This procedure is the same for ECLClusters from data as from Monte Carlo. But for Monte Carlo so-called *truth-level* information is also available. For Monte Carlo it is possible to tell whether a photon is a *true* or a *background* photon candidate. In the same manner it is possible to tell whether a π^0 candidate is a true or a background π^0. Using this distinction, one can use the Monte Carlo to study the true π^0s in order to optimize the signal selection and reduce the background contribution. The selection can then be checked on data.

The procedure that distinguishes between signal and background is called *truth-matching*. Each Monte Carlo photon candidate deposits energy in several ECL crystals. These crystals are usually located next to each other, but this may not be the case. It is possible that the photon deposits energy in crystals that are not adjacent due to simulated physics reactions on the way of the photon from the photon vertex to the ECL. It can also happen that the photon hypothesis is not correct and the ECLCluster is something different, e.g. an electron-positron pair or a hadron, which can lead to more complicated patterns of energy deposition.
After the ECLDigits of the ECL crystals have been combined and converted into ECLClusters, it is possible that one photon candidate has deposited energy in more than one ECLCluster. The truth-matching algorithm now calls a photon candidate a true (or truth-matched) photon if there is an ECLCluster in which the candidate has deposited more than 60 % of its energy. The candidate is then matched to this ECLCluster. All other photon candidates are considered background photons.
The truth-matching procedure for a π^0 candidate is conceptually simpler. If the π^0 candidate is made of two truth-matched photons it is called a true or truth-matched π^0, otherwise it is considered a background π^0. In this thesis, background photons and background π^0s are also referred to as not-truth-matched photons and not-truth-matched π^0s.

[1] At the time of writing this thesis, the average beam spot position is in the origin of the Belle II coordinate system, which will change during the course of phase 3.

4.2 Pion variables

After combining two ECLClusters interpreted as photons, basf2 provides a large number of variables describing the reconstructed π^0 candidate. These variables are referred to as π^0 *variables* for the scope of this thesis. The definition of π^0 variables covers variables describing the π^0 candidate itself, but also the two photon daughters.

The following Section gives an overview on the most important π^0 variables used for this thesis.

4.2.1 InvM

InvM is the reconstructed mass of the π^0. It is also called $M(\gamma\gamma)$, since it is calculated as the invariant mass of the pair of photons. Figure 4.1 shows the InvM distribution for the π^0s reconstructed from the $\Upsilon(4S) \to B^0\overline{B^0}$ Monte Carlo sample. Note that no truth-matching is applied. Therefore the distribution contains signal and background π^0s.
The background π^0s peak at around 60 MeV/c^2 and decrease smoothly for higher and lower InvM values. The signal π^0s peak at around ~ 132.5 MeV/c^2. A zoom around is shown in Figure 4.2. Note that the π^0 peak is not at the PDG value, which is 134.9766 ± 0.0006 MeV/c^2. This is because of the fact that photon energy distributions always show a low energy tail due to leakage and backgrounds (see Section 3.3). When combining two photons to a π^0, the π^0 peak is shifted to slightly smaller values. The π^0 peak must not be corrected to the PDG value by adjusting the reconstructed photon energies. This would lead to a miscalibration of the photons.

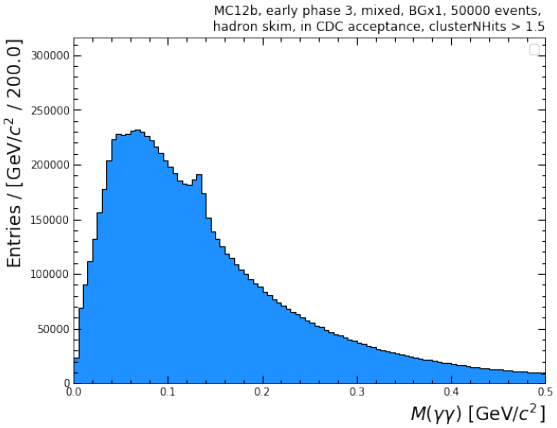

FIGURE 4.1. InvM distribution for the same sample used for Figure 3.9. No additional cuts on π^0 variables are applied. Note the large amount of background. Nonetheless, the π^0 peak at ~ 132 MeV/c^2 is already visible.

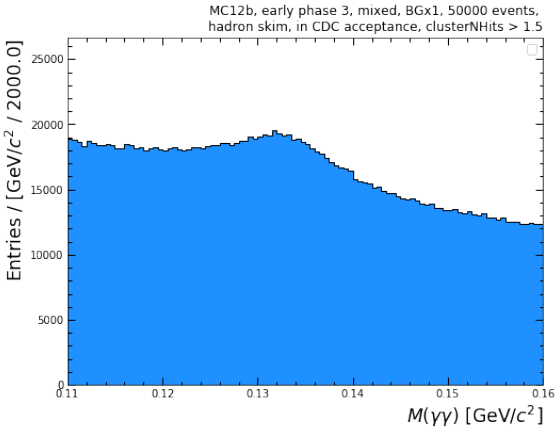

FIGURE 4.2. Zoomed version of Figure 4.1. The shifted π^0 peak at ~ 132.5 MeV/c^2 is clearly visible.

4.2.2 PTD

The *PTD* (photon timing difference) variable gives the difference between the photon timing values of the two photon daughters, t_1 and t_2. The distribution is symmetric around $PTD = 0$ because the labeling of photon 1 and 2 is arbitrary. Figure 4.3 shows the PTD distribution for the $\Upsilon(4S) \to B^0\overline{B^0}$ Monte Carlo sample already used in Section 3.3.

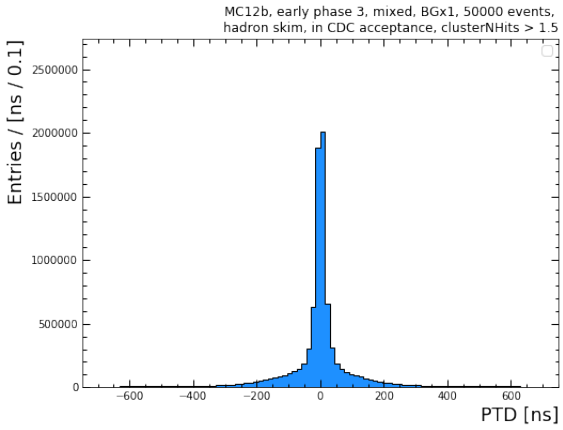

FIGURE 4.3. PTD distribution for the same sample used for Figure 4.1.

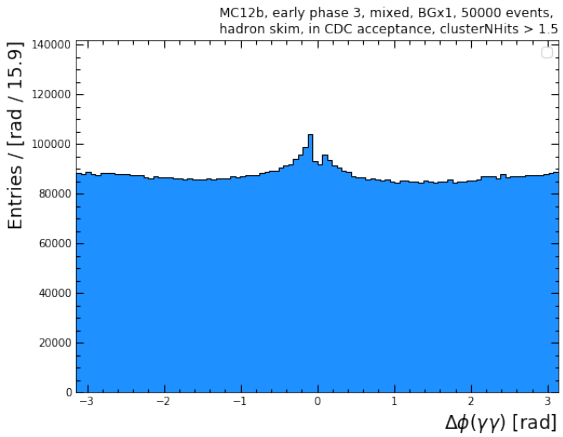

FIGURE 4.4. GammasDeltaPhi distribution for the same sample used for Figure 4.1.

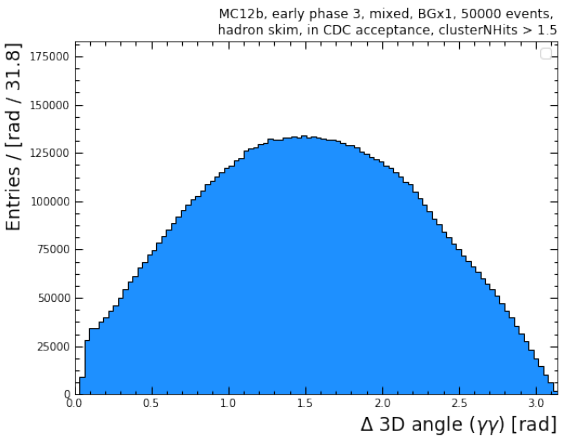

FIGURE 4.5. GammasDelta3D distribution for the same sample used for Figure 4.1.

4.2.3 GammasDeltaPhi

GammasDeltaPhi calculates the difference between the two ϕ angles of the two daughter photons. In basf2 it is called daughterDiffOfPhi(0, 1). In this thesis it is also referred to as $\Delta\phi(\gamma\gamma)$. Figure 4.4 shows the distribution for the $\Upsilon(4S) \to B^0\overline{B^0}$ Monte Carlo sample.

4.2.4 GammasDelta3D

GammasDelta3D gives the angle between the momenta of the two photon daughters. In basf2 it is called daughterAngleInBetween(0, 1). In this thesis it is also referred to as Δ 3D angle ($\gamma\gamma$). Figure 4.5 shows its distribution for the $\Upsilon(4S) \to B^0\overline{B^0}$ Monte Carlo sample.

4.3 Generic π^0 lists in basf2

basf2 provides generic particle lists for the reconstruction of π^0s. A particle list is defined by its selection and is used to reconstruct a given particle. Some of the generic π^0 lists are made to yield a certain π^0 reconstruction efficiency. The default lists contain different cuts on InvM. For the reconstruction of these lists, the corresponding photon lists described in Section 3.4 are used. The different default π^0 lists are listed in Table 4.1.

π^0 list	**InvM window**
pi0eff60	$75\,\mathrm{MeV/c^2} < \mathrm{InvM} < 175\,\mathrm{MeV/c^2}$
pi0eff50	$90\,\mathrm{MeV/c^2} < \mathrm{InvM} < 175\,\mathrm{MeV/c^2}$
pi0eff40	$124\,\mathrm{MeV/c^2} < \mathrm{InvM} < 140\,\mathrm{MeV/c^2}$
pi0eff30	$126\,\mathrm{MeV/c^2} < \mathrm{InvM} < 139\,\mathrm{MeV/c^2}$
pi0eff20	$129\,\mathrm{MeV/c^2} < \mathrm{InvM} < 137\,\mathrm{MeV/c^2}$

TABLE 4.1. Overview on the differences of the current implemented generic π^0 lists in basf2 that are used to yield a certain π^0 reconstruction efficiency. The lists are reconstructed using the corresponding generic photon lists from Section 3.4.

The π^0 reconstruction *efficiency* ϵ is defined as

$$\epsilon = \frac{\text{number of truth-matched } \pi^0 \text{ candidates that pass the selection}}{\text{number of all generated } \pi^0\text{s}} \quad . \tag{4.1}$$

To obtain the nominator, a photon list is filled with the fillParticleList module in basf2. After reconstructing a π^0 list with the reconstructDecay module, the selected π^0s are truth-matched and counted. For the denominator, a π^0 list is directly filled by the fillParticleListFromMC module in basf2 and the π^0s are counted.

The other quantity of importance for this thesis is the π^0 reconstruction *purity* p. It is defined as:

$$p = \frac{\text{number of truth-matched } \pi^0 \text{ candidates that pass the selection}}{\text{number of } \pi^0 \text{ candidates that pass the selection}} \quad . \tag{4.2}$$

The nominator is the same as in the definition of the efficiency and the denominator is the amount of π^0 candidates reconstructed via the fillParticleList and reconstructDecay modules but without truth-matching.

The efficiency is a measure for how many π^0 candidates survive an applied selection, while the purity describes how many of the surviving candidates are really π^0s. Note that both quantities are reasonably defined only for Monte Carlo.

A pair of these two numbers is called a *working point*. For each selection there is an efficiency and a purity value, so each selection defines a working point. The goal is to maximize the purity value for a given efficiency value or vice versa. The purpose of this thesis is to provide such optimized generic π^0 lists for basf2.

Figure 4.6 visualizes the working points for the default π^0 lists currently available in basf2. Note that the lists do not provide the efficiencies implied by their names. Figure 4.6 also shows the working point for no selection applied, which is at ~ 64 % efficiency. The efficiency value is so low due to the ECL acceptance and the efficiency definition. It is not normalized to be at 100 %.

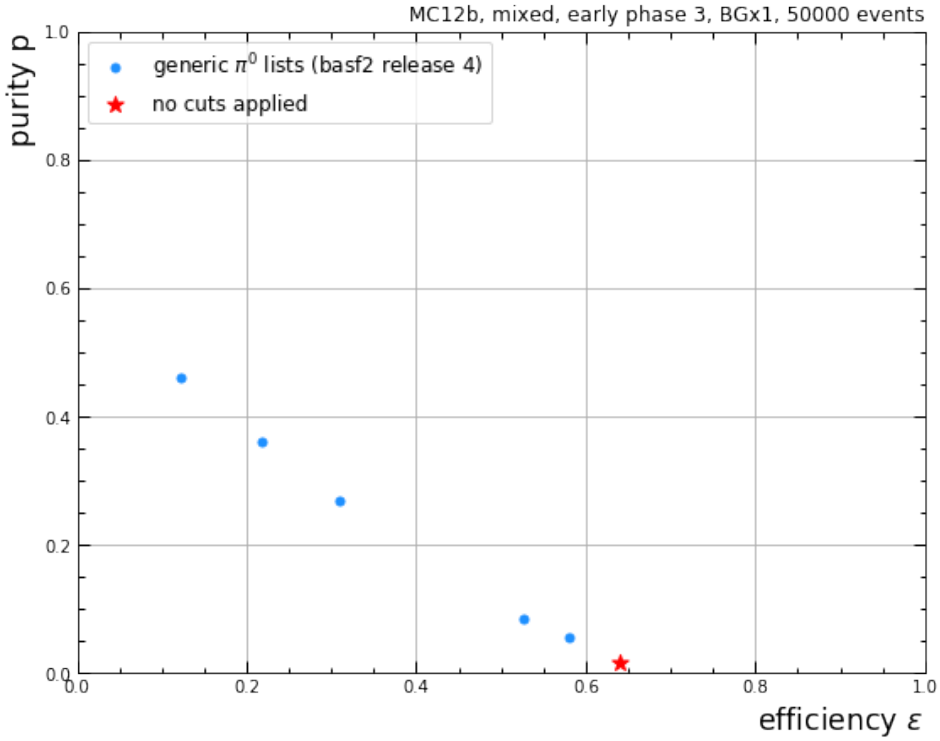

FIGURE 4.6. Visualization of the working points defined by the generic π^0 lists provided in basf2 in blue. The red star shows the working point for no selection applied at all. Since the π^0 reconstruction in Monte Carlo already contains several constraints, this is not at 100 %.

CHAPTER 5

VARIABLE STUDY

In order to provide optimized versions of the current existing π^0 reconstruction selections, it is necessary to investigate the possible cut variables and the applied cut values used for these selections. For yielding the optimized selections, a full grid scan on a choice of cut variables and cut values is performed and described in Chapter 6. The foundation for the grid scan is laid with the variable study in this chapter.

Section 5.1 starts with the description and justification of a preselection applied to the used sample in order to reduce the amount of π^0 candidates. Section **??** investigates the correlations between the different cut variables, while Section **??** takes a look at the different variable distributions and figure of merits to find the best cut values. Section 5.4 closes this chapter with a side study on the efficiency loss per photon energy bin for the different cut variables and cut values.

All the studies in this Chapter are performed on a MC12b (Monte Carlo production 12b), mixed ($\Upsilon(4S) \to B^0\overline{B^0}$), early phase 3 (significantly smaller beam background and only 1.25 layers of PXD), BGx1 (assumed background multiplied by 1), Monte Carlo sample with 50,000 events assuming that the results will also hold for nominal phase 3 (full beam background and full PXD) samples.

5.1 Preselection

When starting this study, an unofficial MC10, mixed, nominal phase 3, BGx1, Monte Carlo sample was used with ~ 2000 π^0 candidates per event. This number is called π^0 *multiplicity*. Without any preselections, it was impossible to perform an appropriate variable study and grid scan due to the huge amount of π^0 candidates. Therefore several precuts were applied which reduced the

π^0 multiplicity by a factor 10.
The final study is performed on a MC12b, mixed sample with a π^0 multiplicity of ~ 200, but the preselection has stayed the same. The coming Section gives an overview on the applied cuts for the preselection and their impact on the π^0 multiplicity.

First of all, one event cut is applied. This is the so-called hadron skim. It makes sure, that only hadronic events are considered. It requires for example that the event has at least three tracks which gets rid of all the $e^+e^- \rightarrow e^+e^-$ events.
After that, four cuts on photon variables are applied:

- clusterNHits > 1.5
- 0.2967 rad < clusterTheta < 2.6180 rad (in CDC acceptance)
- clusterE > 25 MeV
- |t/dt99| < 1.0

The clusterNHits cut is applied to require more than one crystal in the ECLCluster. Since clusterNHits is a float variable, it is necessary to require a float amount of crystals larger than 1 in the ECLCluster.
The clusterTheta cut makes sure that only ECLClusters within the acceptance of the CDC are taken into account since only for these tracking information from the CDC is available. Without any tracking information to an ECLCluster, it is very hard to tell whether the ECLCluster belongs to a charged or neutral particle.
clusterE > 25 MeV is applied to reduce the amount of photon candidates. Figure 5.1 shows that the majority of photons in this sample has energies of < 100 MeV. So each additional cut up to this value reduces the amount of photons drastically. Figure 5.2 shows the normalized clusterE distribution for the used sample up to 100 MeV with the applied precut visualized in red. Note that truth-matching is applied for this Figure and the photons are divided into signal and background photons. Background photons are shown in blue, signal photons in orange.
Since the cut |t/dt99| < 1.0 is already applied on software level for photons with energies less than 50 MeV, this cut is applied to all restly photons as well to reach consistency regarding this variable. The t/dt99 cut for the low energy photons is clearly visible as a step in the clusterE distribution shown in Figures 5.1 and 5.2. Applying this cut to all restly photons gets rid of this step, which can be seen in Figure 5.3. The normalized t/dt99 distribution and the applied cut can be seen in Figure 5.4 where truth-matching is applied and the photons are divided into signal and background photons. Signal photons are again shown in orange, background photons in blue.

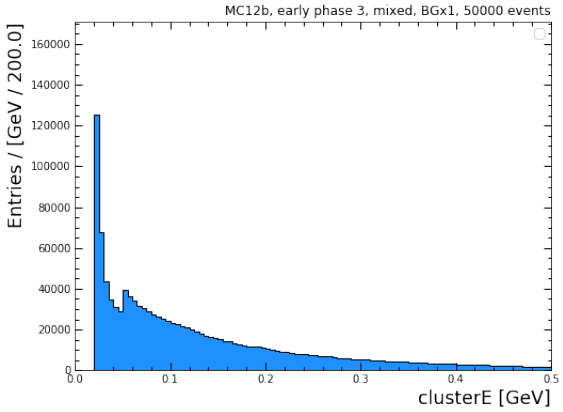

FIGURE 5.1. clusterE distribution without any cut applied for the used MC12b, mixed, early phase 3, BGx1, Monte Carlo sample. Note again the step at 50 MeV caused by the |t/dt99| < 1.0 cut for photons with energies less than 50 MeV.

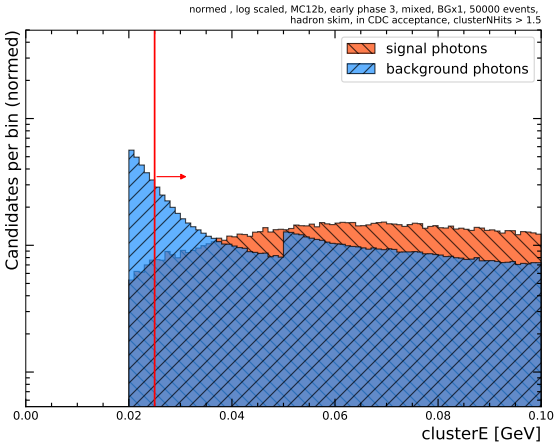

FIGURE 5.2. Normalized clusterE distribution for the used MC12b sample up to 100 MeV with the hadron skim, CDC acceptance cut and clusterNHits cut applied. Also truth-matching is applied and the photons are divided into signal and background photons. The precut on clusterE at 25 MeV is visualized in red.

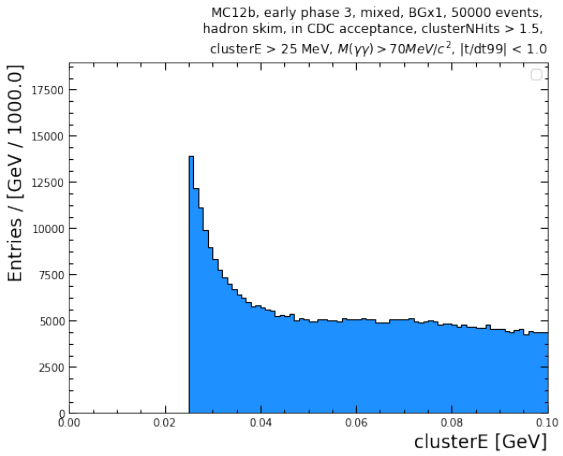

FIGURE 5.3. clusterE distribution after the application of all precuts for the used MC12b, mixed, early phase 3, BGx1, Monte Carlo sample. The step at 50 MeV due to the t/dt99 cut is gone.

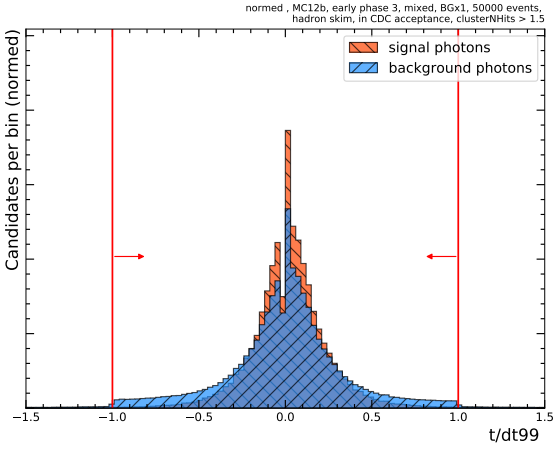

FIGURE 5.4. Normalized t/dt99 distribution with the hadron skim, CDC acceptance cut and clusterNHits cut applied for the used sample. The precut on t/dt99 is visualized in red. Signal and background photons are divided via truth-matching.

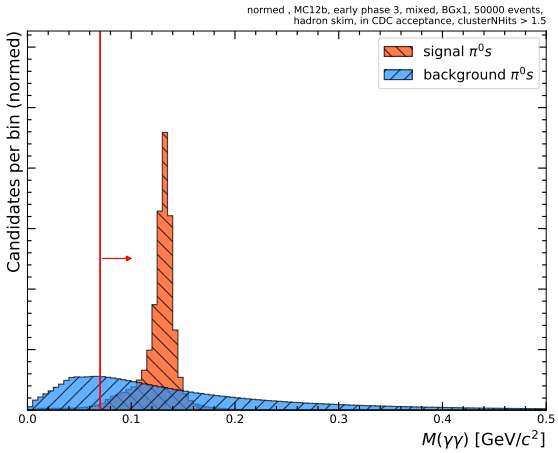

FIGURE 5.5. InvM distribution for the used MC12b sample with the hadron skim, CDC acceptance cut and clusterNHits cut applied. The precut on InvM is visualized in red. Note the huge amount of background π^0s with InvM < 100 MeV/c^2. Truth-matching is applied and the photons are divided into signal and background photons.

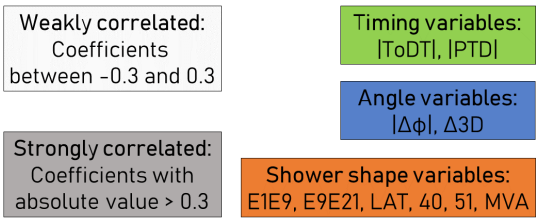

FIGURE 5.6. Correlation and variable categories used in the variable correlation study.

Finally, one cut on a π^0 variable is applied. This is the reconstructed mass of the π^0 (InvM or $M(\gamma\gamma)$). InvM > 70 MeV/c^2 is applied to drastically reduce the amount of π^0 candidates. Figure 5.5 shows the normalized InvM distribution for the used sample where the applied precut is shown in red. Again truth-matching is applied and the candidates are split into signal and background. Signal is shown in orange, background in blue. Note that the majority of background π^0s has InvM values < 100 MeV/c^2.

Table 5.1 shows the impact of the different preselections on the π^0 multiplicity as well as the efficiency and purity of the sample. The preselection reduces the π^0 multiplicity by a factor ~ 2 and the efficiency by $\sim 7\,\%$ while it almost doubles the purity. To quantify which variable cut of the variables clusterE, t/dt99 and InvM cuts the most π^0 candidates, these cuts are considered separately after applying the hadron skim, the CDC acceptance cut and the clusterNHits cut. The numbers show that, when applied solely, the InvM cut is the most powerful in this case, followed by the clusterE cut and the cut on t/dt99. If two of the cuts are applied, the combination InvM - t/dt99 is the most powerful, followed by the combinations InvM - clusterE and clusterE - t/dt99.

Figure 5.7 shows the working points for the currently implemented generic π^0 lists in basf2 like already shown in Section 4.3 but with the working point for the applied preselection added.

selection	**π^0 multiplicity**	**efficiency**	**purity**
no cuts	205.83	63.93 %	1.65 %
basic cuts (hadron skim, CDC acceptance and clusterNHits)	174.26	60.85 %	1.85 %
preselection	96.59	56.98 %	3.13 %
basic cuts plus clusterE cut	137.85	59.46 %	2.29 %
basic cuts plus t/dt99 cut	152.66	59.72 %	2.08 %
basic cuts plus InvM cut	127.90	59.31 %	2.46 %
preselection without clusterE cut	111.19	58.25 %	2.78 %
preselection without t/dt99 cut	112.24	58.03 %	2.75 %
preselection without InvM cut	118.80	58.36 %	2.61 %

TABLE 5.1. The numbers for π^0 multiplicity, efficiency and purity for the different selections are listed.

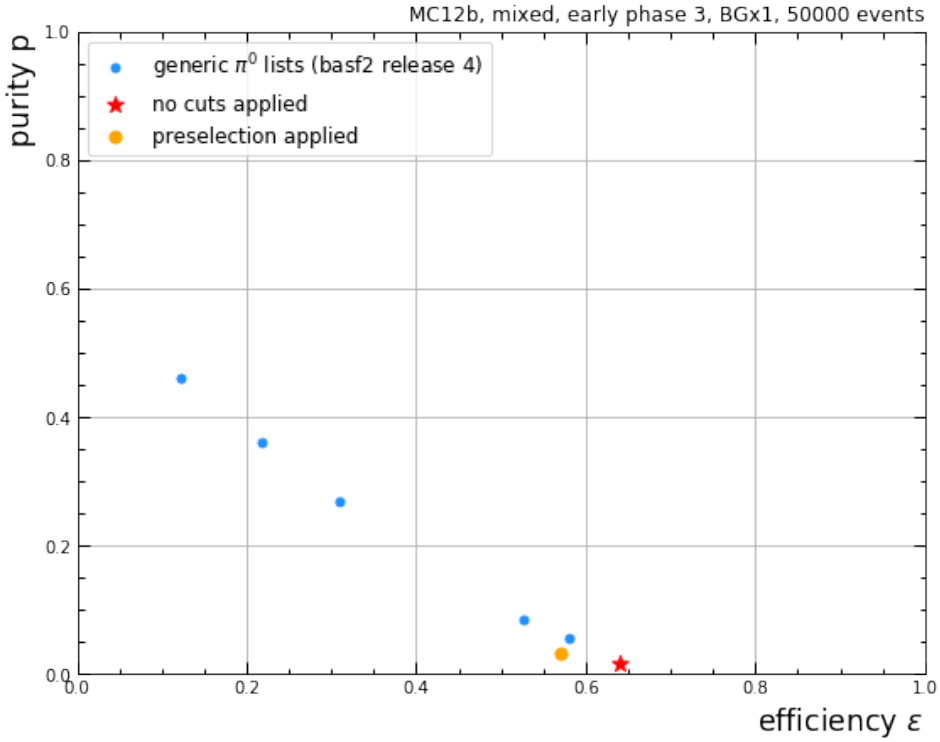

FIGURE 5.7. Visualization of the working points defined by the generic π^0 lists provided in basf2 in blue. The red star shows the working point for no selection applied. The yellow point marks the working point for the preselection.

5.2 Variable correlations

Since there are lots of possible cut variables in basf2 to use for the grid scan, this Section takes a closer look at the correlations between the single variables. The idea is to provide the optimized generic lists using almost uncorrelated variables to get the most out of the applied cuts. To quantify the correlations, the linear correlation coefficient *pearson's r* is used which is briefly described in Section 5.2.1. Section 5.2.2 sets up some categories to make this study more overseeable and the approach and results of the study are presented in Section 5.2.3.

5.2.1 Linear correlation coefficient Pearson's r

The pearson correlation coefficient is defined via

$$\rho_{X,Y} = \frac{\mathrm{cov}(X,Y)}{\sigma_X \sigma_Y} \tag{5.1}$$

where (X, Y) is a pair of variables, $\mathrm{cov}(X,Y)$ is the covariance of X and Y, σ_X is the standard deviation of X and σ_Y is the standard deviation of Y. It measures the linear correlation between the variables X and Y. Note that no statement on non-linear correlation is possible with this coefficient. Pearson's r can have values between -1 and +1, where -1 means full negative linear correlation and +1 means full positive linear correlation.

In the case of cut variables, there are not just two variables X and Y but samples of paired data $\{(x_1,y_1),...,(x_n,y_n)\}$ consisting of n pairs of data tuples (x,y). In such a case one can use the empirical version of the correlation coefficient formula where the covariance $\mathrm{cov}(X,Y)$ gets replaced by the empirical covariance $\sum_{i=1}^{n}(x_i-\overline{x})(y_i-\overline{y})$ and the standard deviations σ_X and σ_Y get replaced by the empirical standard deviations $\sqrt{\sum_{i=1}^{n}(x_i-\overline{x})^2}$ and $\sqrt{\sum_{i=1}^{n}(y_i-\overline{y})^2}$, respectively. This yields

$$r_{x,y} = \frac{\sum_{i=1}^{n}(x_i-\overline{x})(y_i-\overline{y})}{\sqrt{\sum_{i=1}^{n}(x_i-\overline{x})^2}\sqrt{\sum_{i=1}^{n}(y_i-\overline{y})^2}} \tag{5.2}$$

as the formula for the empirical linear correlation coefficient $r_{x,y}$, where n is the sample size, x_i and y_i are the individual sample points indexed with i and $\overline{x} = \frac{1}{n}\sum_{i=1}^{n}x_i$ and $\overline{y} = \frac{1}{n}\sum_{i=1}^{n}y_i$ are the sample mean values for x and y, respectively. [34, 35]

5.2.2 Variable and correlation categories

The following variables are included in the variable study described in this chapter:

- clusterE
- clusterE1E9
- clusterE9E21

- clusterLAT
- clusterAbsZernikeMoment40
- clusterAbsZernikeMoment51
- clusterZernikeMVA
- GammasDeltaPhi
- GammasDelta3D
- t/dt99
- PTD
- (PTD$_{extended}$)

All of these variables are known from Chapters 3 and 4 except for the $PTD_{extended}$ variable. This variable is a π^0 variable and defined via

$$PTD_{extended} = \frac{PTD}{\sqrt{(t/dt99)^2_{\gamma_1} + (t/dt99)^2_{\gamma_2}}} \tag{5.3}$$

where PTD is the PTD value of the π^0 candidate and $(t/dt99)^2_{\gamma_1}$ and $(t/dt99)^2_{\gamma_2}$ are the t/dt99 values of the two daughter photons. This variable was introduced with the hope that it combines the advantages of the PTD and t/dt99 variables and cancels out their disadvantages. The PTD variable is strongly energy dependent which can be seen in Section 5.4 whereas t/dt99 strongly depends on the detector timing calibration when applied on real data.
The clusterE variable has a special status among the listed variables. No correlations between clusterE and the other variables are investigated but correlations for different clusterE bins. Therefore clusterE is divided into the 5 following bins:

- 25 MeV - 50 MeV
- 50 MeV - 100 MeV
- 100 MeV - 150 MeV
- 150 MeV - 200 MeV
- 200 MeV - 3 GeV

Only symmetric bins are investigated, meaning both daughter photons of a π^0 candidate have energies within the respective clusterE bin.
Note that the InvM variable is not part of the correlation study since it will be part of the selection variables anyway.

The listed variables are categorized as follows. clusterE1E9 (E1E9), clusterE9E21 (E9E21), clusterLAT (LAT), clusterAbsZernikeMoment40 (40), clusterAbsZernikeMoment51 (51) and clusterZernikeMVA (MVA) make up the category of *shower shape variables*, GammasDeltaPhi ($\Delta\phi$) and GammasDelta3D ($\Delta 3D$) are the category of *angle variables* and t/dt99, PTD and $\text{PTD}_{extended}$ (PTD_e) represent the category of *timing variables*. Since GammasDeltaPhi, t/dt99, PTD and $\text{PTD}_{extended}$ are symmetrical around 0, their absolute values are used for this correlation study. Otherwise all linear correlation would cancel out. The categorization is also shown in Figure 5.6.

Also two correlation categories are defined, *highly correlated* and *weakly correlated*. A variable pair is highly correlated if the absolute value of the correlation coefficient $r_{x,y}$ is > 0.3 for the different clusterE bins. If the absolute value of the correlation coefficient is ≤ 0.3 for the different bins, the combination is labeled weakly correlated. Note that this is just a personal choice and not justified by any model or calculation. The correlation categories are also shown in Figure 5.6.

5.2.3 Approach and results

In a first step, 2D histograms for the different variable combinations and energy bins are plotted. Also plots for the complete clusterE range are made. The π^0 candidates are divided into signal and background π^0s and there are independent histograms for each of them. The correlation coefficient $r_{x,y}$ is calculated for each 2D distribution as well in this step. Figure 5.8 shows an excerpt of the large amount of histograms. Note that there are combinations which are obviously linearly correlated, combinations that are obviously not linearly correlated and combinations where no statement is possible by just looking at the 2D histogram.

In a second step, the correlation coefficient for a variable combination is plotted versus the clusterE energy bins. Again, the π^0 candidates are divided into signal and background π^0s. Signal is visualized in orange, background in blue. Figure 5.9 shows an excerpt of these plots.

In the following, the results shall be represented organized by the categories introduced in Section 5.2.2.

The combinations of timing variables behave quite differently. The combination |t/dt99| - |PTD| is strongly correlated which can be seen in Figure 5.10. The combination t/dt99 - $\text{PTD}_{extended}$ is weakly correlated but the combination PTD - $\text{PTD}_{extended}$ is strongly correlated. Also the two angle variables show a high correlation. This can be seen in Figure 5.11. Table 5.2 provides the corresponding numbers for the signal π^0s, Table 5.3 for the background π^0s. Note that there are no entries for signal π^0s in the energy bin from 25 MeV to 50 MeV. This is due to very low statistics for signal π^0s in this bin. Physically it is not possible to have a π^0 decaying into two photons that both have an energy within this range meaning that the signal π^0s in this bin are wrongly matched candidates. Therefore the linear correlation coefficient is more or less random for signal π^0s in this bin. Dependent on the distribution of the few entries in this bin, the correlation can be highly correlated or not correlated at all. Therefore the numbers are plotted

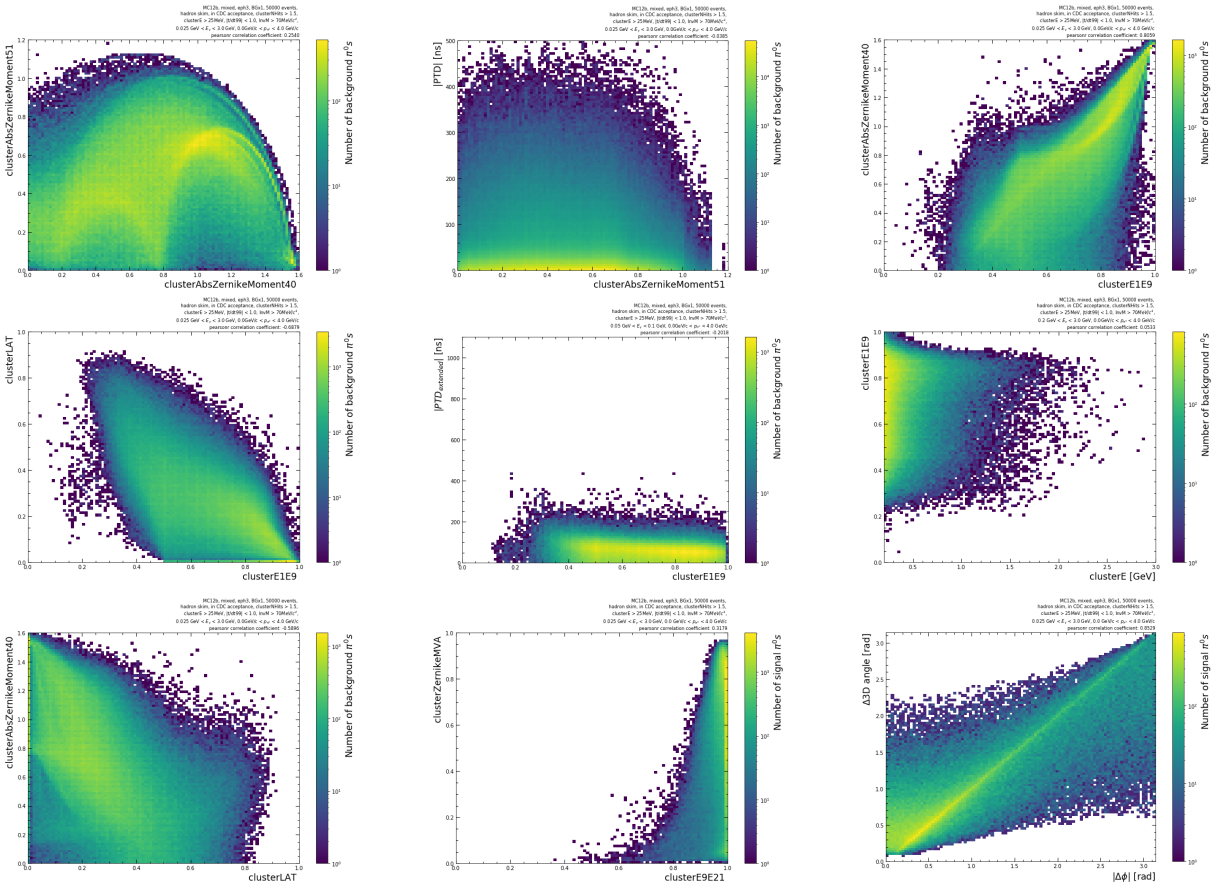

FIGURE 5.8. Selection of 2D histograms. Almost 800 of these plots were made. The plot details are written in the title labels of the single plots. Zoom in if you are interested.

for all the combinations but not provided in the Tables in this Section.

The shower shape variables are highly correlated among themselves as well but to a variable extent. This can be seen in Tables 5.4 and 5.5 for the signal and background π^0s, respectively. Figure 5.12 shows the correlation plot between clusterE1E9 and clusterAbsZernikeMoment40 as an example.

The interesting combinations happen among different categories. Figure 5.13 shows the correlation plot for the combination |t/dt99| - |GammasDeltaPhi|. Note that there is no statement possible and necessary about the gap between the signal and background correlation in the first energy bin since this is due to the low statistics for signal π^0s in this bin. The shown combination is clearly uncorrelated which is the same for any other timing - angle variable combination. The corresponding numbers are provided in Tables 5.6 and 5.7.

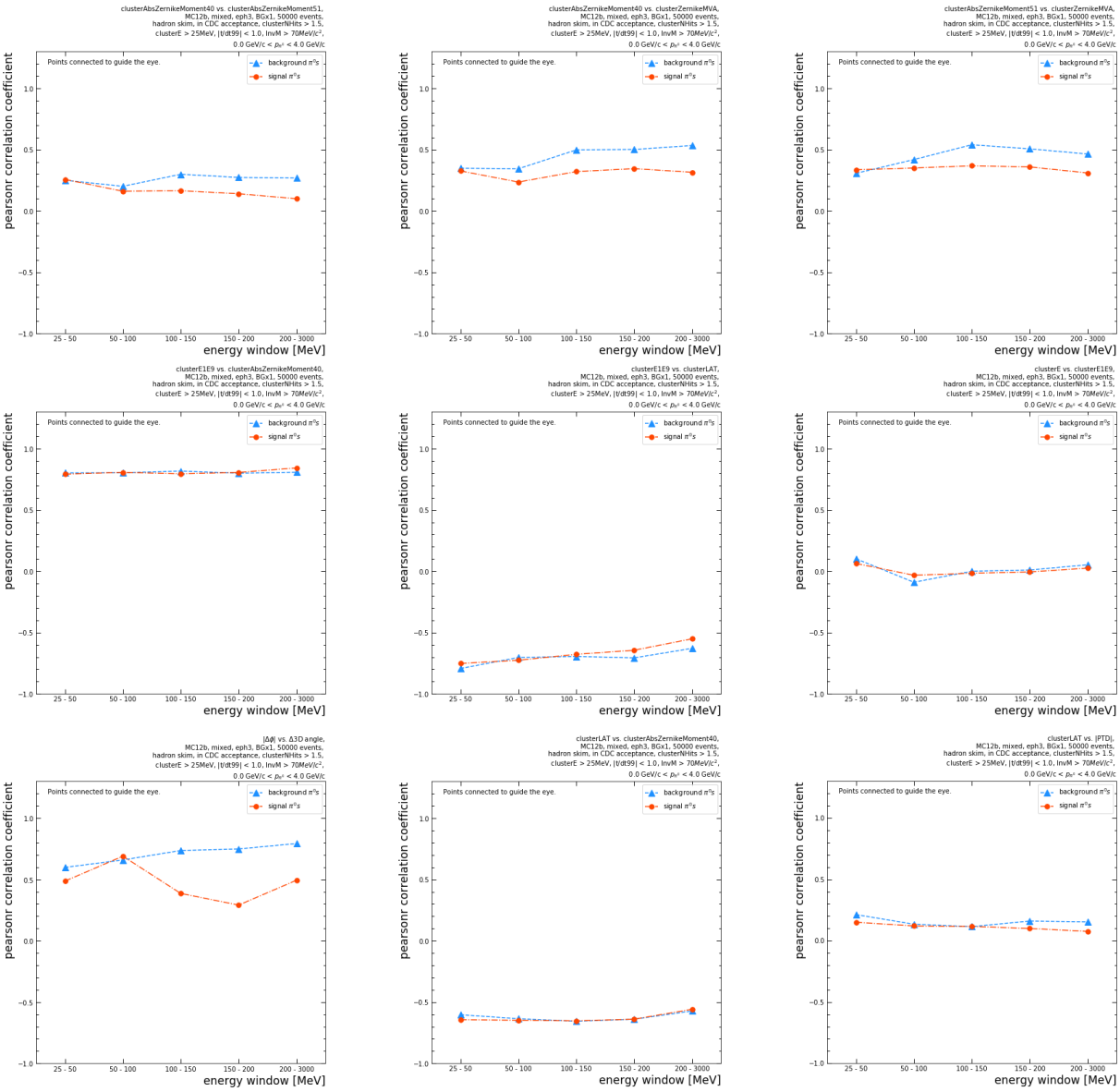

FIGURE 5.9. Selection of correlation coefficient versus photon energy bin plots. More than 60 of these plots were made. The data points are connected to guide the eye. Details are written in the title labels of the single plots. Zoom in if you are interested.

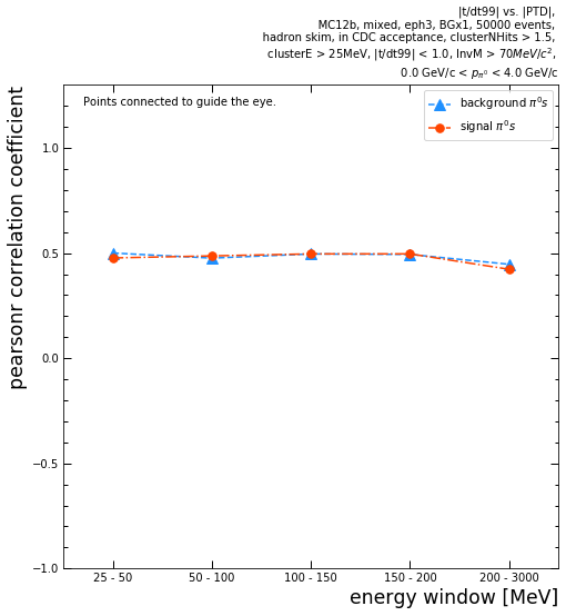

FIGURE 5.10. Correlation plot for the combination |t/dt99| - |PTD|. The two timing variables are highly correlated. Details can be found in the title label.

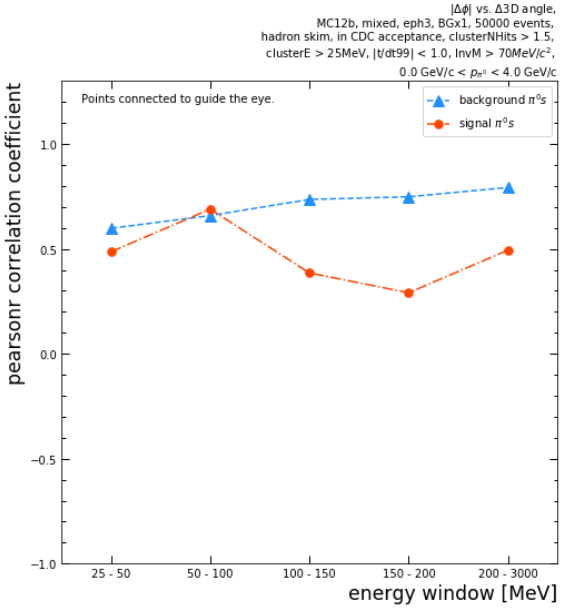

FIGURE 5.11. Correlation plot for the combination |GammasDeltaPhi| - GammasDelta3D. The two angle variables are highly correlated. Details can be found in the title label. Note that the correlation for the signal π^0s is energy dependent.

variable combination	**25 MeV - 3 GeV**	**25 MeV - 50 MeV**	**50 MeV - 100 MeV**	**100 MeV - 150 MeV**	**150 MeV - 200 MeV**	**200 MeV - 3 GeV**
t/dt99 - PTD	0.3590	/	0.4870	0.4965	0.4967	0.4234
t/dt99 - PTD$_e$	0.0516	/	-0.0074	0.0305	0.0549	0.1276
PTD - PTD$_e$	0.3360	/	0.4174	0.2511	0.1693	0.1545
$\Delta\phi$ - $\Delta 3D$	0.8529	/	0.6898	0.3857	0.2912	0.4942

TABLE 5.2. **Signal** correlation coefficients for **timing - timing** and **angle - angle** variable combinations.

variable combination	**25 MeV - 3 GeV**	**25 MeV - 50 MeV**	**50 MeV - 100 MeV**	**100 MeV - 150 MeV**	**150 MeV - 200 MeV**	**200 MeV - 3 GeV**
t/dt99 - PTD	0.3807	0.5007	0.4765	0.4963	0.4941	0.4471
t/dt99 - PTD$_e$	0.1448	0.1266	0.0128	0.0158	0.0406	0.0927
PTD - PTD$_e$	0.6511	0.7000	0.4980	0.3168	0.2242	0.1451
$\Delta\phi$ - $\Delta 3D$	0.7221	0.5984	0.6590	0.7361	0.7487	0.7930

TABLE 5.3. **Background** correlation coefficients for **timing - timing** and **angle - angle** variable combinations.

variable combination	**25 MeV - 3 GeV**	**25 MeV - 50 MeV**	**50 MeV - 100 MeV**	**100 MeV - 150 MeV**	**150 MeV - 200 MeV**	**200 MeV - 3 GeV**
E1E9 - E9E21	0.3502	/	0.3913	0.3564	0.3811	0.3205
E1E9 - LAT	-0.6409	/	-0.7186	-0.6732	-0.6308	-0.5533
E1E9 - 40	0.8172	/	0.8054	0.7905	0.8028	0.8447
E1E9 - 51	0.5092	/	0.5109	0.5159	0.5044	0.4739
E1E9 - MVA	0.3185	/	0.2795	0.3462	0.3871	0.3570
E9E21 - LAT	-0.6305	/	-0.6223	-0.6483	-0.6948	-0.6899
E9E21 - 40	0.4690	/	0.5120	0.5368	0.5224	0.4372
E9E21 - 51	0.2464	/	0.3132	0.2403	0.2055	0.1674
E9E21 - MVA	0.3162	/	0.3768	0.4084	0.4192	0.3561
LAT - 40	-0.5908	/	-0.6445	-0.6487	-0.6190	-0.5612
LAT - 51	-0.3133	/	-0.3714	-0.3133	-0.2604	-0.2139
LAT - MVA	-0.1940	/	-0.2605	-0.3276	-0.3687	-0.3161
40 - 51	0.1396	/	0.1592	0.1540	0.1250	0.0951
40 - MVA	0.2928	/	0.2308	0.3060	0.3254	0.3171
51 - MVA	0.3124	/	0.3465	0.3771	0.3456	0.3222

TABLE 5.4. **Signal** correlation coefficients for **shower shape - shower shape** variable combinations.

variable combination	**25 MeV - 3 GeV**	**25 MeV - 50 MeV**	**50 MeV - 100 MeV**	**100 MeV - 150 MeV**	**150 MeV - 200 MeV**	**200 MeV - 3 GeV**
E1E9 - E9E21	0.3373	0.3020	0.3598	0.3492	0.4033	0.3782
E1E9 - LAT	-0.6881	-0.7922	-0.7034	-0.6969	-0.7038	-0.6305
E1E9 - 40	0.8061	0.8021	0.8051	0.8177	0.7996	0.8081
E1E9 - 51	0.5678	0.5910	0.5327	0.5767	0.5605	0.5677
E1E9 - MVA	0.4727	0.3807	0.4117	0.5591	0.5431	0.5335
E9E21 - LAT	-0.5584	-0.4516	-0.5550	-0.5440	-0.6370	-0.6705
E9E21 - 40	0.4466	0.3724	0.4764	0.4959	0.5276	0.5031
E9E21 - 51	0.2999	0.3081	0.2805	0.2847	0.3214	0.3112
E9E21 - MVA	0.3689	0.3580	0.3472	0.3989	0.4900	0.5056
LAT - 40	-0.5900	-0.6008	-0.6359	-0.6574	-0.6349	-0.5720
LAT - 51	-0.3666	-0.4656	-0.3383	-0.3292	-0.3355	-0.3335
LAT - MVA	-0.3210	-0.3460	-0.2947	-0.4101	-0.4681	-0.4653
40 - 51	0.2524	0.2432	0.1980	0.2939	0.2786	0.2681
40 - MVA	0.4465	0.3525	0.3433	0.4935	0.5005	0.5370
51 - MVA	0.4113	0.3133	0.4188	0.5348	0.5013	0.4682

TABLE 5.5. **Background** correlation coefficients for **shower shape - shower shape** variable combinations.

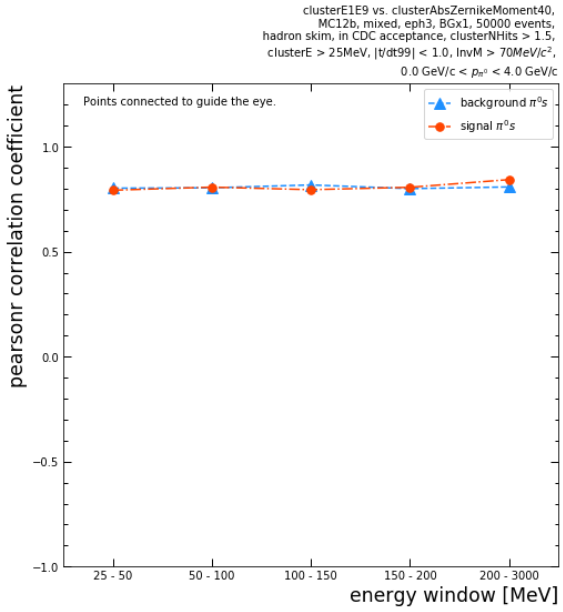

FIGURE 5.12. Correlation plot for the combination clusterE1E9 - clusterAbsZernikeMoment40. The two shower shape variables are highly correlated. Details can be found in the title label.

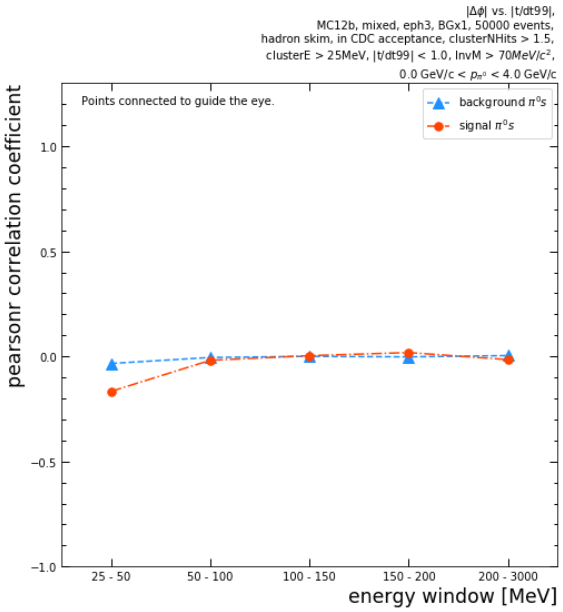

FIGURE 5.13. Correlation plot for the combination |t/dt99| - |GammasDeltaPhi|. The two variables are not correlated at all and therefore weakly correlated. Details can be found in the title label.

variable combination	**25 MeV - 3 GeV**	**25 MeV - 50 MeV**	**50 MeV - 100 MeV**	**100 MeV - 150 MeV**	**150 MeV - 200 MeV**	**200 MeV - 3 GeV**
t/dt99 - $\Delta\phi$	-0.0080	/	-0.0186	0.0036	0.0183	-0.0153
t/dt99 - $\Delta 3D$	-0.0081	/	-0.0070	0.0406	0.0245	-0.0385
PTD - $\Delta\phi$	0.2867	/	0.0027	0.0193	0.0137	0.1101
PTD - $\Delta 3D$	0.3545	/	0.0511	0.0704	0.0559	0.2578
PTD_e - $\Delta\phi$	0.2193	/	0.0188	-0.0035	-0.0117	0.0348
PTD_e - $\Delta 3D$	0.2706	/	0.0628	0.0329	0.0345	0.0859

TABLE 5.6. **Signal** correlation coefficients for **timing - angle** variable combinations.

The category combinations timing - shower shape and angle - shower shape also come out to be weakly correlated. Example correlation plots are shown in Figures 5.14 and 5.15. Again the difference for signal and background π^0s due to the very low signal statistics in the first energy bin is apparent. The corresponding numbers can be found in Tables 5.8 and 5.10 for the timing - shower shape variable combinations and in Tables 5.9 and 5.11 for the angle - shower shape variable combinations.

variable combination	**25 MeV - 3 GeV**	**25 MeV - 50 MeV**	**50 MeV - 100 MeV**	**100 MeV - 150 MeV**	**150 MeV - 200 MeV**	**200 MeV - 3 GeV**
t/dt99 - $\Delta\phi$	0.0076	-0.0336	-0.0049	0.0004	-0.0020	0.0041
t/dt99 - $\Delta 3D$	0.0291	0.0698	0.0043	0.0002	-0.0023	0.0013
PTD - $\Delta\phi$	0.0345	-0.0338	-0.0099	-0.0025	-0.0036	-0.0033
PTD - $\Delta 3D$	0.1341	0.1494	0.0445	0.0269	0.0193	0.0237
PTD_e - $\Delta\phi$	0.0416	-0.0092	-0.0070	-0.0042	0.0010	-0.0017
PTD_e - $\Delta 3D$	0.1366	0.1471	0.0526	0.0233	0.0108	0.0089

TABLE 5.7. **Background** correlation coefficients for **timing - angle** variable combinations.

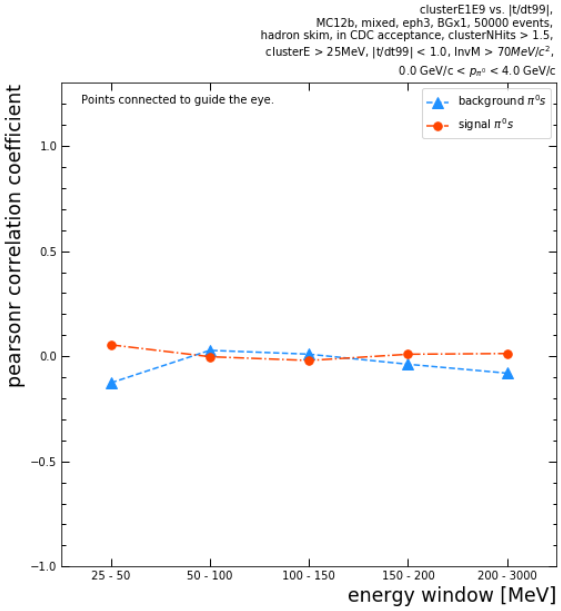

FIGURE 5.14. Correlation plot for the combination t/dt99 - clusterE1E9. The two variables are clearly uncorrelated. Details can be found in the title label.

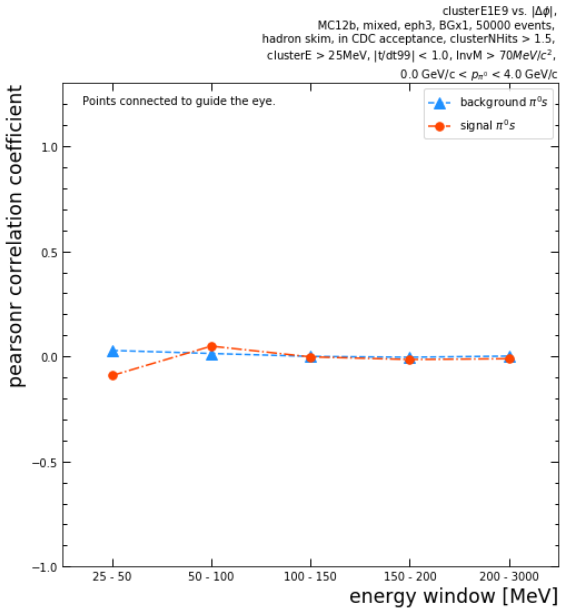

FIGURE 5.15. Correlation plot for the combination |GammasDeltaPhi| - clusterE1E9. The two variables are clearly uncorrelated. Details can be found in the title label.

Altogether one can say that this variable study turns out like expected. The different variable categories are highly correlated among themselves (if one leaves out the variable $PTD_{extended}$) and weakly correlated among each other. For optimizing a selection it is therefore recommended to combine variables out of different categories and to use the least correlated combinations if combinations of variables out of the same category are used.

variable combination	**25 MeV - 3 GeV**	**25 MeV - 50 MeV**	**50 MeV - 100 MeV**	**100 MeV - 150 MeV**	**150 MeV - 200 MeV**	**200 MeV - 3 GeV**
t/dt99 - E1E9	0.0036	/	-0.0020	-0.0200	0.0097	0.0131
t/dt99 - E9E21	-0.0050	/	-0.0076	-0.0163	0.0120	0.0057
t/dt99 - LAT	0.0149	/	0.0120	0.0286	0.0106	0.0038
t/dt99 - 40	0.0027	/	-0.0099	-0.0184	0.0164	0.0147
t/dt99 - 51	0.0036	/	0.0137	-0.0059	0.0097	0.0074
t/dt99 - MVA	0.0049	/	-0.0106	-0.0175	0.0087	0.0062
PTD - E1E9	-0.1094	/	-0.1473	-0.1336	-0.1359	-0.1325
PTD - E9E21	-0.0288	/	-0.0878	-0.0725	-0.0797	-0.0587
PTD - LAT	0.0274	/	0.1206	0.1164	0.0998	0.0761
PTD - 40	-0.0995	/	-0.1154	-0.1128	-0.1019	-0.1144
PTD - 51	-0.0517	/	-0.0750	-0.0678	-0.0855	-0.0799
PTD - MVA	-0.1418	/	-0.0780	-0.0755	-0.0907	-0.0614
PTD_e - E1E9	-0.0787	/	-0.1865	-0.1108	-0.0140	-0.0371
PTD_e - E9E21	-0.0170	/	-0.1009	-0.0587	-0.0200	-0.0159
PTD_e - LAT	0.0091	/	0.1431	0.0901	0.0069	0.0160
PTD_e - 40	-0.0738	/	-0.1436	-0.0916	-0.0105	-0.0353
PTD_e - 51	-0.0388	/	-0.1067	-0.0590	-0.0245	-0.0218
PTD_e - MVA	-0.1040	/	-0.0837	-0.0635	-0.0092	-0.0121

TABLE 5.8. **Signal** correlation coefficients for **timing - shower shape** variable combinations.

variable combination	**25 MeV - 3 GeV**	**25 MeV - 50 MeV**	**50 MeV - 100 MeV**	**100 MeV - 150 MeV**	**150 MeV - 200 MeV**	**200 MeV - 3 GeV**
$\Delta\phi$ - E1E9	0.0106	/	0.0490	-0.0020	-0.0147	-0.0109
$\Delta\phi$ - E9E21	0.0530	/	0.0478	-0.0013	-0.0288	-0.0182
$\Delta\phi$ - LAT	-0.1313	/	-0.0517	-0.0081	0.0064	-0.0233
$\Delta\phi$ - 40	-0.0147	/	0.0477	-0.0010	-0.0168	-0.0174
$\Delta\phi$ - 51	0.0166	/	0.0289	-0.0066	0.0037	-0.0153
$\Delta\phi$ - MVA	-0.1948	/	0.0523	-0.0159	-0.0258	-0.0262
$\Delta 3D$ - E1E9	0.0099	/	0.0608	0.0157	-0.0137	-0.0187
$\Delta 3D$ - E9E21	0.0602	/	0.0531	-0.0162	-0.0665	-0.0208
$\Delta 3D$ - LAT	-0.1469	/	-0.0574	0.0195	0.0331	-0.0424
$\Delta 3D$ - 40	-0.0221	/	0.0514	-0.0127	-0.0280	-0.0443
$\Delta 3D$ - 51	0.0192	/	0.0464	0.0184	0.0053	-0.0228
$\Delta 3D$ - MVA	-0.2283	/	0.0492	0.0055	-0.0280	-0.0279

TABLE 5.9. **Signal** correlation coefficients for **angle - shower shape** variable combinations.

variable combination	**25 MeV - 3 GeV**	**25 MeV - 50 MeV**	**50 MeV - 100 MeV**	**100 MeV - 150 MeV**	**150 MeV - 200 MeV**	**200 MeV - 3 GeV**
t/dt99 - E1E9	-0.0629	-0.1265	0.0282	0.0100	-0.0379	-0.0803
t/dt99 - E9E21	-0.0181	-0.0534	-0.0034	-0.0027	-0.0564	-0.1251
t/dt99 - LAT	0.0359	0.1268	0.0064	-0.0100	0.0284	0.0919
t/dt99 - 40	-0.0770	-0.1194	0.0185	0.0054	-0.0525	-0.1067
t/dt99 - 51	-0.0165	-0.0477	0.0175	-0.0124	-0.0633	-0.0790
t/dt99 - MVA	-0.1289	-0.0805	-0.0257	-0.0611	-0.1469	-0.1897
PTD - E1E9	-0.1226	-0.2246	-0.1291	-0.1449	-0.1784	-0.1834
PTD - E9E21	-0.0110	-0.1161	-0.0841	-0.0828	-0.1457	-0.1743
PTD - LAT	0.0732	0.2130	0.1344	0.1150	0.1605	0.1537
PTD - 40	-0.1111	-0.1788	-0.1089	-0.1223	-0.1579	-0.1781
PTD - 51	-0.0385	-0.1241	-0.0654	-0.0981	-0.1260	-0.1385
PTD - MVA	-0.1000	-0.1276	-0.0791	-0.1240	-0.1799	-0.2192
PTD_e - E1E9	-0.1404	-0.2987	-0.2018	-0.1476	-0.1039	-0.0513
PTD_e - E9E21	-0.0137	-0.1547	-0.1143	-0.0788	-0.0756	-0.0352
PTD_e - LAT	0.0727	0.2658	0.1804	0.1180	0.0920	0.0341
PTD_e - 40	-0.1244	-0.2343	-0.1657	-0.1234	-0.0865	-0.0464
PTD_e - 51	-0.0495	-0.1824	-0.1052	-0.0915	-0.0661	-0.0365
PTD_e - MVA	-0.1201	-0.1615	-0.0962	-0.0959	-0.0768	-0.0535

TABLE 5.10. **Background** correlation coefficients for **timing - shower shape** variable combinations.

variable combination	**25 MeV - 3 GeV**	**25 MeV - 50 MeV**	**50 MeV - 100 MeV**	**100 MeV - 150 MeV**	**150 MeV - 200 MeV**	**200 MeV - 3 GeV**
$\Delta\phi$ - E1E9	0.0030	0.0284	0.0140	0.0002	-0.0037	0.0016
$\Delta\phi$ - E9E21	0.0131	0.0419	0.0125	0.0009	-0.0040	0.0011
$\Delta\phi$ - LAT	-0.0184	-0.0349	-0.0156	-0.0021	0.0014	-0.0006
$\Delta\phi$ - 40	0.0009	0.0251	0.0137	-0.0010	-0.0042	0.0024
$\Delta\phi$ - 51	0.0065	0.0140	0.0094	0.0004	-0.0050	0.0004
$\Delta\phi$ - MVA	-0.0200	0.0277	0.0089	-0.0034	-0.0079	0.0008
$\Delta 3D$ - E1E9	-0.0074	-0.0396	0.0091	0.0018	-0.0001	0.0016
$\Delta 3D$ - E9E21	0.0154	0.0027	0.0043	-0.0025	-0.0027	-0.0022
$\Delta 3D$ - LAT	-0.0104	0.0263	0.0026	0.0109	0.0132	0.0100
$\Delta 3D$ - 40	-0.0144	-0.0419	0.0031	-0.0019	-0.0021	-0.0028
$\Delta 3D$ - 51	0.0108	-0.0090	0.0172	0.0059	-0.0001	0.0029
$\Delta 3D$ - MVA	-0.0418	-0.0373	0.0053	0.0004	-0.0021	-0.0023

TABLE 5.11. **Background** correlation coefficients for **angle - shower shape** variable combinations.

5.3 Variable distributions and figure of merits

Additionally to the large amount of cut variables every variable has an infinite amount of possible cut values. This makes the purpose of running a full grid scan on the cut variables and values even more difficult. Technically it is not possible to scan thousands of values for each variable. Therefore it is essential to get an idea of which cut values are 'good' and which are 'bad'. This question shall be treated in the following Section. While Section 5.3.1 answers this question in a purely qualitative way, Section 5.3.2 introduces a method to answer the question quantitatively. The results using the variables introduced in Section 5.2.2 are provided in Section 5.3.3.

5.3.1 1D Histograms

The goal of a good variable selection is to get rid of as much background as possible and to be left with as much signal as possible. This means in a perfect world the selection would cut the complete background and leave the signal untouched. Unfortunately this is not possible. So a short and simple definition for a 'good cut' would be a cut that leaves as much signal as possible compared to background.

The intuitive way to find 'good cuts' is to take a look at the variable distributions for signal and background in Monte Carlo. In Monte Carlo it is possible to divide the dataset into signal and background since it is just a simulation. Usually one takes a look at the normalized distributions to be able to compare the distribution shapes. If the absolute distributions are used usually no statement is possible since there is much less signal then background. This is also the reason why the normalized distributions for the preselection variables were shown in Section 5.1.

Dependent on the variable the signal and background distributions can be very similar, very different or something in between. Figure 5.16 shows the normalized distributions for GammasDelta3D. The shapes of the signal and background distributions are very different in this case and one would intuitively apply a highcut at $\sim 1.1\,\mathrm{rad}$ where the both distributions overlap. Highcut means setting a maximum value for the variable and cutting everything above this value. In contrast a lowcut means setting a minimum value and cutting everything below this value. The opposite is shown in Figure 5.17. It shows the normalized distributions for clusterAbsZernikeMoment51. In such a case it is very hard to make a statement which cut to apply. The best choice would again be the region where the two distributions overlap.

5.3.2 Figure of merits

The intuitive approach suggested in Section 5.3.1 quickly hits the wall like shown with Figure 5.17. A way to measure how a cut performs is to use so called *figure of merits*. A figure of merit quantifies the proportion of signal and background and therefore makes measurable whether a cut performs 'good' or 'bad'.

For the study performed in this Section two different figure of merits are considered which are

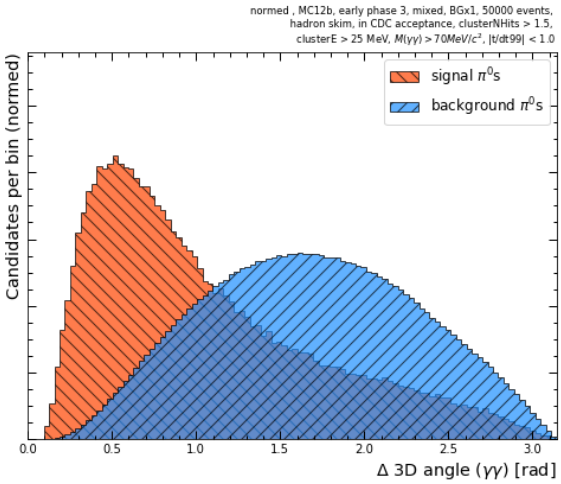

FIGURE 5.16. Normalized signal and background distributions for GammasDelta3D.

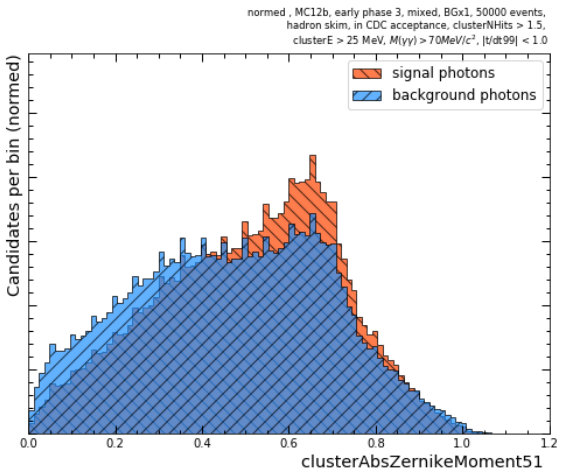

FIGURE 5.17. Normalized signal and background distributions for clusterAbsZernikeMoment51.

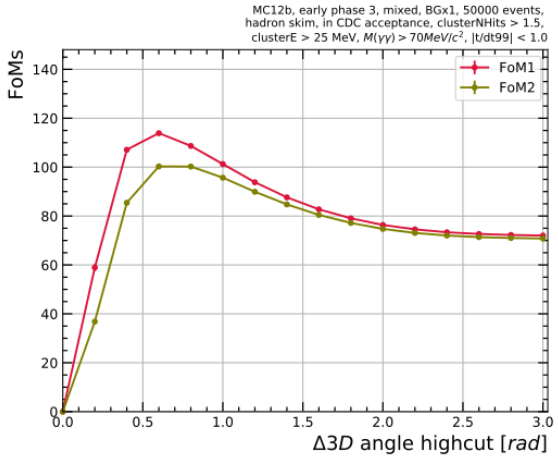

FIGURE 5.18. The two figure of merits for different GammasDelta3D highcuts.

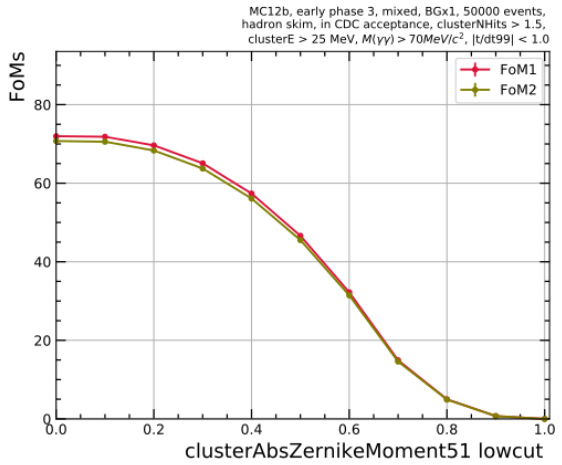

FIGURE 5.19. The two figure of merits for different clusterAbsZernikeMoment51 lowcuts.

defined in Equations 5.4 and 5.5 where FoM stands for figure of merit.

$$\text{FoM}_1 = \frac{\text{amount of signal } \pi^0 s}{\sqrt{\text{amount of background } \pi^0 s}} \tag{5.4}$$

$$\text{FoM}_2 = \frac{\text{amount of signal } \pi^0 s}{\sqrt{\text{amount of all } \pi^0 s}} \tag{5.5}$$

By calculating the figure of merit for different cut values one can find 'good cuts' or 'good cut regions' by maximizing the figure of merit(s). Figure 5.18 shows the two figure of merits for different GammasDelta3D highcuts. Note how the figure of merits peak in the region where one would have intuitively applied the cut regarding Figure 5.16.
Figure 5.19 shows the figure of merits for different clusterAbsZernikeMoment51 lowcuts as a counterexample. In this case the figure of merits quantitatively show the problem faced in Section 5.3.1. Due to the overlapping distributions it is hard to tell whether a cut performs 'good' or 'bad'. Following the figure of merits here, it would be the best to not perform a lowcut on clusterAbsZernikeMoment51 or to choose a value between 0.0 and 0.2 for the lowcut.

5.3.3 Results

In the following Section cuts on the single variables are investigated by using the two figure of merits introduced in Section 5.3.2. Principally there are three different types of cuts. One can apply a highcut, a lowcut or a combination of both. For axisymmetric distributions around 0, the combination usually results in a cut on the absolute value of the variable like performed on t/dt99 in Section 5.1.

The signal and background distributions as well as the figure of merits are shown. Additionally to the variables treated in Section 5.2, several more are investigated. These are InvM and region-dependent clusterE. The regional clusterE variables are named E_{BRL}, E_{FWD} and E_{BWD} for the barrel, the forward endcap and the backward endcap, respectively. For the sake of clarity only the plots for t/dt99 are shown here. They can be seen in Figure 5.20. The plots for all other variables can be found in Section A.1 of the appendix. The resulting 'good cut regions' of all variables are summed in Table 5.12. Note that the given numbers can only be seen as a first orientation. In the case of InvM for example, we will see tighter cuts then the given ones here in Chapter 6.

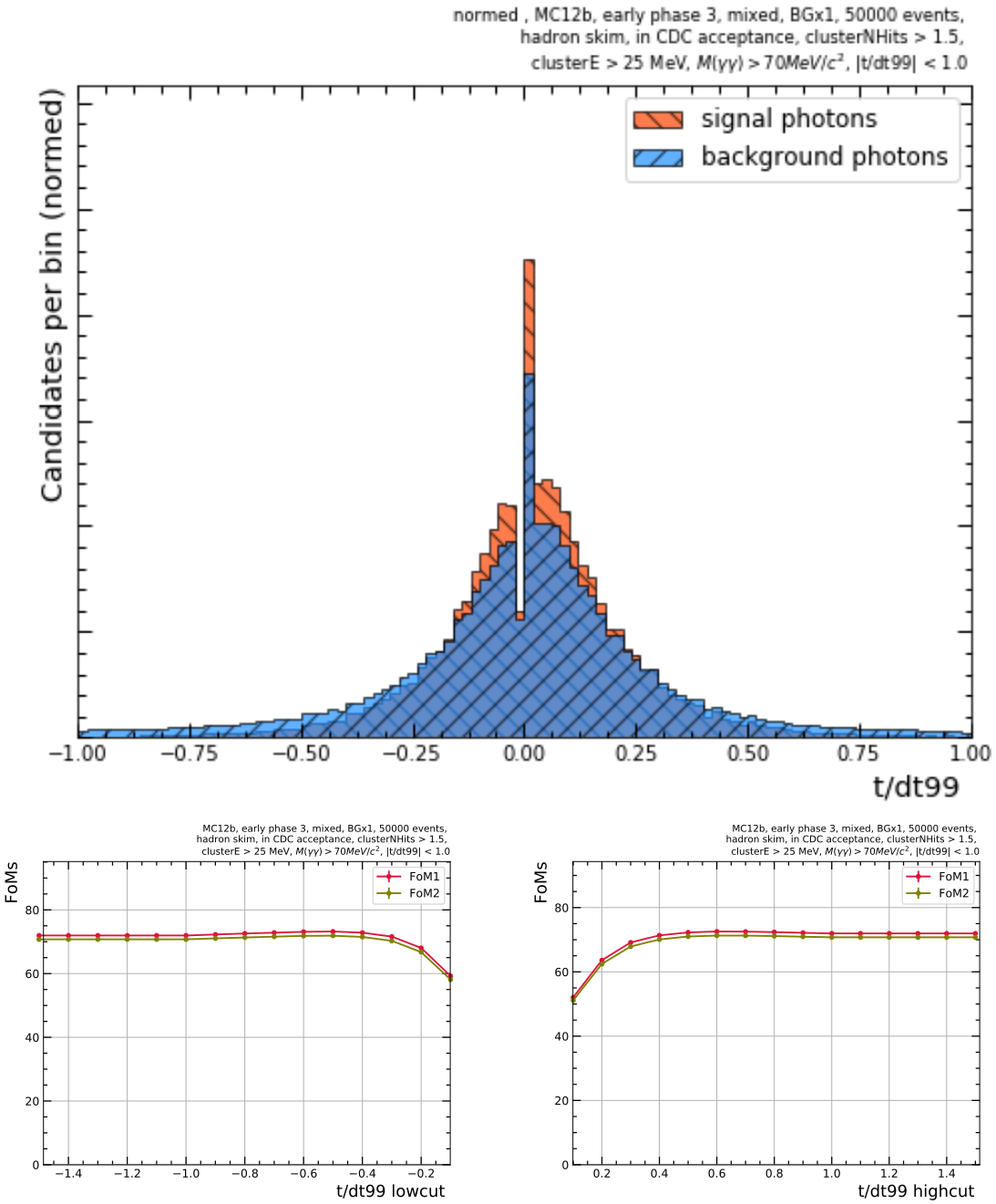

FIGURE 5.20. Signal and background distributions for t/dt99 (top). Figure of merits for t/dt99 lowcuts (bottom left) and highcuts (bottom right).

variable	**[unit]**	**lowcut**	**highcut**	**absolute value cut**
t/dt99		/	/	0.3 - 1.0
PTD	[ns]	/	/	25 - 300
$PTD_{extended}$	[ns]	/	/	100 - 1000
GammasDeltaPhi	[rad]	/	/	1.0 - 2.5
GammasDelta3D	[rad]	/	0.4 - 1.4	/
clusterE1E9		0.0 - 0.5	/	/
clusterE9E21		0.0 - 0.9	/	/
clusterLAT		/	0.4 - 1.0	/
clusterAbsZernikeMoment40		0.0 - 0.4	/	/
clusterAbsZernikeMoment51		/	/	/
clusterZernikeMVA		0.1 - 0.4	/	/
InvM	[MeV/c^2]	60 - 115	140 - 160	/
E_{BRL}	[MeV]	20 - 100	/	/
E_{FWD}	[MeV]	20 - 200	/	/
E_{BWD}	[MeV]	20 - 200	/	/

TABLE 5.12. 'Good cut regions' for the single variables based on the Monte Carlo variables study.

5.4 Efficiency loss per photon energy bin

The following side study came to life when an alternative to the two timing variables t/dt99 and PTD was searched. The alternative should combine the two variables which resulted in $PTD_{extended}$ described in Section 5.2.2.

t/dt99 is very dependent on the detector timing calibration if used on data which is not a problem if used on Monte Carlo since the timing calibration is considered to be perfect in Monte Carlo. Whereas PTD shows a large energy dependence which will be shown in this Section. The hope was that $PTD_{extended}$ combines the energy robustness of t/dt99 with the calibration independence of PTD. Therefore the efficiency loss per photon energy bin for different t/dt99, PTD and $PTD_{extended}$ cuts was investigated. The following plots show the 5 photon energy bins known from Sections 5.2.2 and 5.2.3 on the x-axis. On the y-axis you find the efficiency loss divided by the efficiency for the respective bin. Efficiency means the π^0 reconstruction efficiency explained in Section 4.3. The efficiency loss is calculated by the efficiency before applying the cut minus the efficiency after the cut application. Therefore the value on the y-axis is a number between 0 and 1 and tells what percentage of π^0s is cut by the applied cut for this energy bin.

Figures 5.21 and 5.22 show these efficiency loss plots for t/dt99 and PTD with several different cuts applied. While t/dt99 is very energy robust, PTD is very energy dependent. The PTD plot shows that higher energetic photon pairs have a smaller photon timing difference and therefore are ignored by the applied cuts. The efficiency loss per photon energy bin for $PTD_{extended}$ is shown in Figure 5.23. The energy dependence is even more complicated than in the case of PTD.

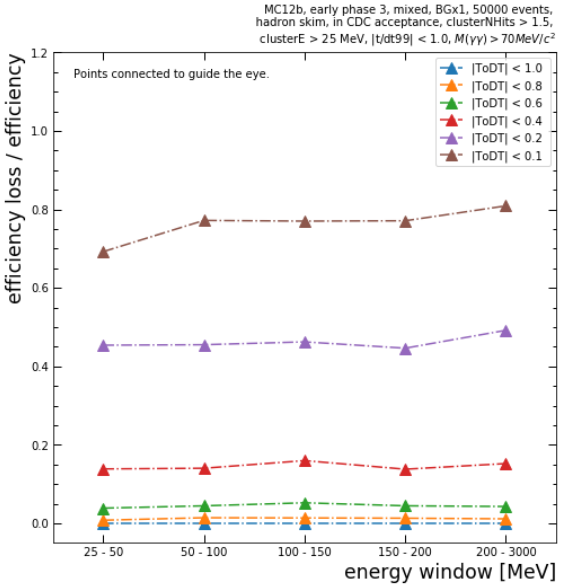

FIGURE 5.21. Efficiency loss per photon energy bin for different t/dt99 cuts. The different cuts are plotted in different colors. Data points are connected to guide the eye.

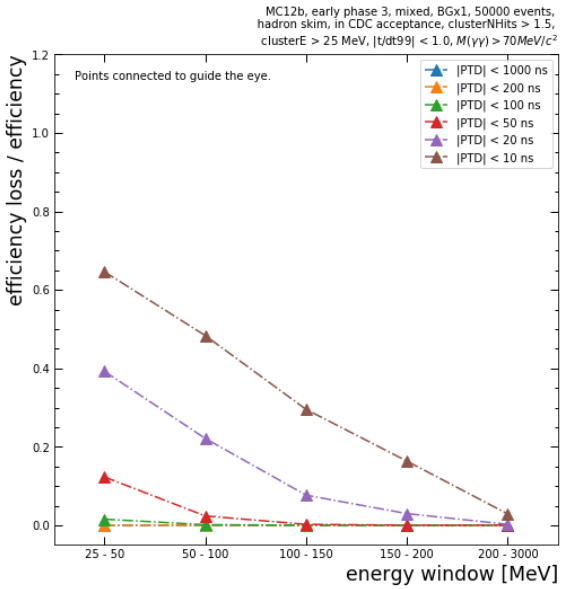

FIGURE 5.22. Efficiency loss per photon energy bin for different PTD cuts.

Since the efficiency loss plots give a good insight into the different variables, the plots were also made for all the other variables used in Section 5.2. These are presented in the following.

Figures 5.24 to 5.29 show the efficiency loss plots for the six shower shape variables. clusterLAT and clusterZernikeMVA show a cut dependent energy dependence. clusterE1E9, clusterE9E21, clusterAbsZernikeMoment40 and clusterAbsZernikeMoment51 are almost energy independent.

The efficiency loss plots for the two angle variables are shown in Figures 5.30 and 5.31. Both of them are highly energy and cut dependent. This is due to the physics of a π^0 decaying into two photons. Two high energetic photon daughters will have smaller angles between them then low energetic photon daughters do.

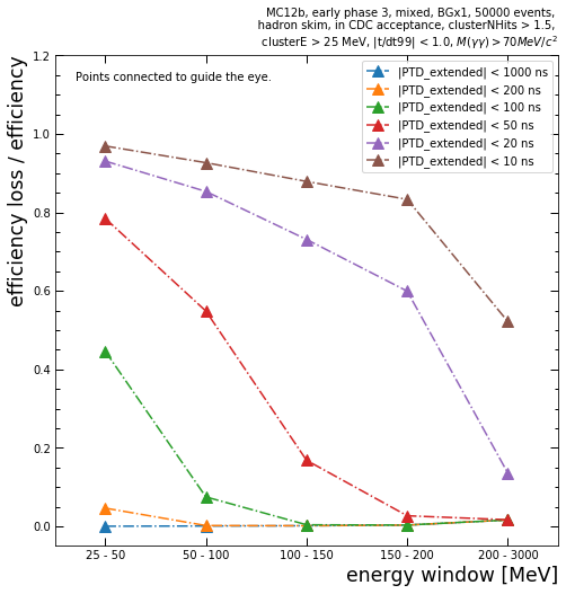

FIGURE 5.23. Efficiency loss per photon energy bin for different $\mathrm{PTD}_{extended}$ cuts.

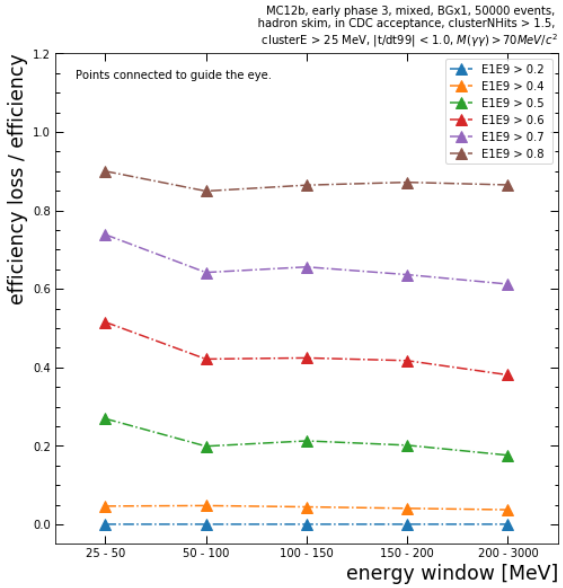

FIGURE 5.24. Efficiency loss per photon energy bin for different clusterE1E9 cuts.

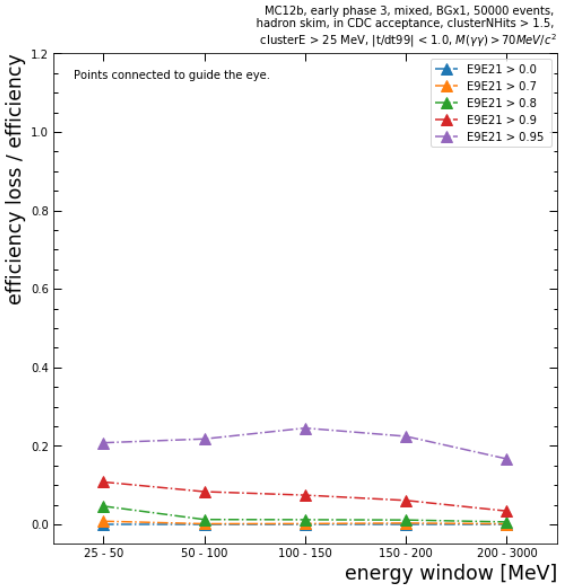

FIGURE 5.25. Efficiency loss per photon energy bin for different clusterE9E21 cuts.

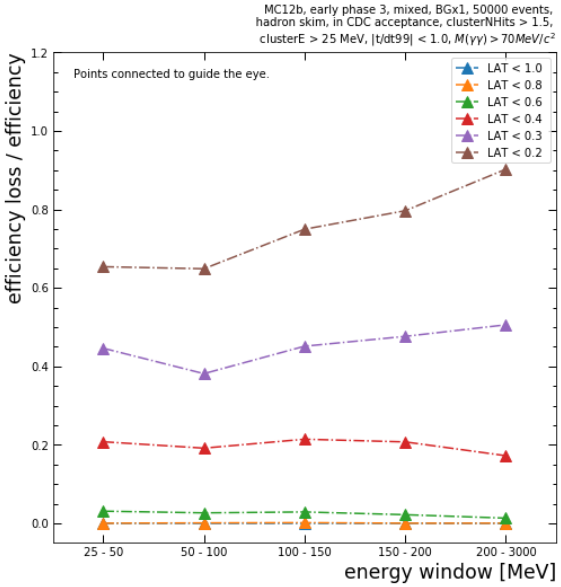

FIGURE 5.26. Efficiency loss per photon energy bin for different clusterLAT cuts.

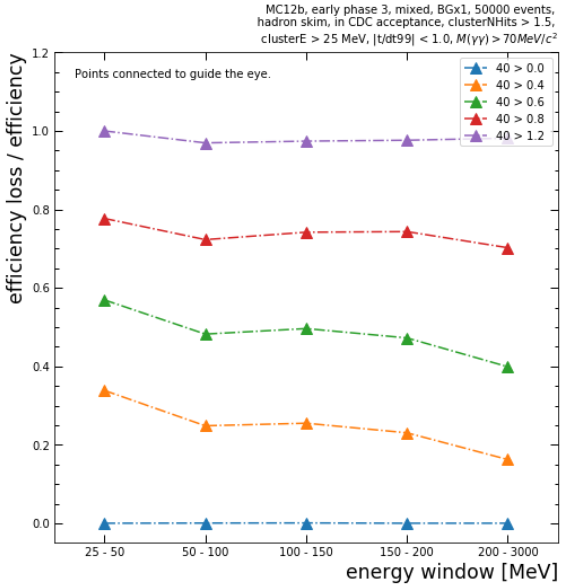

FIGURE 5.27. Efficiency loss per photon energy bin for different clusterAbsZernikeMoment40 cuts.

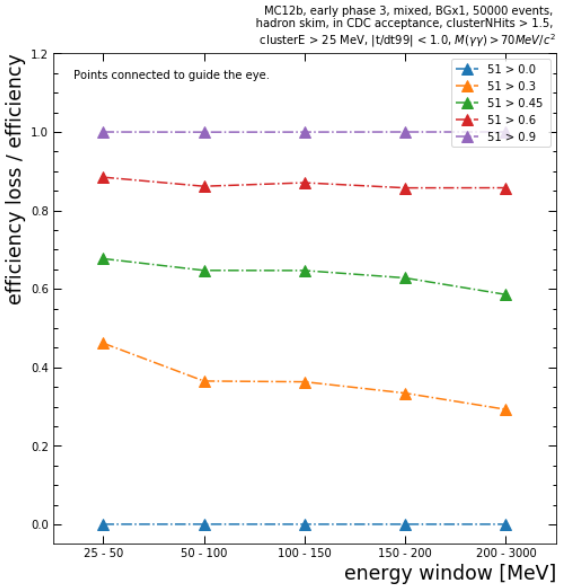

FIGURE 5.28. Efficiency loss per photon energy bin for different clusterAbsZernikeMoment51 cuts.

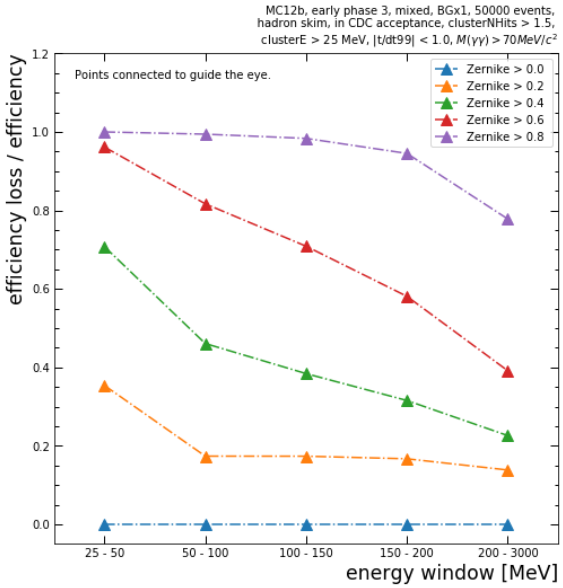

FIGURE 5.29. Efficiency loss per photon energy bin for different clusterZernikeMVA cuts.

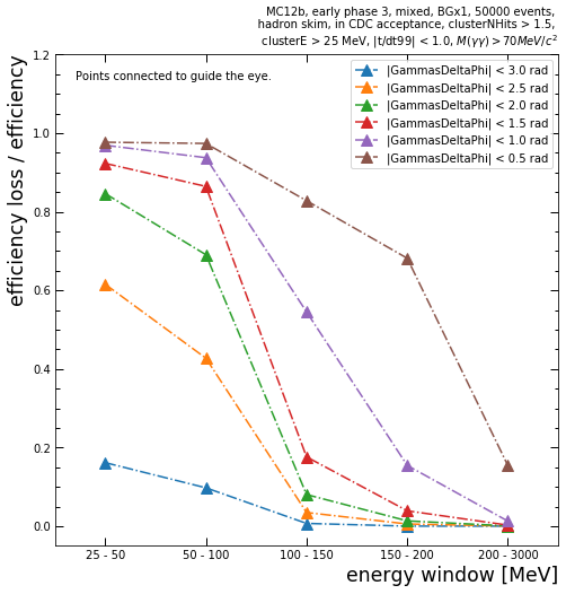

FIGURE 5.30. Efficiency loss per photon energy bin for different GammasDeltaPhi cuts.

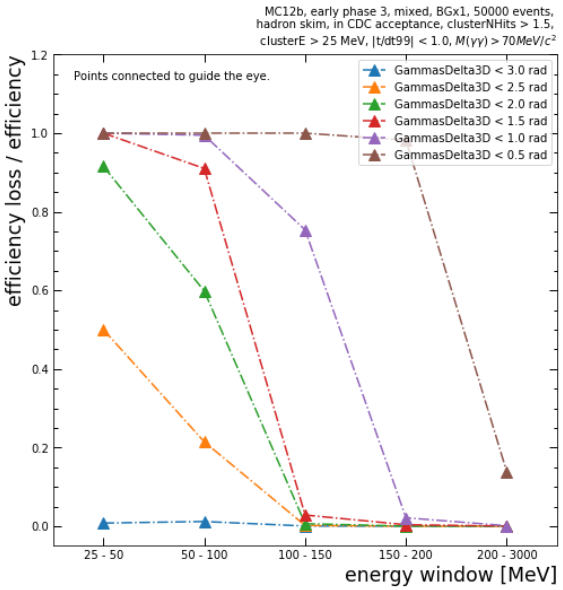

FIGURE 5.31. Efficiency loss per photon energy bin for different GammasDelta3D cuts.

CHAPTER 6

GRID SCAN

This Chapter treats the full grid scan on the cut variables and cut values investigated in Chapter 5 for the optimization of the generic π^0 reconstruction selections in basf2. The grid scan is performed on the MC12b, mixed, early phase 3, BGx1, Monte Carlo sample already used for Chapter 5, but this time with 200,000 events for more statistics. The preselection defined in Section 5.1 is applied as well.

Based on the results from Chapter 5, Section 6.1 introduces the variables and values used for the grid scan and clarifies the overall approach. The results of the grid scan as well as the final suggestions for the optimized π^0 reconstruction selections are represented in Section 6.2.1. Section 6.3 takes a look on the performance of the final suggestions on other Monte Carlo samples than the mixed sample.

6.1 Variables, values and approach

Performing a full grid scan means choosing a set of cut variables and cut values and checking the performance of each single configuration, i.e. calculating the π^0 reconstruction efficiency and purity. The grid scan serves for finding the highest possible purity value to six given efficiency values. These are: 60%, 50%, 40%, 30%, 20%, and 10%. The corresponding selections are referred to as eff60, eff50, eff40, eff30, eff20, and eff10.

Since the π^0 reconstruction efficiency is already below 60% after the preselection, the 60% list is treated separately in Section 6.1.3. Section 6.1.1 describes the grid scan approach using the software *HTCondor* and Section 6.1.2 defines the cut variables and cut values used for the grid scan.

6.1.1 Grid scan approach with HTCondor

Since the amount of configurations rises rapidly with the number of cut variables and cut values, a single computer quickly reaches the point where it takes an inappropriate amount of time to get the results of the grid scan. Hence, the software *HTCondor* in corporation with the computing power of the *NAF* (national analysis facility) at DESY is used. The *NAF* is a large batch facility providing huge computing resources and all experiment data present at DESY. The software *HTCondor* manages the distribution of computationally intensive tasks on the *NAF*. It takes the elementary parts, so-called jobs, of a task, distributes them on the *NAF*, and runs the jobs in parallel.

As a user, there are two controllable parameters: the amount of jobs and the runtime of a job. In practice, these two parameters are controlled with the use of an inner and outer programming script, where the outer script loops over the inner script for each job defined in the outer script. In the case of the grid scan, there is a bunch of variable cut configurations per job. The amount of variable cuts is mostly defined in the outer script to control the number of jobs, but also in the inner script to control the runtime of a job. Besides, the inner script loads the data file, performs the variable cuts, calculates the π^0 reconstruction efficiency and purity, and stores the results in a text file for later usage.

Due to priority settings on the *NAF* and to make the results reproducible in an appropriate amount of time, the number of jobs should not heavily exceed 10,000 and the runtime of the inner script should be of $\sim 1.5\,\mathrm{h}$.

6.1.2 Cut variable and cut value choice

A choice on cut variables and corresponding cut values is made to be used for the grid scan. The choice of variables is based on the results of the correlation study in Section 5.2. The ranges of the corresponding cut values are defined regarding the results from Section 5.3. The amount of cut values per variable and the exact values within the given ranges are chosen to fit the computing requirements from Section 6.1.1.

clusterE and InvM are chosen as the must-have variables, where clusterE is applied region-dependently. The single cuts are named E_{BRL}, E_{FWD}, and E_{BWD}. The cuts on clusterE are lowcuts, the cuts on InvM are both lowcuts and highcuts.
Additionally, one shower shape variable is considered for the grid scan, which is clusterE1E9. Due to the strong correlation among the shower shape variables, only one shower shape variable is considered. The cuts on clusterE1E9 have the character of a lowcut.
Since the angle variables are strongly correlated as well, only one of them is desired for the final selections. In the grid scan, both of them are implemented for comparing their performance. The cuts on GammasDeltaPhi are applied on the absolute value of the variable, the cuts on GammasDelta3D are highcuts.

The timing variables have a special status among the cut variables. At the time of writing this thesis, the timing calibration of the ECL is not exact enough to allow tight timing cuts. The variable distributions for data and Monte Carlo do not show large agreement, which is shown in Chapter 7. Thus, no tighter t/dt99 cuts than the one applied with the preselection are taken into account. In contrast, the PTD variable is considered as a possible upgrade in Section 6.2.2. Therefore the grid scan is performed with and without cuts on the PTD variable. The PTD cut is performed on the absolute value of the variable.

An overview on the used cut variables and the choice of the corresponding cut values can be found in Table 6.1. The chosen values for InvM need further explanation.

For InvM, way more cuts are considered than for the other variables. Starting from the rounded PDG value for the π^0 mass ($\sim 135\,\mathrm{MeV/c^2}$), 60 symmetric windows around this value are created by increasing and decreasing the value in $1\,\mathrm{MeV/c^2}$ steps. Thus the tightest symmetric window is $134\,\mathrm{MeV/c^2}$ - $136\,\mathrm{MeV/c^2}$ and $75\,\mathrm{MeV/c^2}$ - $195\,\mathrm{MeV/c^2}$ is the loosest one. Also differently asymmetric InvM windows are considered. Therefore the $1\,\mathrm{MeV/c^2}$ steps in both directions from the PDG value are altered. The following combinations are considered for the grid scan: $1\,\mathrm{MeV/c^2}$ to lower values and $1.5\,\mathrm{MeV/c^2}$ to higher values, $1.5\,\mathrm{MeV/c^2}$ to lower values and $1\,\mathrm{MeV/c^2}$ to higher values, $1\,\mathrm{MeV/c^2}$ to lower values and $2\,\mathrm{MeV/c^2}$ to higher values, and $2\,\mathrm{MeV/c^2}$ to lower values and $1\,\mathrm{MeV/c^2}$ to higher values. 60 asymmetric windows per step combination are considered.

variable	**[unit]**	**cut**	**values**	**stepsize**
InvM	[MeV/c^2]	lowcut and highcut	see text	
E_{BRL}	[MeV]	lowcut	30 - 100	5
E_{FWD}	[MeV]	lowcut	30 - 200	10
E_{BWD}	[MeV]	lowcut	30 - 200	10
clusterE1E9		lowcut	0.2 - 0.5	0.1
GammasDeltaPhi	[rad]	cut on absolute value	0.9, 1.0, 1.2, 1.5	
GammasDelta3D	[rad]	highcut	0.8, 0.9, 1.1, 1.4	
PTD	[ns]	cut on absolute value	20, 50, 100	

TABLE 6.1. The choice of cut variables and corresponding cut values used for the grid scan. Additionally to the given values, always no cut on a variable is considered.

6.1.3 Approach for the eff60 list

Since the π^0 reconstruction efficiency is already below 60 % after applying the preselection, the approach for obtaining a suggestion for a π^0 selection with 60 % efficiency is slightly different from the one introduced in Section 6.1.1. The idea of the grid scan stays the same, but the amount of configurations is much lower, so that no distribution on the *NAF* is necessary. Instead, the jobs are run locally on a single computer. Additionally, the Monte Carlo sample is used without the preselection. Only the basic cuts (hadron skim, CDC acceptance and clusterNHits) are applied.

As variables, only InvM and clusterE are considered. The cut on clusterE is again region-dependent. As InvM lowcut values, only 30 MeV/c^2, 40 MeV/c^2, 50 MeV/c^2, and 60 MeV/c^2 are used, since the 70 MeV/c^2 lowcut already brings the efficiency down to 59.31 %. No InvM highcuts are considered. The clusterE lowcut values are 20 MeV (same as no cut), 22.5 MeV, and 25 MeV.

6.2 Results and optimized π^0 reconstruction list suggestions

6.2.1 Optimized list suggestions without an additional timing cut

In the following, the suggestions for the optimized π^0 reconstruction selections are presented. Three things are considered when filtering the results of the grid scan:

1. The highest purity values to the six given efficiency values are searched.
2. The efficiency of a selection is allowed to vary by ± 0.2 % (absolute percentage points) from the efficiency implied by the name of the selection.
3. The variable cuts defining the selections shall get tighter for lower efficiency selections.

Table 6.2 shows the eff60, eff50, and eff40 selection suggestions. No angle cuts are required for these selections. The comparison to the current generic lists in basf2 is shown in Figure 6.1. There is no noticeable purity gain for these selections, but the suggestions provide the efficiencies implied by their names.

		eff60	**eff50**	**eff40**
efficiency ϵ	[%]	59.83	49.95	39.95
purity p	[%]	2.21	11.88	20.58
π^0 multiplicity		144.81	22.53	10.59
InvM cut	[MeV/c^2]	> 40	101 - 152	117 - 144
E_{BRL} cut	[MeV]	> 20	> 25	> 30
E_{FWD} cut	[MeV]	> 20	> 40	> 80
E_{BWD} cut	[MeV]	> 25	> 40	> 80
clusterE1E9 cut		/	> 0.3	> 0.3
truth-matched π^0s that pass the selection		158,879	132,643	106,093
reconstructed π^0s that pass the selection		7,189,095	1,116,295	515,472
all generated π^0s		265,550	265,550	265,550

TABLE 6.2. Suggestions for the optimized eff60, eff50, and eff40 selections. Note that the basic cuts (hadron skim, CDC acceptance and clusterNHits > 1.5) are applied for all three suggestions and that |t/dt99| < 1.0 is applied for eff50 and eff40.

Table 6.3 shows the eff30 selection suggestions for the different combinations of angle cuts. The suggestions with one angle cut applied reach a ~ 1 % higher purity than without the application

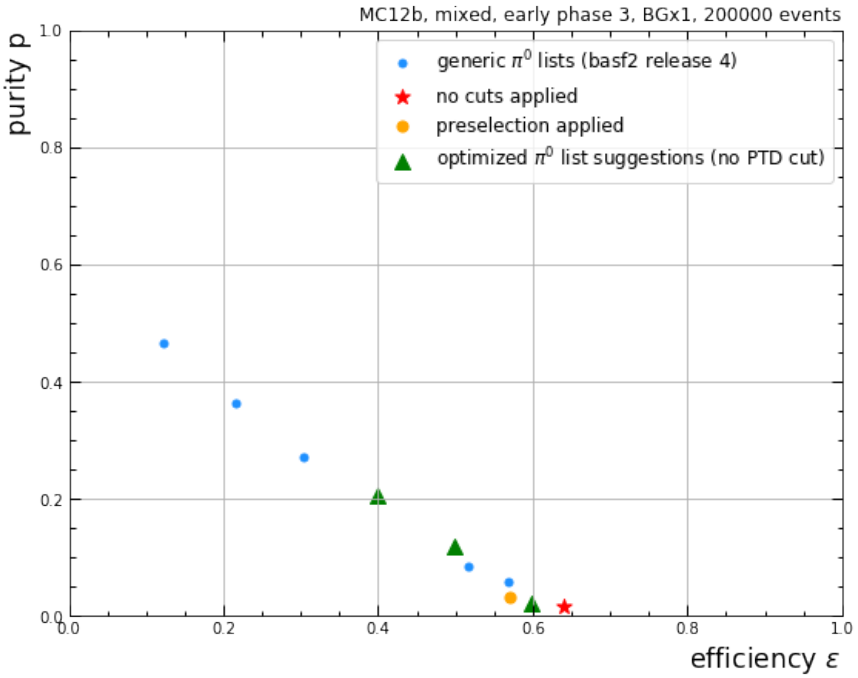

FIGURE 6.1. Working points of the eff60, eff50, and eff40 selection suggestions.

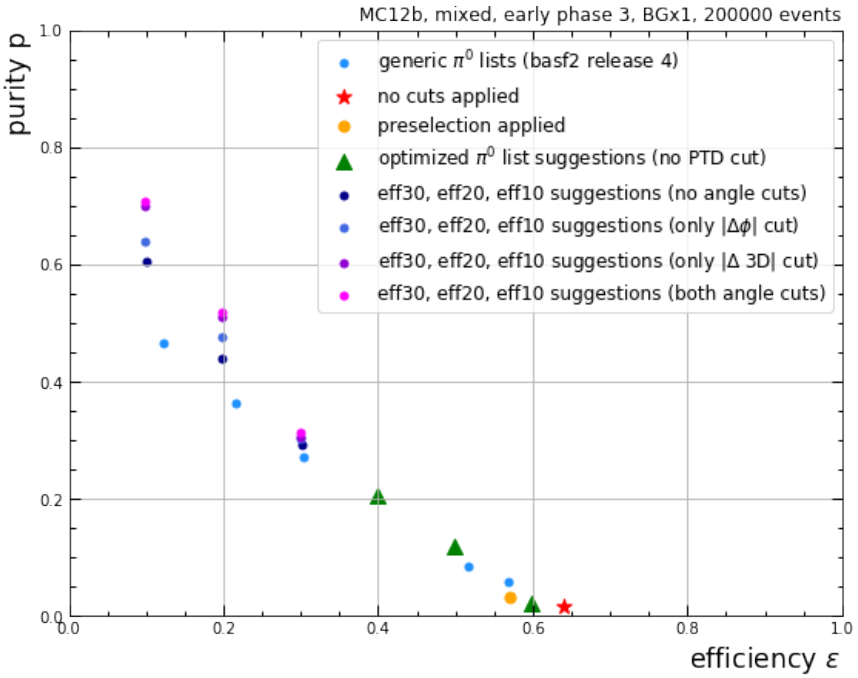

FIGURE 6.2. Visualization of the eff30, eff20, and eff10 suggestions for different angle cut combinations.

		no angle cuts	**cut on $\Delta\phi$**	**cut on Δ3D**	**both angle cuts**
efficiency ϵ	[%]	30.07	29.88	29.92	29.92
purity p	[%]	29.22	30.29	30.57	31.24
InvM cut	[MeV/c^2]	121 - 142	119 - 143	119 - 143	117 - 144
E_{BRL} cut	[MeV]	> 45	> 35	> 30	> 30
E_{FWD} cut	[MeV]	> 180	> 80	> 100	> 80
E_{BWD} cut	[MeV]	> 120	> 80	> 80	> 80
clusterE1E9 cut		> 0.4	> 0.3	> 0.3	> 0.3
$\lvert\Delta\phi\rvert$ cut		/	1.5	/	1.5
Δ3D cut		/	/	< 1.4	< 1.4
truth-matched π^0s that pass the selection		79,844	79,352	79,447	79,446
reconstructed π^0s that pass the selection		273,275	261,938	259,854	254,296
all generated π^0s		265,550	265,550	265,550	265,550

TABLE 6.3. Comparison of the **eff30** suggestions for different angle cut combinations. Note that the preselection is applied for all suggestions.

		no angle cuts	**cut on $\Delta\phi$**	**cut on Δ3D**	**both angle cuts**
efficiency ϵ	[%]	19.86	19.80	19.82	19.83
purity p	[%]	43.97	47.67	51.19	51.94
InvM cut	[MeV/c^2]	121 - 142	123 - 141	123 - 143	121.5 - 144
E_{BRL} cut	[MeV]	> 90	> 55	> 30	> 30
E_{FWD} cut	[MeV]	> 180	> 180	> 120	> 100
E_{BWD} cut	[MeV]	> 120	> 140	> 80	> 80
clusterE1E9 cut		> 0.4	> 0.4	> 0.4	> 0.4
$\lvert\Delta\phi\rvert$ cut		/	1.0	/	1.0
Δ3D cut		/	/	< 0.9	< 0.9
truth-matched π^0s that pass the selection		119,946	110,307	102,804	101,394
reconstructed π^0s that pass the selection		52,736	52,587	52,627	52,660
all generated π^0s		265,550	265,550	265,550	265,550

TABLE 6.4. Comparison of the **eff20** suggestions for different angle cut combinations. Note that the preselection is applied for all suggestions.

of an angle cut. The cut on GammasDelta3D (Δ3D) performs slightly better than the cut on GammasDeltaPhi ($\Delta\phi$) and the combination of both cuts increases the purity by another ~ 1%. The differences in performance are more striking for the eff20 and eff10 suggestions provided in Tables 6.4 and 6.5. For eff20, the combination of both angle cuts gains ~ 8% compared to no angle cut applied. For eff10, it is even a ~ 10% gain. The cut on GammasDelta3D performs distinctly

better than the cut on GammasDeltaPhi for both lists. The visualization of these results is shown in Figure 6.2.

The final suggestions for the eff30, eff20, and eff10 selections are summed in Table 6.6. Note that these are the same as the suggestions with both angle cuts applied from Tables 6.3, 6.4, and 6.5. The working points for all six π^0 reconstruction selection suggestions are shown in Figure 6.3.

		no angle cuts	**cut on $\Delta\phi$**	**cut on Δ3D**	**both angle cuts**
efficiency ϵ	[%]	10.01	9.80	9.92	9.84
purity p	[%]	60.62	63.88	70.00	70.89
InvM cut	[MeV/c^2]	129 - 139	129 - 139	127 - 139	127 - 139
E_{BRL} cut	[MeV]	> 100	> 95	> 100	> 100
E_{FWD} cut	[MeV]	> 200	> 180	> 200	> 200
E_{BWD} cut	[MeV]	> 200	> 180	> 200	> 160
clusterE1E9 cut		> 0.5	> 0.5	> 0.5	> 0.5
$\lvert\Delta\phi\rvert$ cut		/	1.0	/	1.0
Δ3D cut		/	/	< 0.8	< 0.8
truth-matched π^0s that pass the selection		43,859	40,761	37,642	36,845
reconstructed π^0s that pass the selection		26,589	26,037	26,351	26,119
all generated π^0s		265,550	265,550	265,550	265,550

TABLE 6.5. Comparison of the **eff10** suggestions for different angle cut combinations. Note that the preselection is applied for all suggestions.

		eff30	**eff20**	**eff10**
efficiency ϵ	[%]	29.92	19.83	9.84
purity p	[%]	31.24	51.94	70.89
π^0 multiplicity		5.49	2.60	1.51
InvM cut	[MeV/c^2]	117 - 144	121.5 - 144	127 - 139
E_{BRL} cut	[MeV]	> 30	> 30	> 100
E_{FWD} cut	[MeV]	> 80	> 100	> 200
E_{BWD} cut	[MeV]	> 80	> 80	> 160
clusterE1E9 cut		0.3	> 0.4	> 0.5
$\lvert\Delta\phi\rvert$ cut		1.5	1.0	1.0
Δ3D cut		< 1.4	< 0.9	< 0.8
truth-matched π^0s that pass the selection		254,296	101,394	36,845
reconstructed π^0s that pass the selection		79,446	52,660	26,119
all generated π^0s		265,550	265,550	265,550

TABLE 6.6. Suggestions for the optimized eff30, eff20, and eff10 selections. Note that the preselection is applied for all three suggestions.

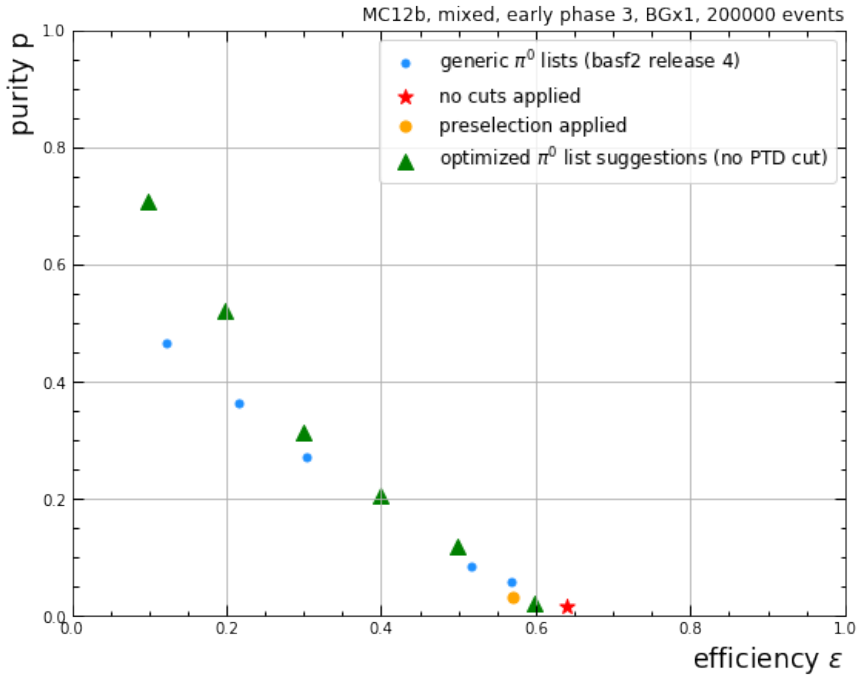

FIGURE 6.3. Visualization of the six π^0 reconstruction selection suggestions for 60%, 50%, 40%, 30%, 20%, and 10%.

6.2.2 Additional timing cut as a performance upgrade

The following suggestions additionally contain a timing cut on the PTD variable. Although the timing calibration of the ECL is not exact enough to allow for tight timing cuts at the time of writing this thesis, the performance of a PTD cut is investigated as a possible future upgrade to the π^0 reconstruction selections. The timing cut on t/dt99 stays the same as applied in the preselection, it is not further investigated in the scope of this thesis.

Table 6.7 shows the eff60, eff50, and eff40 suggestions with an additional PTD cut. The performance of the three suggestions is slightly better than the performance of the suggestions without the additional timing cut. The PTD cut gains $\sim 0.3\%$ in purity for the three selections.
The suggestions for eff30, eff20, and eff10 are shown in Table 6.8. The purity gain with the PTD cut is even higher for these three selections. While the PTD cut gains $\sim 0.5\%$ in purity for eff30, it gains $\sim 0.7\%$ and $\sim 0.6\%$ for eff20 and eff10, respectively.

Figure 6.4 shows the working points to the six suggestions with a PTD cut compared to the ones without a cut on PTD.

		eff60	**eff50**	**eff40**
efficiency ϵ	[%]	59.82	49.83	40.03
purity p	[%]	2.49	12.20	20.91
InvM cut	[MeV/c^2]	> 30	99 - 153	117 - 144
E_{BRL} cut	[MeV]	> 20	> 25	> 30
E_{FWD} cut	[MeV]	> 22.5	> 40	> 80
E_{BWD} cut	[MeV]	> 20	> 40	> 60
clusterE1E9 cut		/	/	> 0.3
$\|\Delta\phi\|$ cut		/	/	/
Δ3D cut		/	/	/
|PTD| cut	[ns]	100	50	50
truth-matched π^0s that pass the selection		158,852	132,329	106,311
reconstructed π^0s that pass the selection		6,379,599	1,084,229	508,312
all generated π^0s		265,550	265,550	265,550

TABLE 6.7. Suggestions for the optimized eff60, eff50, and eff40 selections with PTD cut. Note that the basic cuts (hadron skim, CDC acceptance and clusterNHits > 1.5) are applied for all three suggestions and that |t/dt99| < 1.0 is applied for eff50 and eff40.

		eff30	**eff20**	**eff10**
efficiency ϵ	[%]	29.84	19.81	9.82
purity p	[%]	31.77	52.62	71.57
InvM cut	[MeV/c^2]	117 - 144	121.5 - 144	127 - 139
E_{BRL} cut	[MeV]	> 30	> 35	> 100
E_{FWD} cut	[MeV]	> 100	> 120	> 180
E_{BWD} cut	[MeV]	> 60	> 60	> 100
clusterE1E9 cut		> 0.3	> 0.4	> 0.5
$\|\Delta\phi\|$ cut		1.5	1.2	0.9
Δ3D cut		< 1.4	< 0.9	< 0.8
|PTD| cut	[ns]	50	20	20
truth-matched π^0s that pass the selection		79,239	52,608	26,071
reconstructed π^0s that pass the selection		249,399	99,972	36,426
all generated π^0s		265,550	265,550	265,550

TABLE 6.8. Suggestions for the optimized eff30, eff20, and eff10 selections with PTD cut. Note that the preselection is applied for all three suggestions.

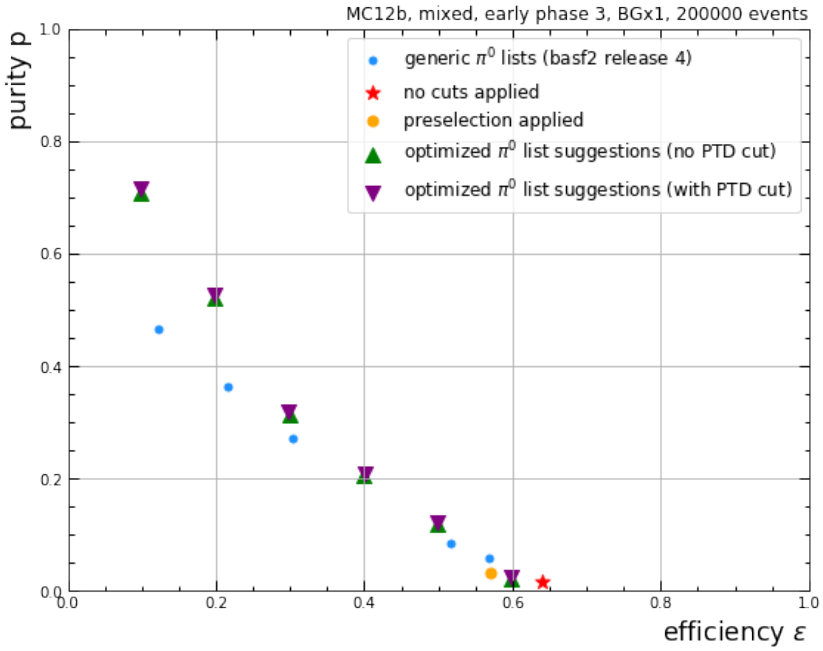

FIGURE 6.4. Visualization of the six π^0 reconstruction selectionsuggestions with PTD cut for 60%, 50%, 40%, 30%, 20%, and 10%.

6.3 Performance on other samples

Since the optimization of the π^0 reconstruction selections is performed on a mixed Monte Carlo sample, the question arises, how the optimized selection suggestions perform on other Monte Carlo samples. The performances on a charged ($\Upsilon(4S) \to B^0\overline{B^0}$), a taupair ($\Upsilon(4S) \to \tau\tau$), a $B \to \pi^0\pi^0$, and a $B \to D^*\tau\nu$ with $D^* \to D^0\pi^0$ sample are checked in the following.

Table 6.9 shows the efficiency, the purity, and the π^0 multiplicity values for the six reconstruction selection suggestions on an official MC12b, charged, early phase 3, BGx1 sample with 200,000 events. The numbers are very similar to the ones for the mixed sample and the generic π^0 reconstruction selections in basf2 are outperformed by the optimized selection suggestions as well. This is expected, since neutral and charged B-mesons decay in very similar manners and produce similarly momentum distributed π^0s, which can be seen in Figures 6.5 and 6.6. Figure 6.7 shows the performance of the six selection suggestions compared to the generic π^0 reconstruction selections implemented in basf2.

The performance on an official MC12b, taupair, early phase 3, BGx1 sample with 200,000 events is shown and visualized in Table 6.10 and Figure 6.8. The generic selections in basf2 and the optimized selection suggestions perform better on the taupair sample than on the mixed and charged samples. This meets the expectation since τ-leptons produce more hard π^0s than

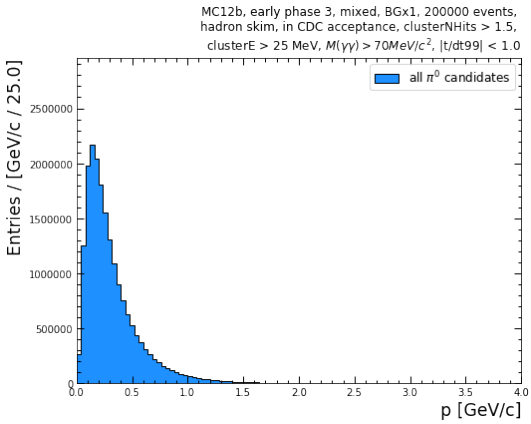

FIGURE 6.5. π^0 momentum distribution for the mixed sample.

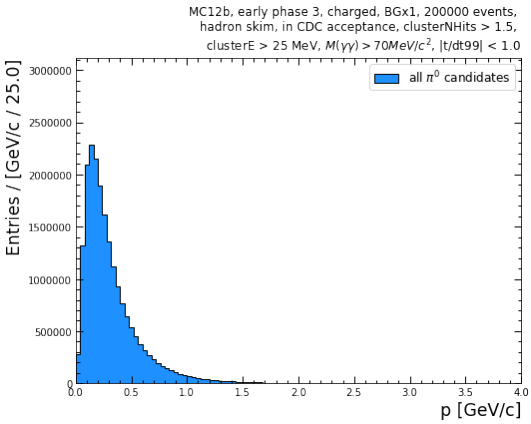

FIGURE 6.6. π^0 momentum distribution for the charged sample.

		preselection	**eff60**	**eff50**	**eff40**	**eff30**	**eff20**	**eff10**
efficiency ϵ	[%]	57.01	60.04	49.96	39.80	29.19	19.44	9.72
purity p	[%]	3.11	2.19	11.74	20.24	30.16	50.73	70.03
π^0 multiplicity		100.82	150.97	23.51	11.02	5.65	2.65	1.53

TABLE 6.9. Performance of the optimized selection suggestions on an official MC12b, charged, early phase 3, BGx1 sample with 200,000 events.

		preselection	**eff60**	**eff50**	**eff40**	**eff30**	**eff20**	**eff10**
efficiency ϵ	[%]	58.43	61.44	52.79	45.74	43.61	37.02	20.39
purity p	[%]	6.35	3.18	28.20	48.54	62.98	75.71	87.71
π^0 multiplicity		12.46	23.39	3.23	2.02	1.70	1.45	1.19

TABLE 6.10. Performance of the optimized selection suggestions on an official MC12b, taupair, early phase 3, BGx1, sample with 200,000 events.

B-mesons do, which can be seen in Figure 6.9. Hard π^0s are higher energetic and therefore less effected by the applied cuts in the selections. Additionally, the taupair sample has to treat with less π^0 candidates, since the π^0 multiplicity is lower. The optimized selection suggestions outperform the generic selections in basf2 for the taupair sample as well.

Table 6.11 and Figure 6.11 describe the performance of the optimized selection suggestions on a $B \to \pi^0\pi^0$ sample. It is an unofficial MC12, phase 3, BGx1 sample with 5,000 events. The π^0s in this sample are very high-energetic, which can be seen in Figure 6.10. The optimized selection suggestions also outperform the generic selections in basf2 for this sample. The efficiencies of the selections are lower for this sample than for the previous samples, which is due to the definition of the applied hadron skim. The hadron skim cuts every event with less than 3 charged tracks. Since the π^0s in this sample are directly produced by a B-meson, it depends on the decay of the

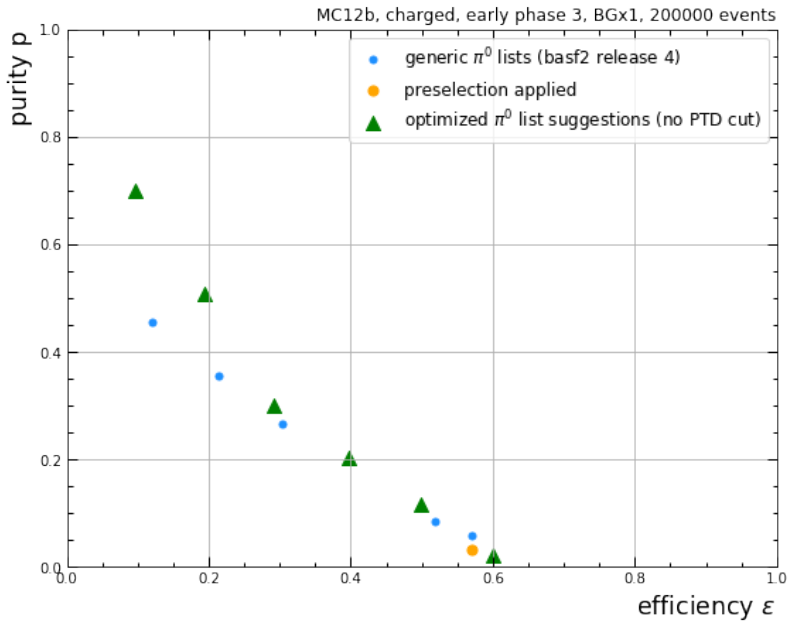

FIGURE 6.7. Performance of the optimized list suggestions on an official MC12b, charged, early phase 3, BGx1 sample with 200,000 events. The suggestions are shown in green, the generic lists from basf2 in blue. The yellow point marks the preselection.

second B-meson in the event, how many charged tracks are in the event. In many cases, the event does not pass the hadron skim.

		preselection	**eff60**	**eff50**	**eff40**	**eff30**	**eff20**	**eff10**
efficiency ϵ	[%]	31.36	33.75	28.81	24.96	24.96	22.89	12.68
purity p	[%]	0.68	0.15	3.77	12.56	26.85	46.19	66.21
π^0 multiplicity		857.95	4,104.53	142.56	37.10	17.35	9.26	3.67

TABLE 6.11. Performance of the optimized selection suggestions on an unofficial MC12, $B \to \pi^0\pi^0$, phase3, BGx1 sample with 5,000 events.

		preselection	**eff60**	**eff50**	**eff40**	**eff30**	**eff20**	**eff10**
efficiency ϵ	[%]	10.99	11.52	8.34	5.02	0.03	0.00	0.00
purity p	[%]	0.24	0.06	0.81	1.79	0.03	0.00	0.00
π^0 multiplicity		1,222.76	5,565.99	277.83	76.06	26.57	8.82	3.09

TABLE 6.12. Performance of the optimized selection suggestions on an unofficial MC12, $B \to D^*\tau\nu$ with $D^* \to D^0\pi^0$, phase 3, BGx1 sample with 5,000 events.

Finally, the performance on an unofficial MC12, $B \to D^*\tau\nu$ with $D^* \to D^0\pi^0$, phase 3, BGx1 sample with 5,000 events is tested. The corresponding numbers can be found in Table 6.12. The

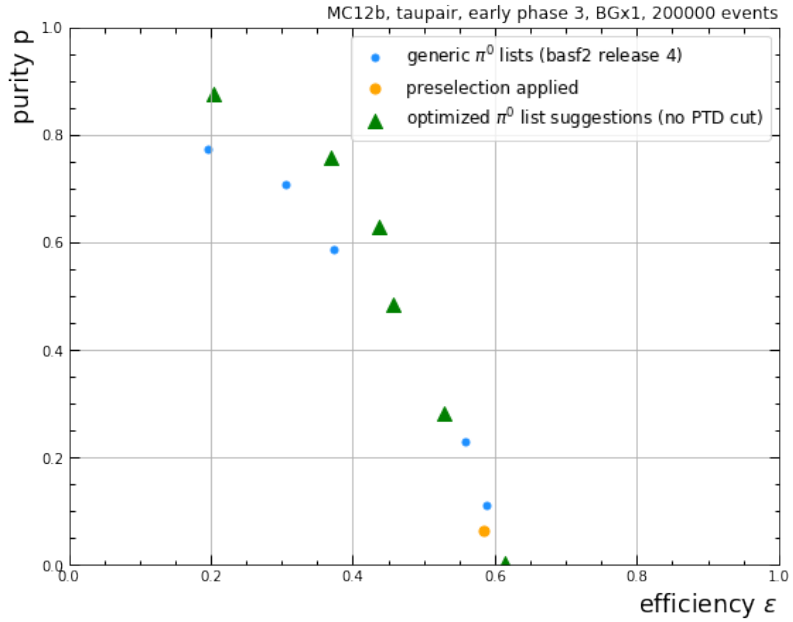

FIGURE 6.8. Performance of the optimized list suggestions on an official MC12b, taupair, early phase 3, BGx1 sample with 200,000 events. The optimized list suggestions are shown in green, the generic lists from basf2 in blue. The yellow point marks the preselection.

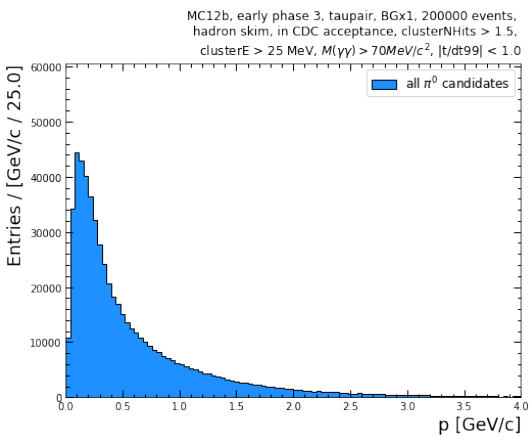

FIGURE 6.9. π^0 momentum distribution for the taupair sample.

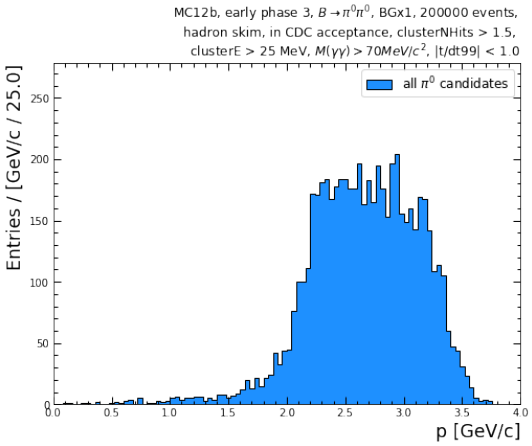

FIGURE 6.10. π^0s momentum distribution for the $B \to \pi^0\pi^0$ sample.

π^0s in this sample are very low-energetic, since the mass difference between a D^* and a D^0 is $\sim 142\,\mathrm{MeV/c^2}$ [32], which is only $\sim 7\,\mathrm{MeV/c^2}$ more than the rest mass of a π^0. The π^0 momentum distribution of this sample is shown in Figure 6.12. Due to this fact, the performance of the optimized suggestions and the generic selections in basf2 is very bad on this sample. The applied

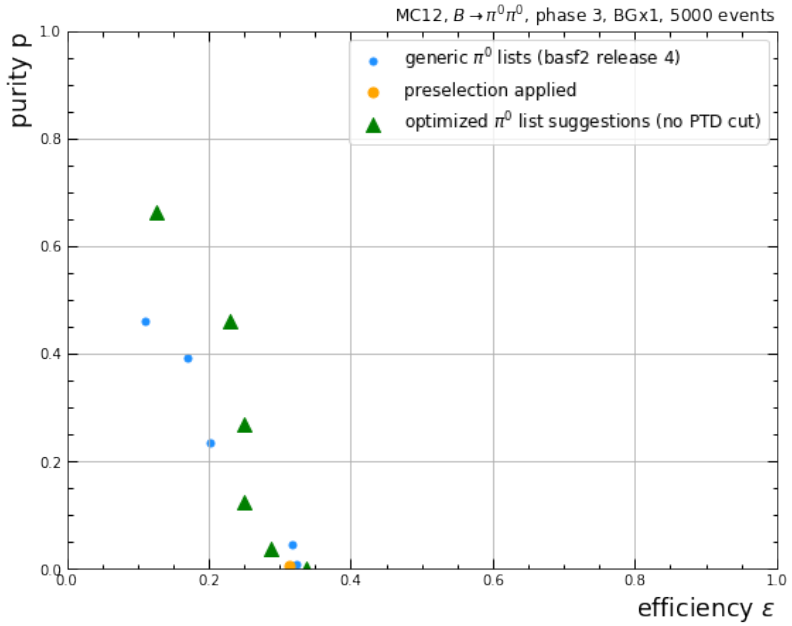

FIGURE 6.11. Performance of the optimized selection suggestions on an unofficial MC12, $B \to \pi^0\pi^0$, phase 3, BGx1 sample with 5,000 events. The suggestions are shown in green, the generic selections from basf2 in blue. The yellow point marks the preselection.

cuts are too tight for the π^0s in this sample. For the eff20 and eff10 suggestions, even no π^0s are left. The visualization of the performance on the $B \to D^*\tau\nu$ with $D^* \to D^0\pi^0$ sample is shown in Figure 6.13. Figure 6.14 provides a zoomed version.

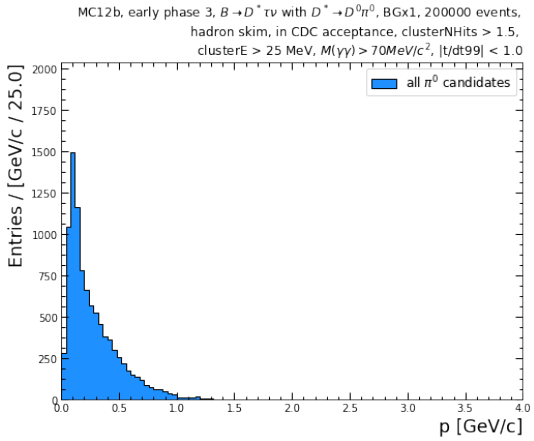

FIGURE 6.12. π^0 momentum distribution for the $B \to D^*\tau\nu$ with $D^* \to D^0\pi^0$ sample.

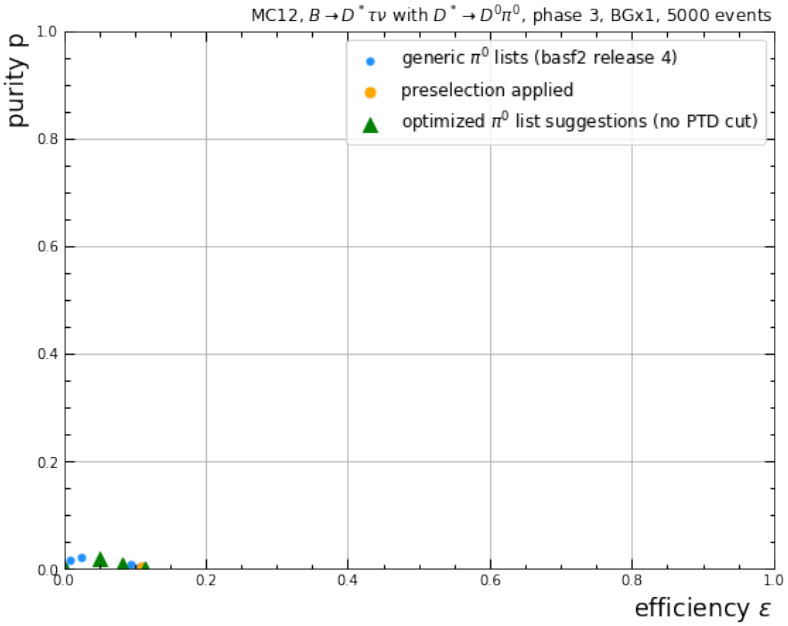

FIGURE 6.13. Performance of the optimized selection suggestions on an unofficial MC12, $B \to D^* \tau\nu$ with $D^* \to D^0\pi^0$, phase 3, BGx1 sample with 5,000 events. The suggestions are shown in green, the generic selections from basf2 in blue. The yellow point marks the preselection.

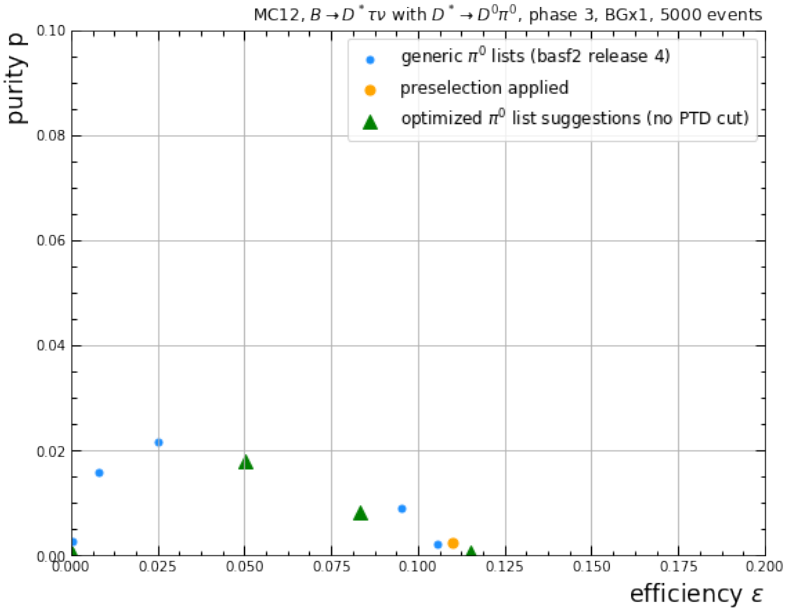

FIGURE 6.14. Performance of the optimized selection suggestions on the $B \to D^* \tau\nu$ with $D^* \to D^0\pi^0$ sample (zoomed version).

CHAPTER 7

PERFORMANCE ON DATA

After obtaining optimized π^0 reconstruction selections in Chapter 6 and testing these selections on other Monte Carlo samples than the mixed sample, the present Chapter checks the performance of the optimized selections on data and compares it to Monte Carlo. To that end, experiment 8, bucket 7, $\Upsilon(4S)$ data from early phase 3 is compared to MC12b, early phase 3, BGx1 Monte Carlo.

7.1 Comparison approach

In order to compare data and Monte Carlo, all the different decay channels making up data in real life have to be summed for Monte Carlo. These samples are the mixed sample ($\Upsilon(4S) \to B^+B^-$), the charged sample ($\Upsilon(4S) \to B^0\overline{B^0}$), the taupair sample ($\Upsilon(4S) \to \tau\tau$), and the continuous background consisting of the quark pair samples uubar ($\Upsilon(4S) \to u\overline{u}$), ddbar ($\Upsilon(4S) \to d\overline{d}$), ssbar ($\Upsilon(4S) \to s\overline{s}$), and ccbar ($\Upsilon(4S) \to c\overline{c}$). For all of these samples, one Monte Carlo file with $\sim 200,000$ events is used, respectively.

Before summing the samples, they have to be normalized to data. Otherwise, Monte Carlo and data are not comparable. To do so, there are many different possibilities. For this thesis, Monte Carlo is normalized to the integrated luminosity of the data. Therefore, for each Monte Carlo file the integrated luminosity $L_{int,MC}$ is calculated via

$$L_{int,MC} = \frac{N_{\text{events}}}{\sigma_{MC}} \quad , \tag{7.1}$$

where N_{events} is the number of events in the Monte Carlo sample and σ_{MC} is the cross section of the decay to the Monte Carlo file. The cross sections to the Monte Carlo files can be found in Table 7.1. The number of events per Monte Carlo file is extracted from the respective file and

decay	**cross section [nb]**
$\Upsilon(4S) \to B^+B^-$	0.5103
$\Upsilon(4S) \to B^0\overline{B^0}$	0.5397
$\Upsilon(4S) \to \tau\tau$	0.9190
$\Upsilon(4S) \to u\overline{u}$	1.5997
$\Upsilon(4S) \to d\overline{d}$	0.4023
$\Upsilon(4S) \to s\overline{s}$	0.3825
$\Upsilon(4S) \to c\overline{c}$	1.3265

TABLE 7.1. Cross sections for the different Monte Carlo files. The numbers are taken from the *Belle II* software code. Rounded numbers can be found in [36].

amounts to ~ 200,000 per file.
The integrated luminosity $L_{int,data}$ of the data is taken from a so-called luminosity file. For each data production, the integrated luminosity per run is stored in an own luminosity file. Runs 1917 – 3123 of experiment 8, bucket 7 are used, which add up to $\sim 2.98\,\text{fb}^{-1}$ of integrated luminosity. When summing the Monte Carlo files, each file is weighted by the factor $\frac{L_{int,data}}{L_{int,MC}}$ and therefore normalized to data.

7.2 Data and MC comparison

The results of the data Monte Carlo comparison study are presented in the following. The variable distributions of the variables used for the grid scan are shown for the eff30 suggestion. The distributions of the remaining variables described in Chapters 3 and 4 for the eff30 suggestion can be found in Section A.2 of the appendix. The results for the other selection suggestions are located in the appendix as well.

Figure 7.1 shows the InvM distributions for data and Monte Carlo in the range applied for the eff30 suggestion. The peak position is clearly different for data and Monte Carlo. For Monte Carlo, the peak is at $\sim 132.5\,\text{MeV/c}^2$, while it is at $\sim 131.5\,\text{MeV/c}^2$ for data. One possible explanation is that the low-energy tails of the photons in data are higher than they are simulated in Monte Carlo. Higher low-energy tails of the photons lead to an even more shifted π^0 peak. Another possible reason is, that the energy calibration for data is not exact enough at the time of writing this thesis. The mismatched energy of the photons would shift the π^0 peak as well.
Figure 7.2 shows a wider range of the InvM distributions. The InvM window applied for the eff30 suggestion is shown with red lines and arrows. This view on the InvM distributions shows that the overall agreement of data and Monte Carlo is quite good, except for the π^0 peak not being matched perfectly. Monte Carlo is slightly exceeding data.

The clusterE distributions for the eff30 suggestion is shown in Figure 7.3. The shapes for data and Monte Carlo agree very well. Again, Monte Carlo is slightly exceeding data, which can be seen in the range from 200 MeV to 300 MeV. The range from 30 MeV to 50 MeV shows an interesting

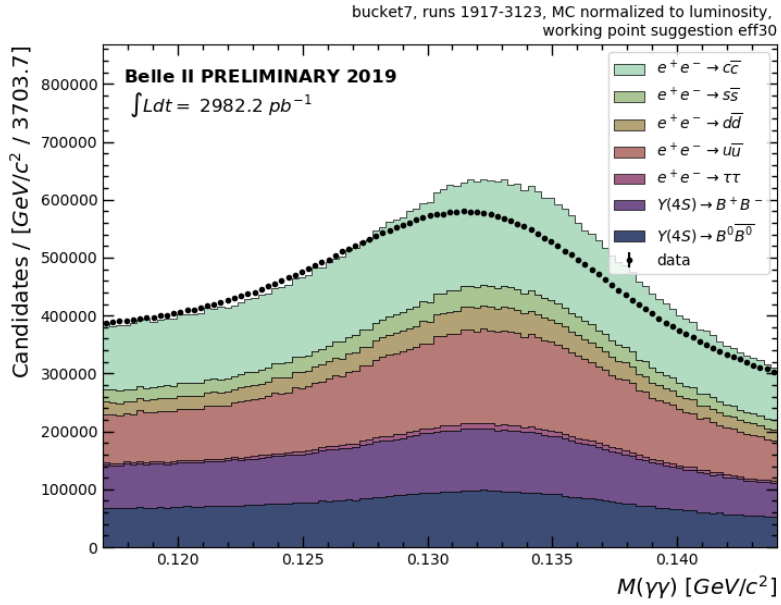

FIGURE 7.1. Comparison of data and Monte Carlo for the InvM distribution for the eff30 suggestion. Monte Carlo is normalized to data luminosity.

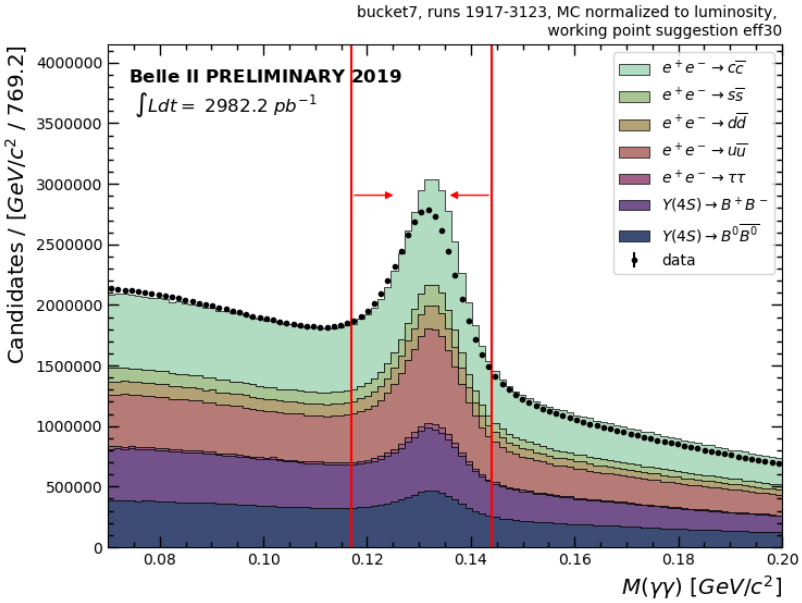

FIGURE 7.2. Comparison of data and Monte Carlo for the InvM distribution for the eff30 suggestion (broader range). The InvM window of the selection is annotated in red. Monte Carlo is normalized to data luminosity.

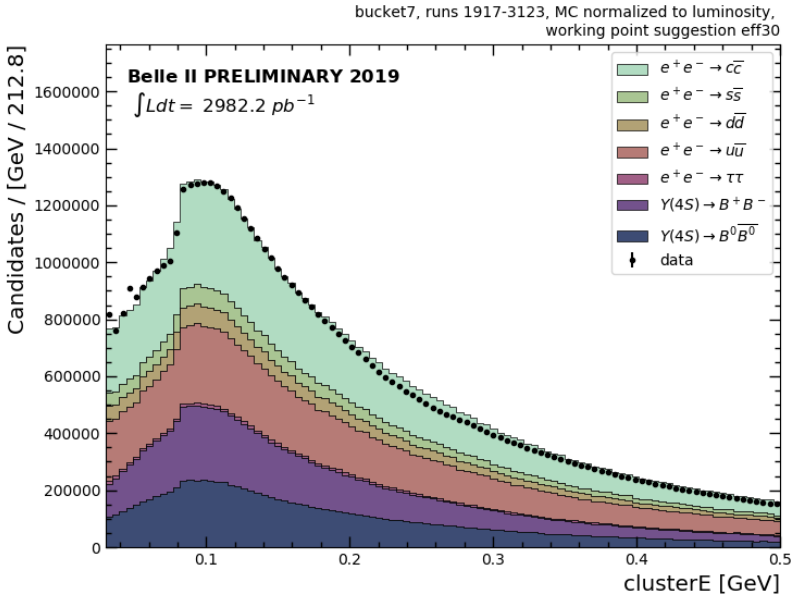

FIGURE 7.3. Comparison of data and Monte Carlo for the clusterE distribution for the eff30 suggestion. Monte Carlo is normalized to data luminosity.

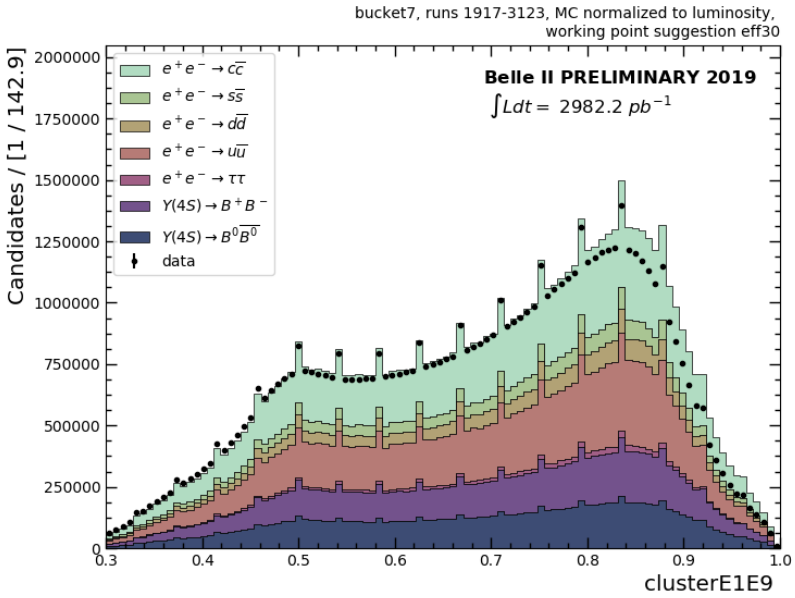

FIGURE 7.4. Comparison of data and Monte Carlo for the clusterE1E9 distribution for the eff30 suggestion. Monte Carlo is normalized to data luminosity.

behaviour. The distribution shows a small peak for clusterE values around ~ 45 MeV and rises for values from ~ 35 MeV down to the 30 MeV border of the distribution. These observations could be explained by background effects, but need further investigation.

Figure 7.4 shows the clusterE1E9 distributions for data and Monte Carlo. The shapes agree very well, but Monte Carlo again slightly exceeds data, which can be seen at the peak between 0.8 and 0.9. The binning effects mentioned in Chapter 3 are clearly visible.

Figures 7.5 and 7.6 show the comparison distributions for GammasDeltaPhi and GammasDelta3D. The mismatch of data and Monte Carlo is the same for these two variables. Data is lower than Monte Carlo, but the shapes agree very well.

The comparison distributions for the two timing variables are shown in Figures 7.7 and 7.8. The distribution for t/dt99 in Figure 7.7 justifies the statement in Chapter 6, that the timing calibration of the ECL is not exact enough to allow tight timing cuts at the time of writing this thesis. The t/dt99 distributions for data and Monte Carlo totally disagree. The shape for data is far broader than for Monte Carlo and the data peak is shifted to $\sim(-0.15)$.
The distributions for PTD show higher agreement. The peak is at 0 for both distributions, but the shapes are different. The Monte Carlo distribution is much narrower than the distribution for data.

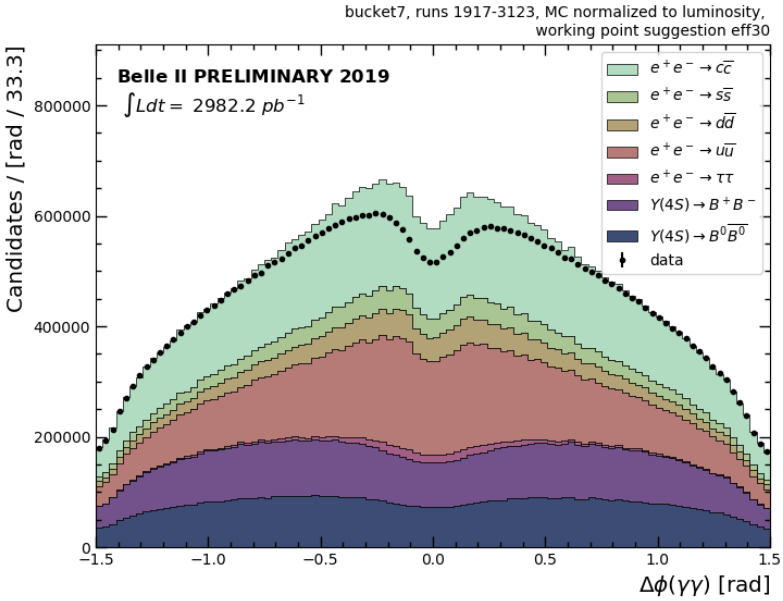

FIGURE 7.5. Comparison of data and Monte Carlo for the GammasDeltaPhi distribution for the eff30 suggestion. Monte Carlo is normalized to data luminosity.

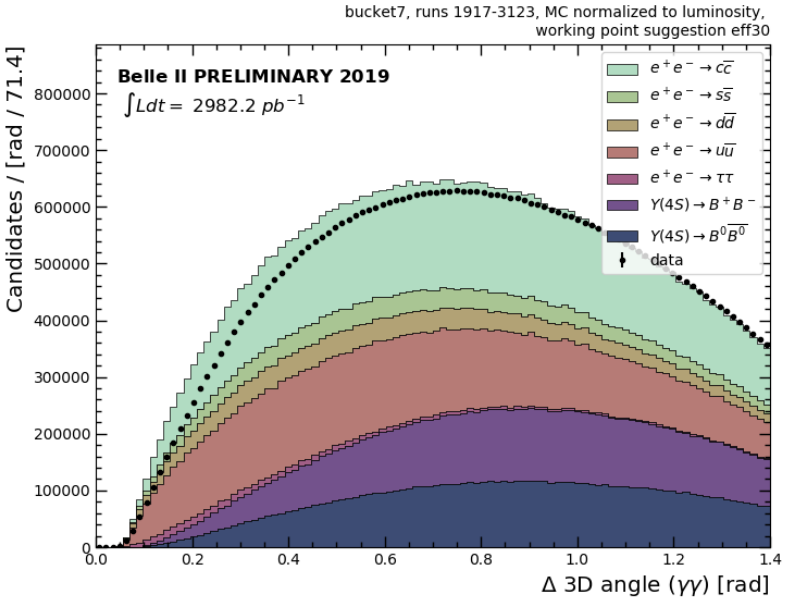

FIGURE 7.6. Comparison of data and Monte Carlo for the GammasDelta3D distribution for the eff30 suggestion. Monte Carlo is normalized to data luminosity.

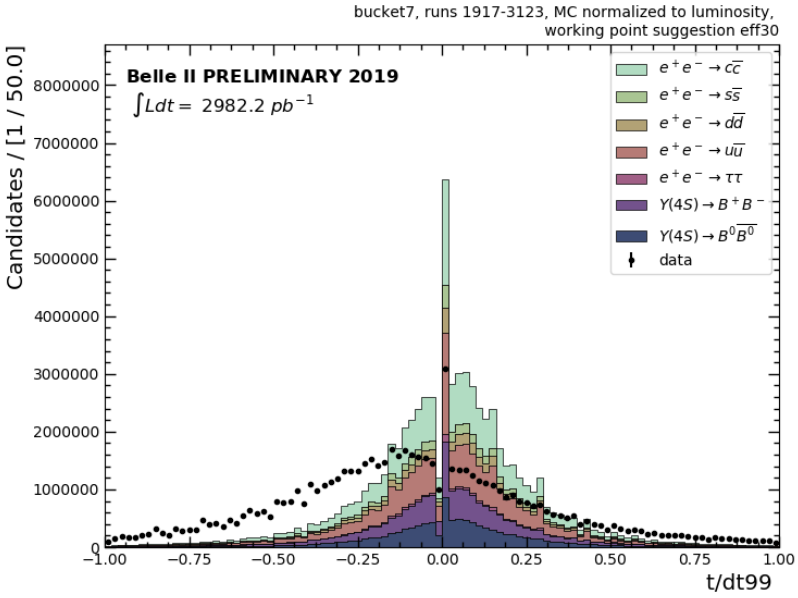

FIGURE 7.7. Comparison of data and Monte Carlo for the t/dt99 distribution for the eff30 suggestion. Monte Carlo is normalized to data luminosity.

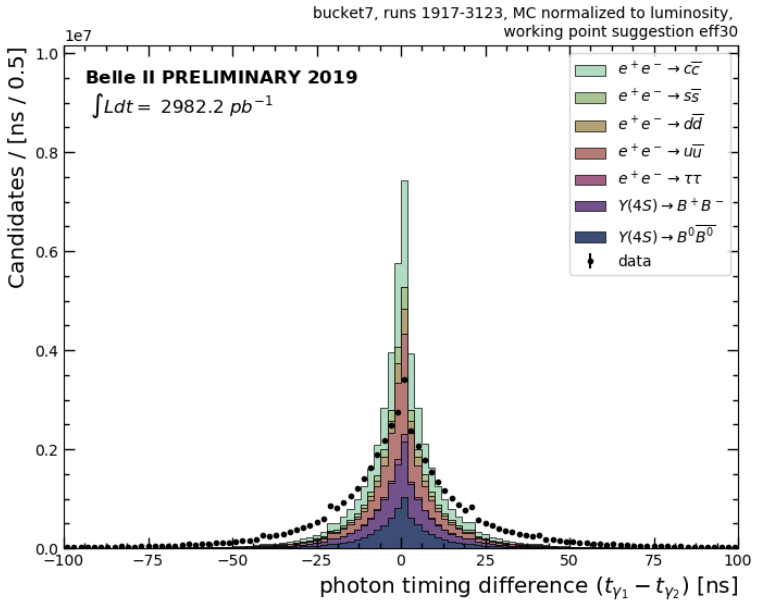

FIGURE 7.8. Comparison of data and Monte Carlo for the PTD distribution for the eff30 suggestion. Monte Carlo is normalized to data luminosity.

CHAPTER 8

SUMMARY & CONCLUSION

In this thesis, optimized π^0 reconstruction selections for the *Belle II analysis software framework* (basf2) were provided. For this purpose, a variable study on several photon and π^0 variables was performed to find the best possible variable choice to be used for a full grid scan on a $\Upsilon(4S) \to B^0\overline{B^0}$ Monte Carlo sample. Optimized selections for 60 %, 50 %, 40 %, 30 %, 20 %, and 10 % of π^0 reconstruction efficiency were provided using the results of the grid scan. The performances of the optimized selections were also tested on $\Upsilon(4S) \to B^+B^-$, $\Upsilon(4S) \to \tau\tau$, $B \to \pi^0\pi^0$, and $B \to D^*\tau\nu$ with $D^* \to D^0\pi^0$ Monte Carlo samples. Finally, the optimized selections were applied to data and compared to Monte Carlo.

The variable study investigated the linear correlation between the variables and provided promising figure of merit based cut regions for each variable. The study distinguished between three variable categories: shower shape variables, angle variables and timing variables. While variables among the same category are strongly linearly correlated, variables among different categories show a weak linear correlation. Thus, the best performance is achieved by combining variables from different categories.

The full grid scan on the $\Upsilon(4S) \to B^0\overline{B^0}$ Monte Carlo sample provided six optimized π^0 reconstruction selections named eff60, eff50, eff40, eff30, eff20, and eff10. The selections provide the π^0 reconstruction efficiencies implied by their names, which is not the case for all of the generic π^0 reconstruction selections implemented in basf2 at the time of writing this thesis. The performance of the six optimized selections outperforms the performance of the generic selections implemented in basf2 on the $\Upsilon(4S) \to B^0\overline{B^0}$ Monte Carlo sample.
The same holds for the $\Upsilon(4S) \to B^+B^-$ and the $\Upsilon(4S) \to \tau\tau$ Monte Carlo samples. For the $\Upsilon(4S) \to B^+B^-$ Monte Carlo sample, the performance of the optimized selections is almost identical to the performance on the $\Upsilon(4S) \to B^0\overline{B^0}$ Monte Carlo sample. For the $\Upsilon(4S) \to \tau\tau$

Monte Carlo sample, the optimized selections do not provide the π^0 reconstruction efficiencies implied by their names due to the higher portion of high-energetic π^0s in this sample.
The optimized π^0 reconstruction selections are also suitable to be used on a $B \to \pi^0\pi^0$ sample, but cautiously when using the applied hadron skim. For the $B \to \pi^0\pi^0$ Monte Carlo sample used in this thesis, the hadron skim distinctly lowered the efficiencies of the selections, since it cuts all events with less than three tracks.
The optimized selections are not designed to be used on a $B \to D^*\tau\nu$ with $D^* \to D^0\pi^0$ sample. The π^0s in the used Monte Carlo sample were too low-energetic for the selection cuts, which resulted in a very bad performance. The eff20 and eff10 selections even left not one single π^0. Therefore, a specific optimization has to be done for this decay. A first suggestion would be to loosen or even leave out the energy cuts and work with the residual variables used for the grid scan in this thesis.

The comparison of bucket7 data and MC12b Monte Carlo showed a high agreement for the shapes of the variable distributions, but a slight overestimation of Monte Carlo. A further study should investigate if this is true for all run ranges of bucket7 or if this is run dependent.
The reconstructed mass of the π^0 peaks at $\sim 131.5\,\mathrm{MeV/c^2}$, which is $\sim 1\,\mathrm{MeV/c^2}$ lower than the value expected from Monte Carlo. Possible explanations are the slight mismodeling of the low-energy tails of the photons in Monte Carlo or the miscalibration of the photon energy for data. Unfortunately, it was not possible to quantify this observation in a more detailed way for this thesis due to lack of time. A further study should quantify the parameters of the π^0 peak and whether the parameters vary for different run ranges of bucket7.

The high agreement of the distribution shapes for data and Monte Carlo is not true for the timing variables investigated in this thesis. The distribution shapes for the t/dt99 variable show high disagreement. For data, the t/dt99 distribution peaks at $\sim(-0.15)$, while it is expected from Monte Carlo to peak at 0. This shows, that at the time of writing this thesis, the timing calibration for data is not as exact as it should be. Besides, the t/dt99 distribution for data is broader and flatter than for Monte Carlo. This also holds for the PTD variable.
Regarding the variable study and the grid scan, the timing variables are promising to be used in the future. At the time of writing this thesis, they have to be treated with caution.

APPENDIX

The appendix contains all the remaining plots not treated in the certain chapters due to clarity and readability reasons.

A.1 Additional plots for Section 5.3.3

In the following, the signal and background distributions as well as the figure of merits for the remaining variables not treated in Section 5.3.3 are listed. The plots for PTD, $\text{PTD}_{extended}$, GammasDeltaPhi, GammasDelta3D, clusterE1E9, clusterE9E21, clusterLAT, clusterAbsZernikeMoment40, clusterAbsZernikeMoment51, clusterZernikeMVA, InvM, E_{BRL}, E_{FWD}, and E_{BWD} are shown.

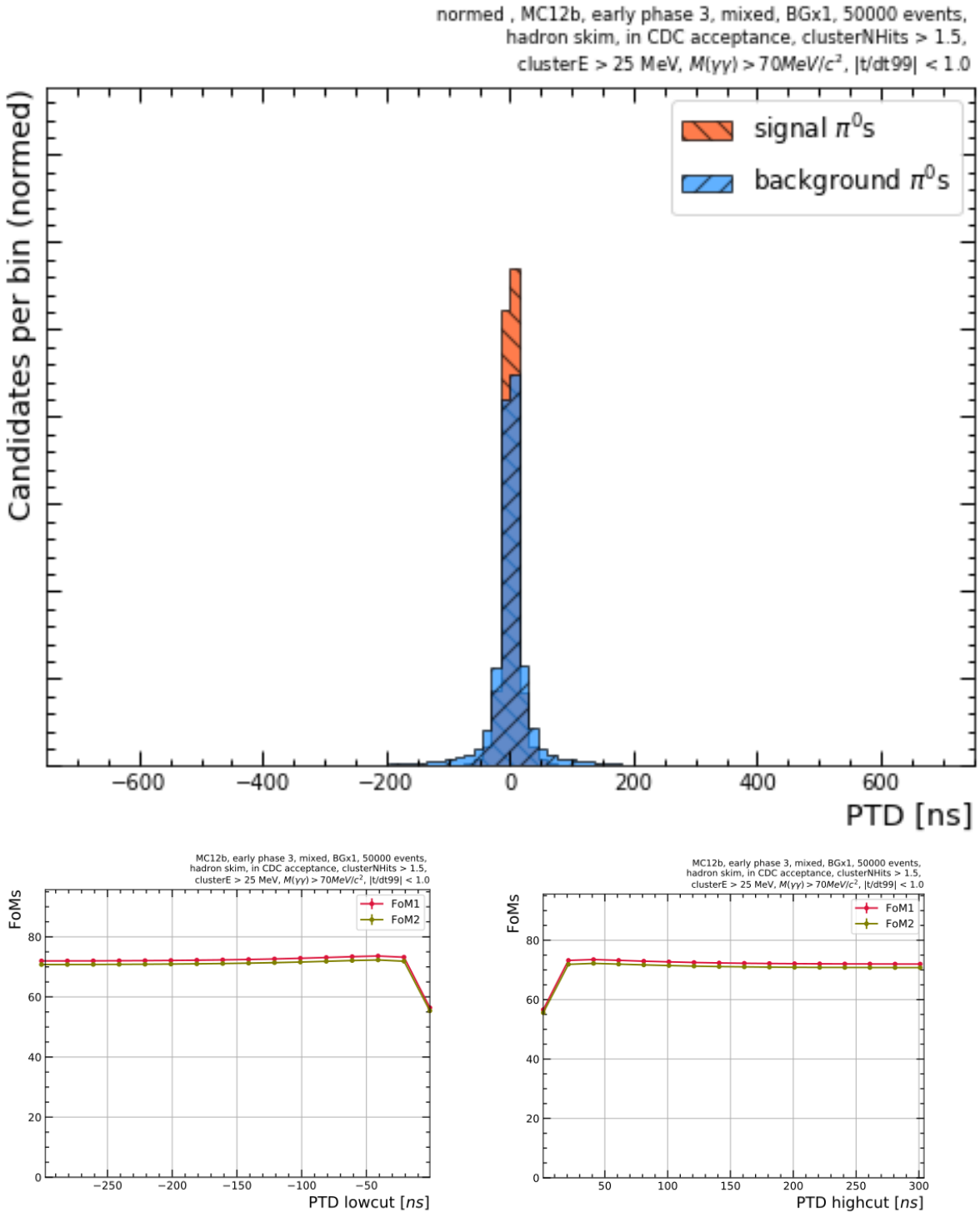

FIGURE A.1. Signal and background distributions for PTD (top). Figure of merits for PTD lowcuts (bottom left) and highcuts (bottom right).

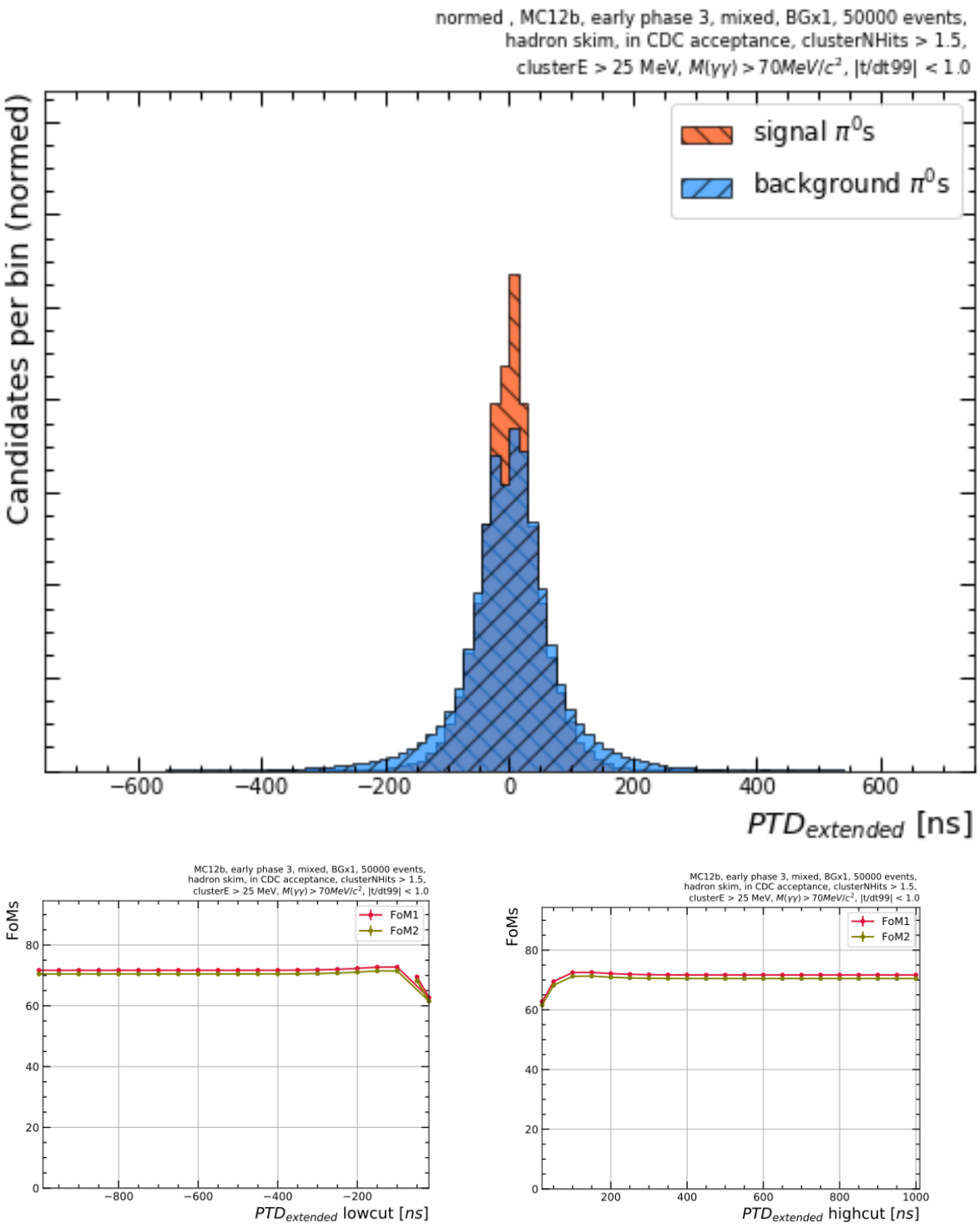

FIGURE A.2. Signal and background distributions for $\text{PTD}_{extended}$ (top). Figure of merits for $\text{PTD}_{extended}$ lowcuts (bottom left) and highcuts (bottom right).

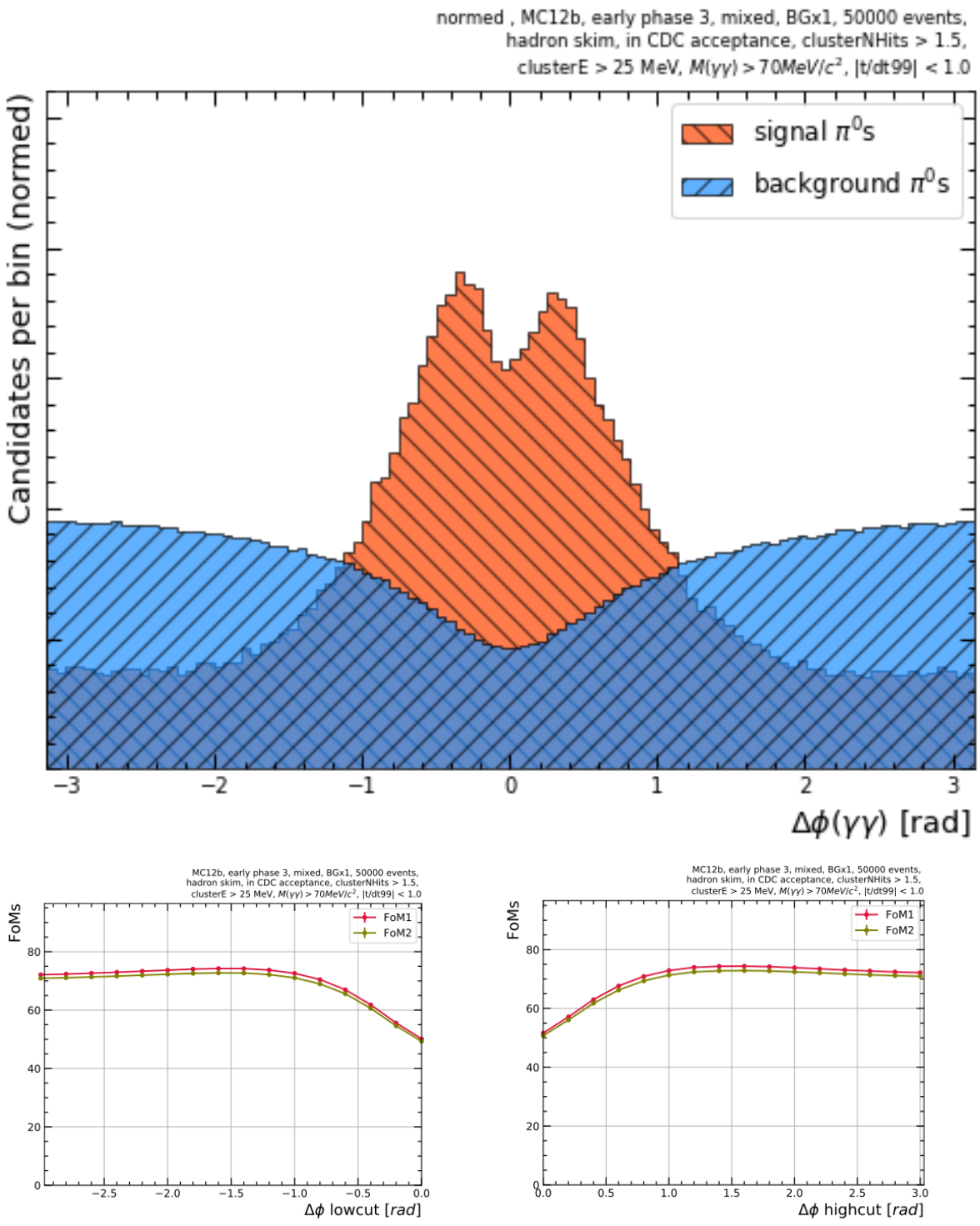

FIGURE A.3. Signal and background distributions for clusterDeltaPhi (top). Figure of merits for clusterDeltaPhi lowcuts (bottom left) and highcuts (bottom right).

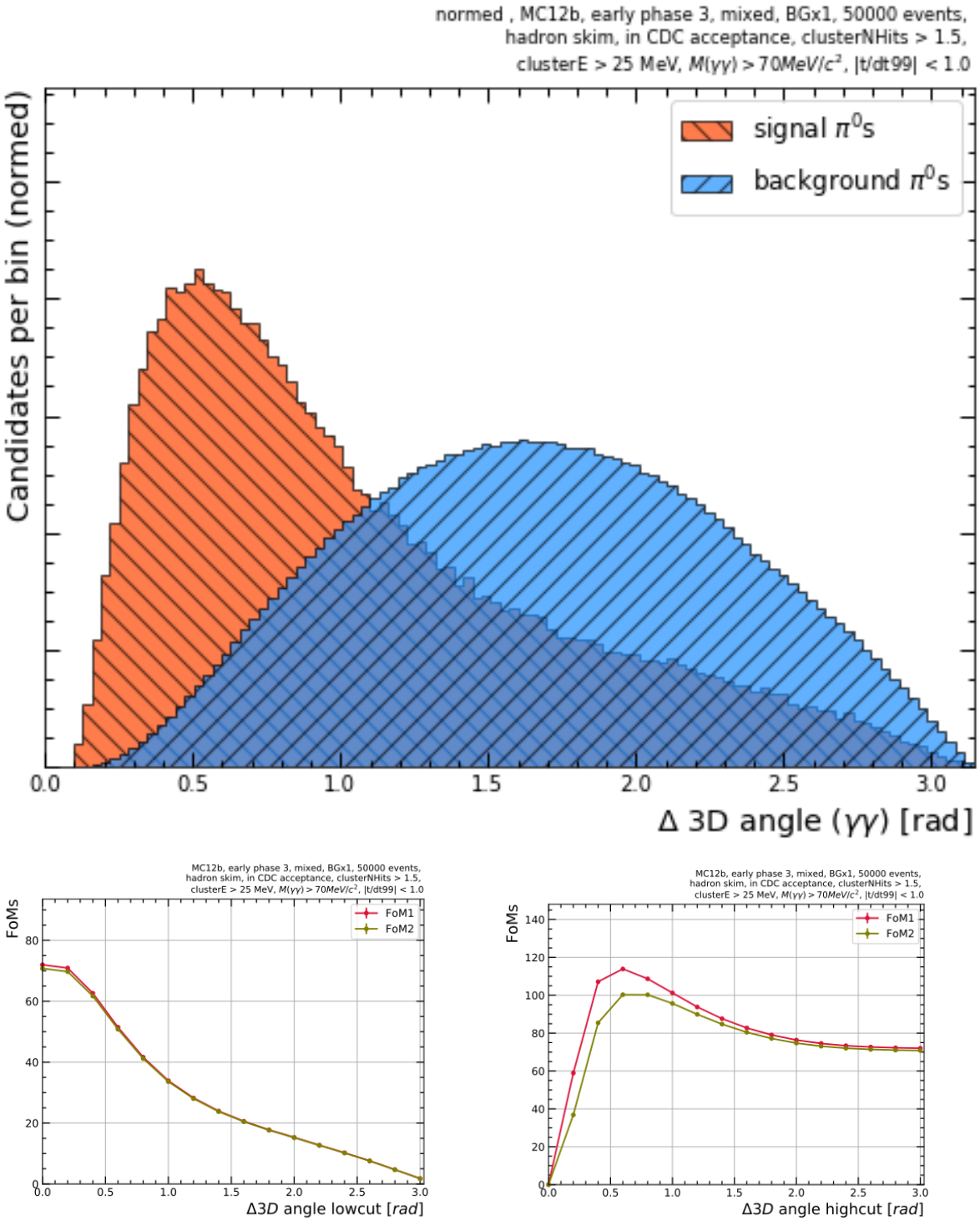

FIGURE A.4. Signal and background distributions for clusterDelta3D (top). Figure of merits for clusterDelta3D lowcuts (bottom left) and highcuts (bottom right).

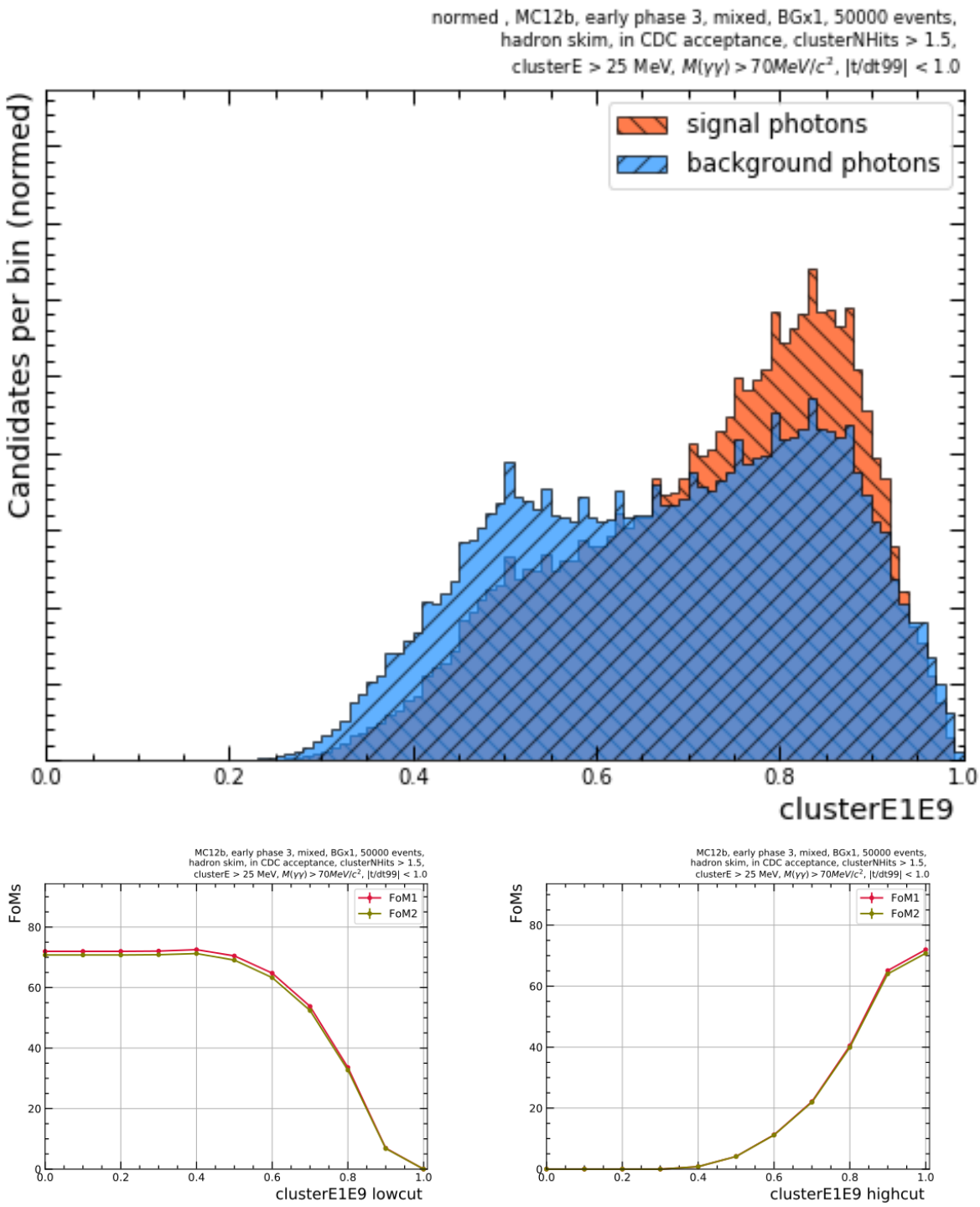

FIGURE A.5. Signal and background distributions for clusterE1E9 (top). Figure of merits for clusterE1E9 lowcuts (bottom left) and highcuts (bottom right).

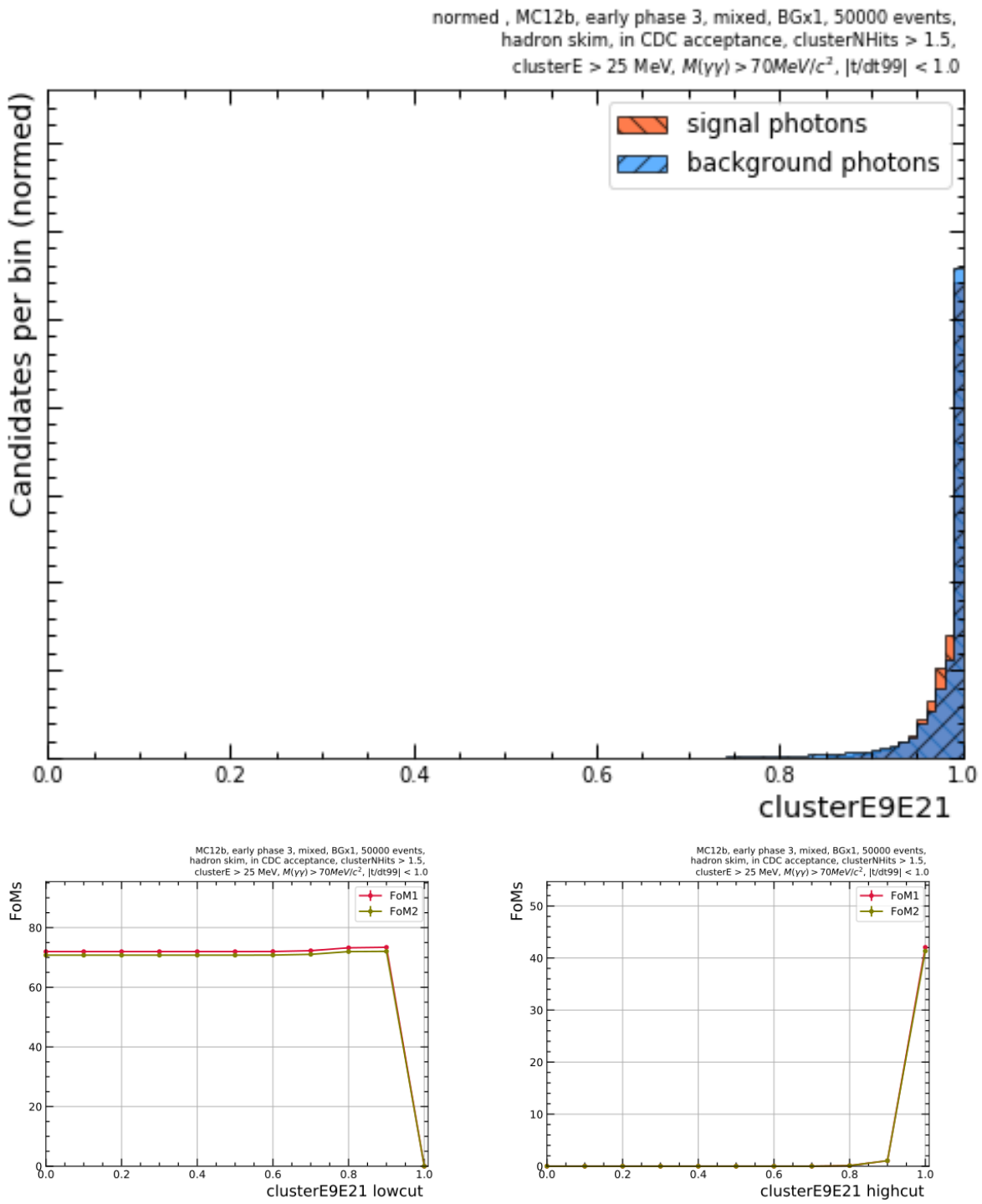

FIGURE A.6. Signal and background distributions for clusterE9E21 (top). Figure of merits for clusterE9E21 lowcuts (bottom left) and highcuts (bottom right).

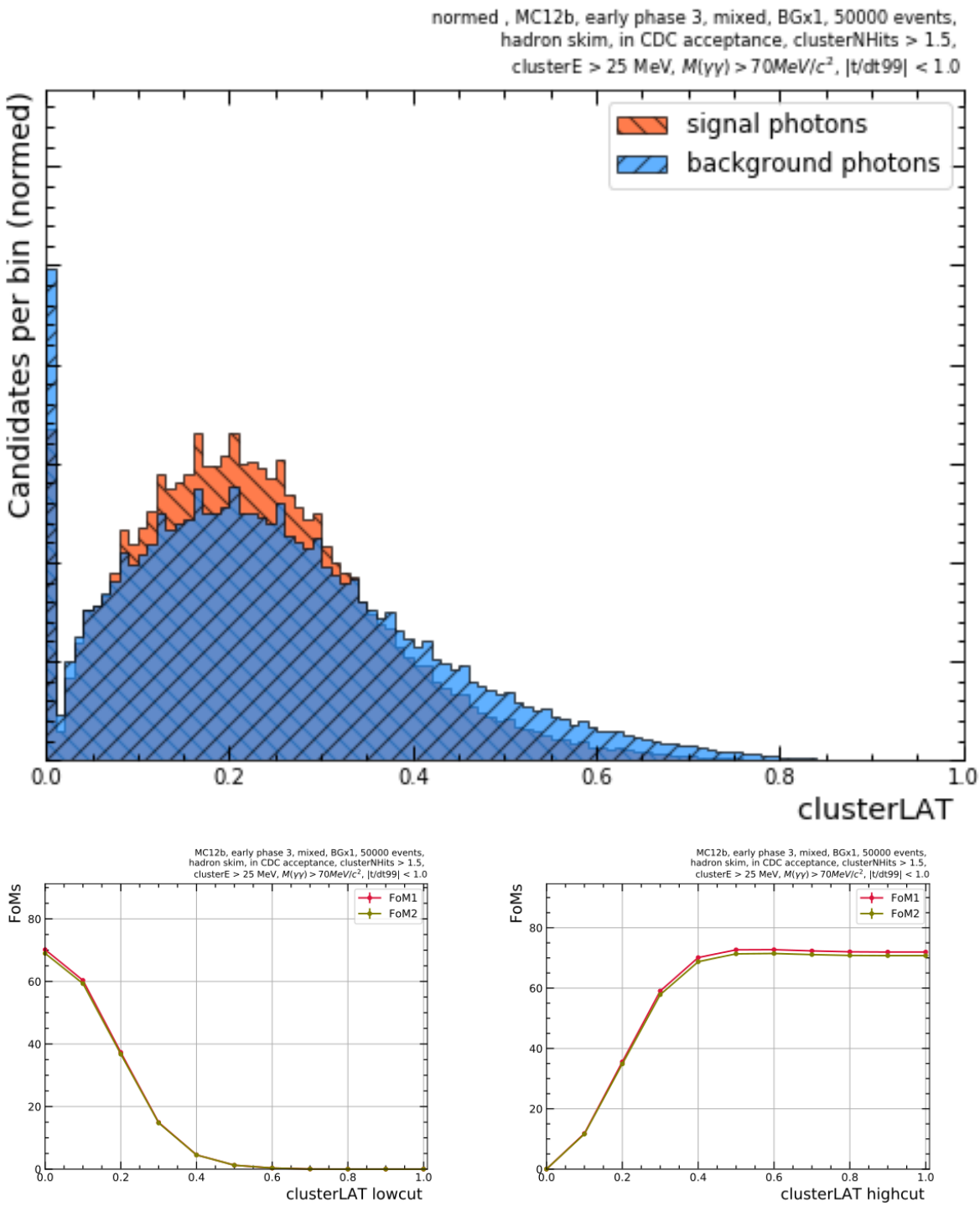

FIGURE A.7. Signal and background distributions for clusterLAT (top). Figure of merits for clusterLAT lowcuts (bottom left) and highcuts (bottom right).

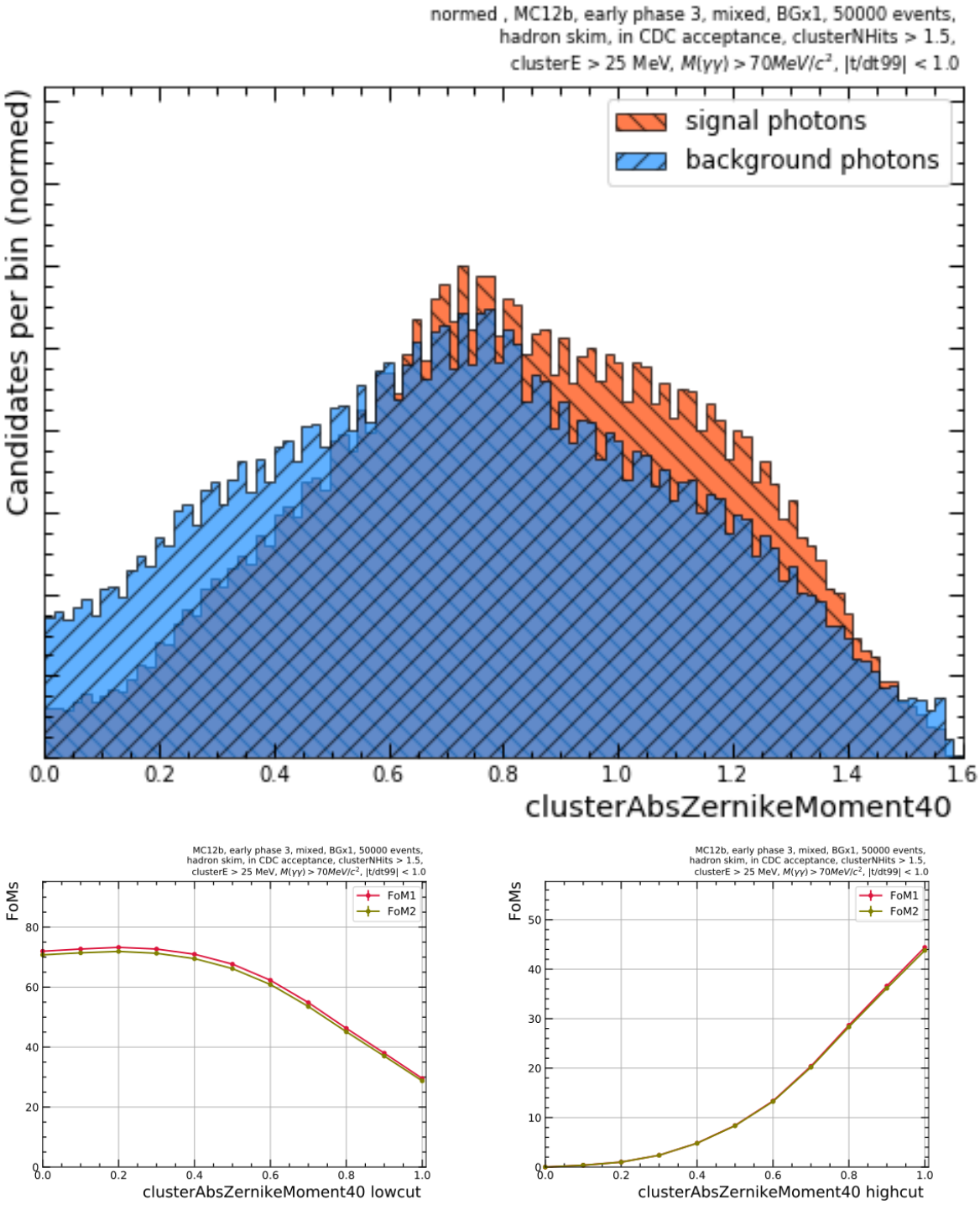

FIGURE A.8. Signal and background distributions for clusterAbsZernikeMoment40 (top). Figure of merits for clusterAbsZernikeMoment40 lowcuts (bottom left) and highcuts (bottom right).

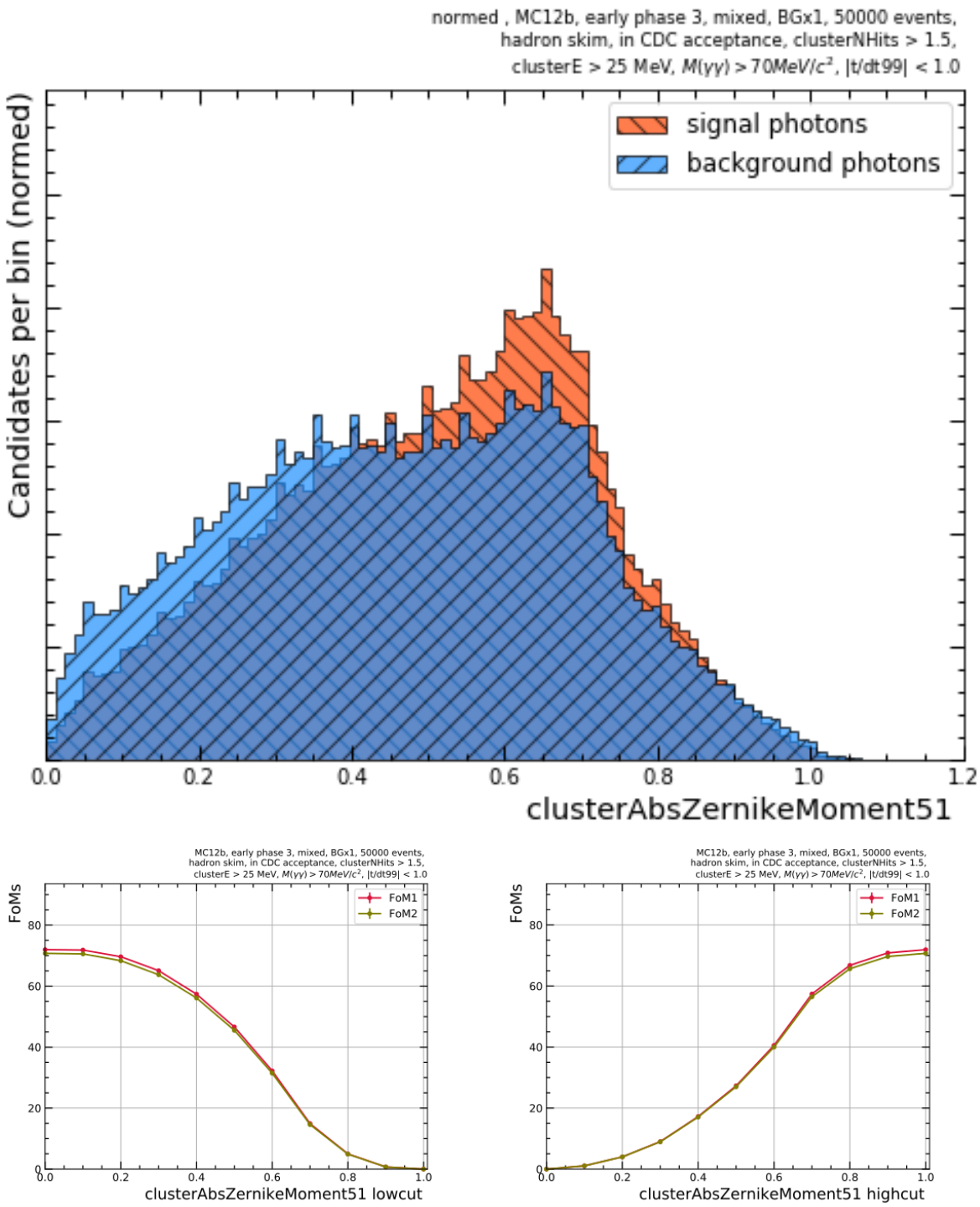

FIGURE A.9. Signal and background distributions for clusterAbsZernikeMoment51 (top). Figure of merits for clusterAbsZernikeMoment51 lowcuts (bottom left) and highcuts (bottom right).

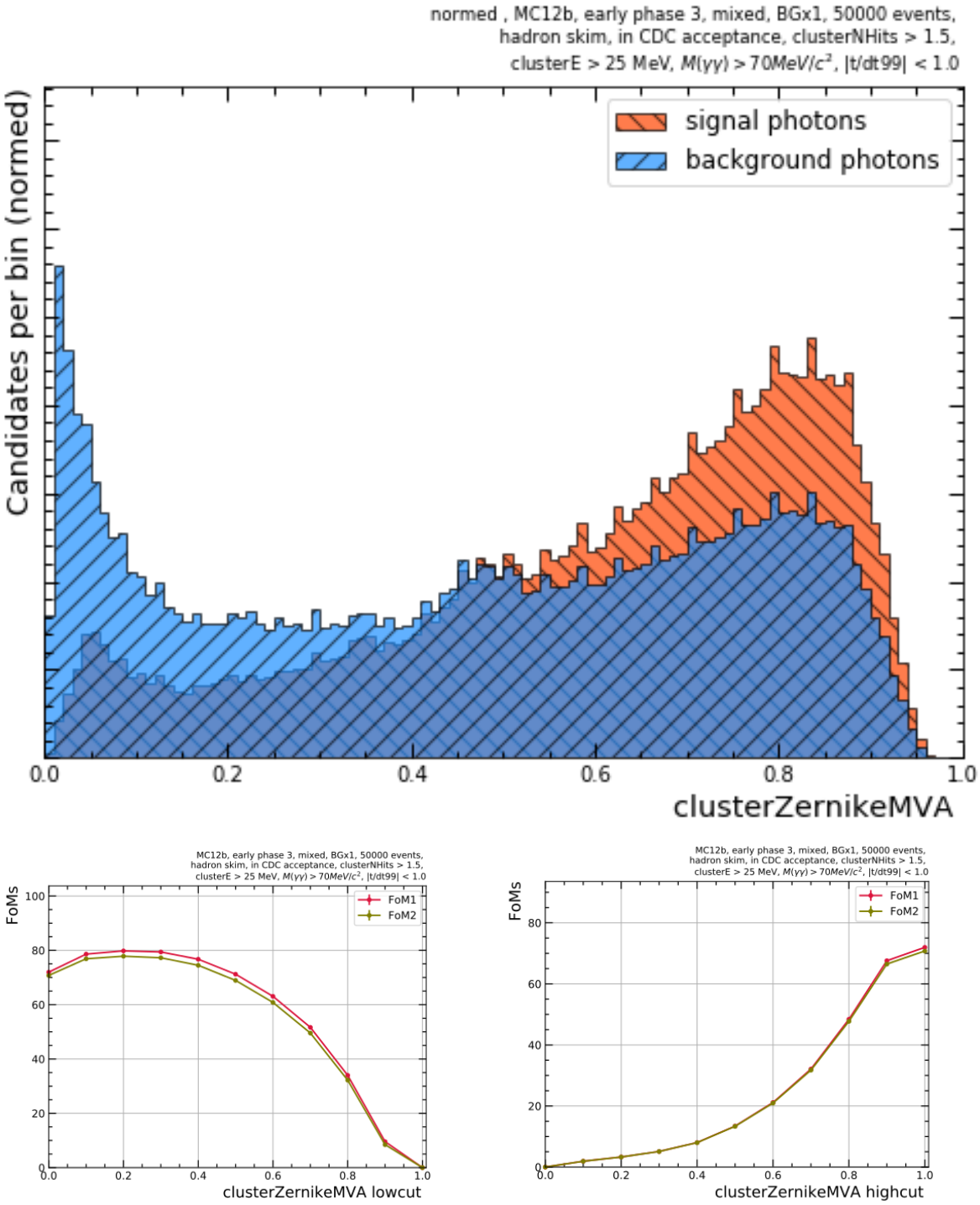

FIGURE A.10. Signal and background distributions for clusterZernikeMVA (top). Figure of merits for clusterZernikeMVA lowcuts (bottom left) and highcuts (bottom right).

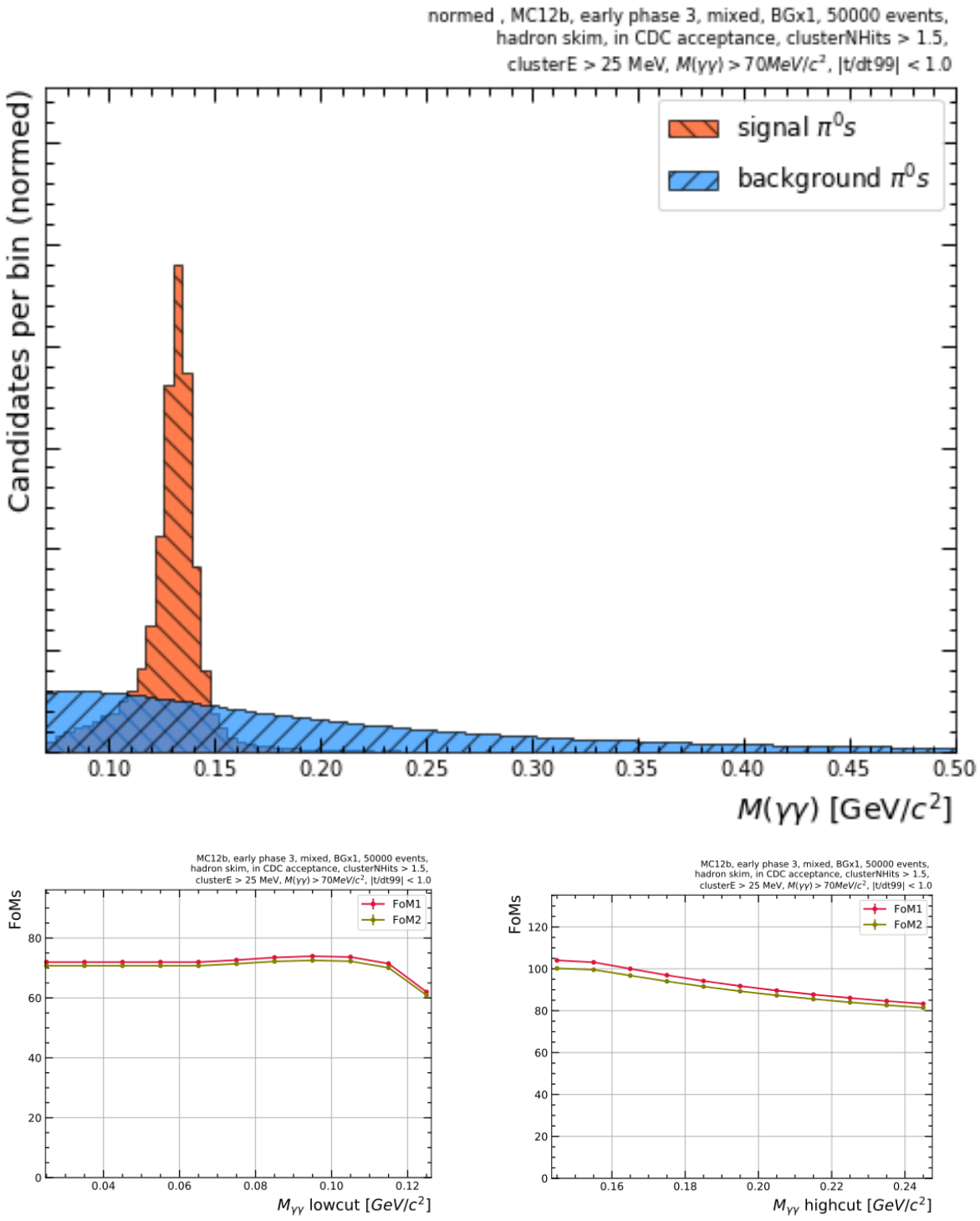

FIGURE A.11. Signal and background distributions for InvM (top). Figure of merits for InvM lowcuts (bottom left) and highcuts (bottom right).

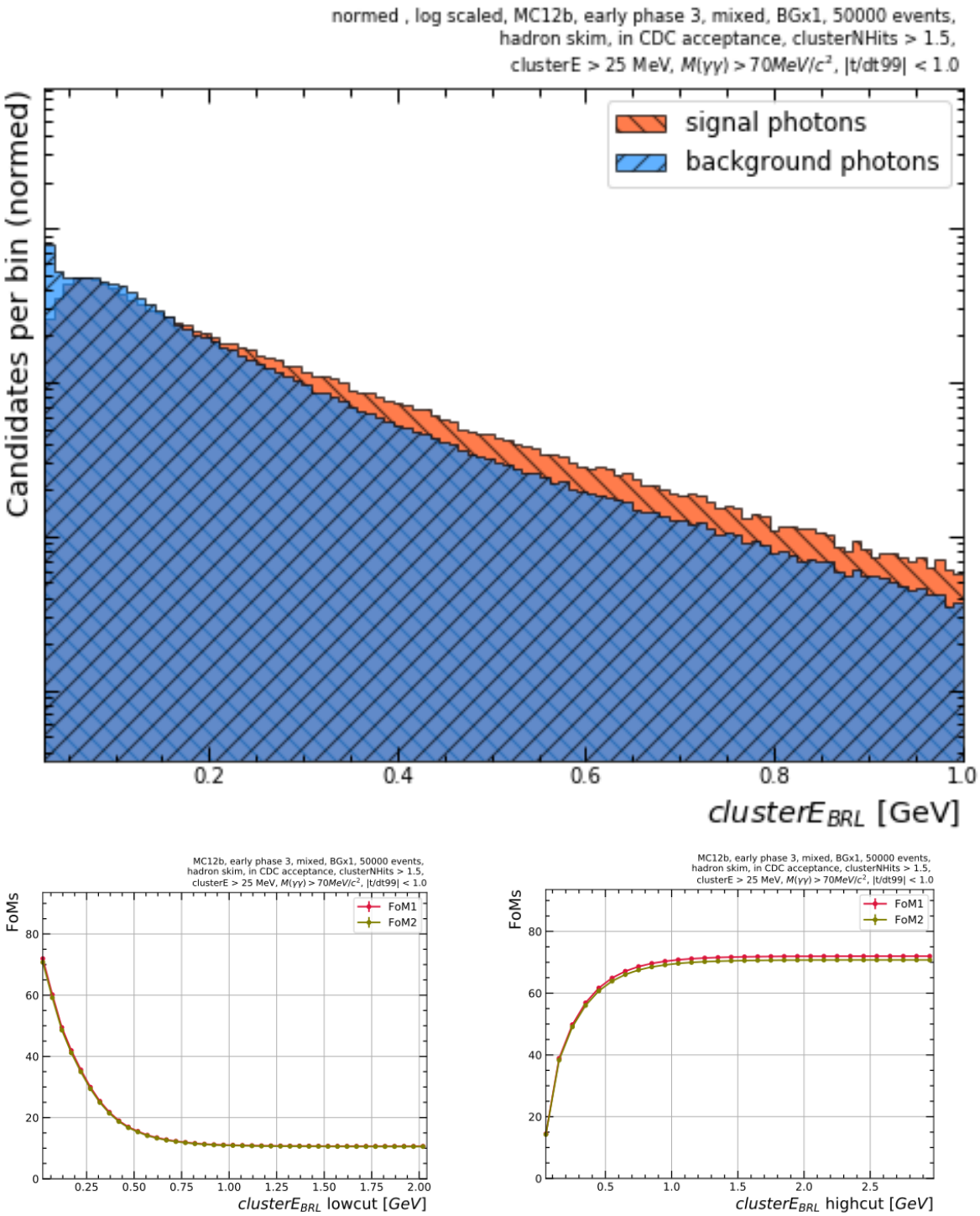

FIGURE A.12. Signal and background distributions for E_{BRL} (top). Figure of merits for E_{BRL} lowcuts (bottom left) and highcuts (bottom right).

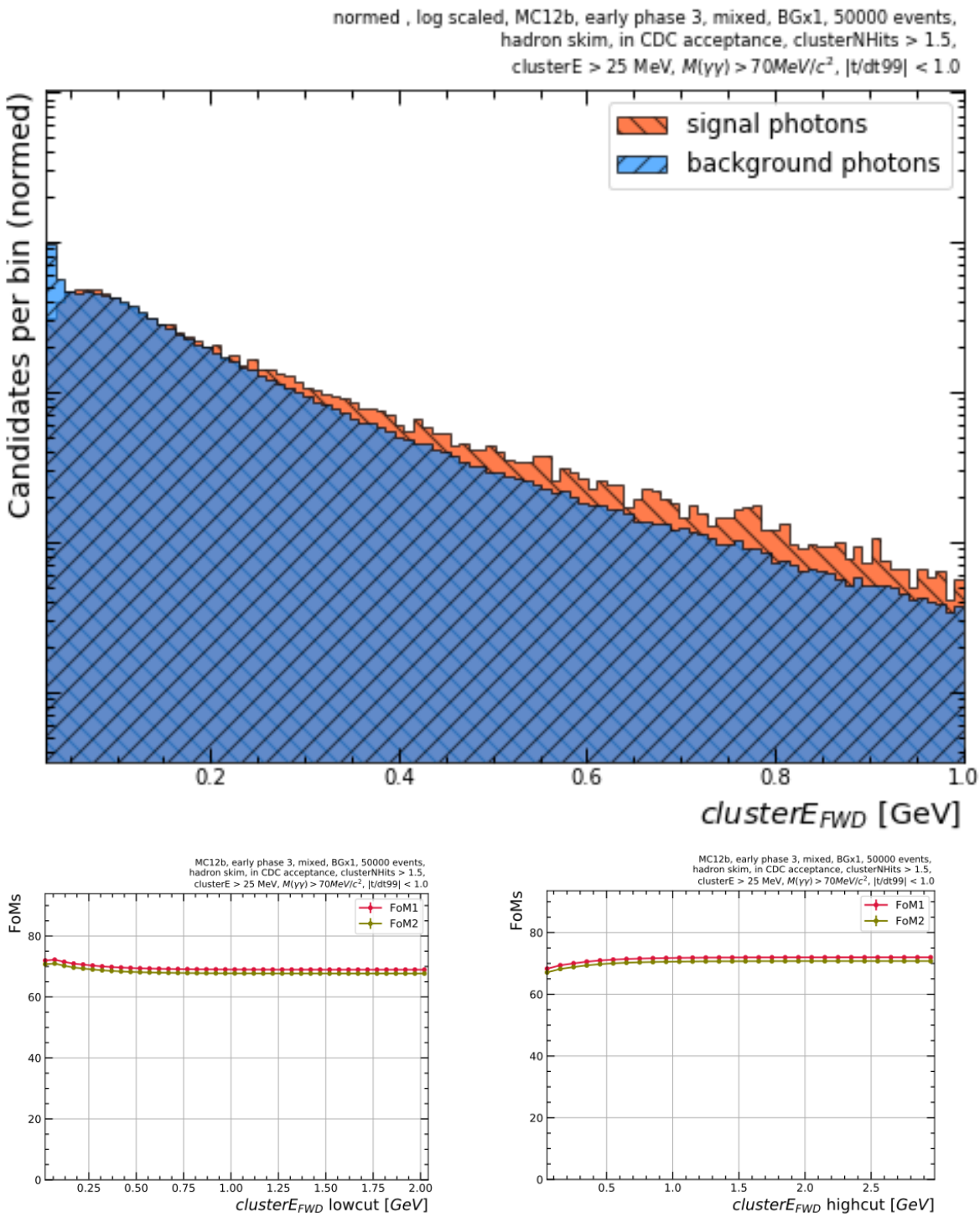

FIGURE A.13. Signal and background distributions for E_{FWD} (top). Figure of merits for E_{FWD} lowcuts (bottom left) and highcuts (bottom right).

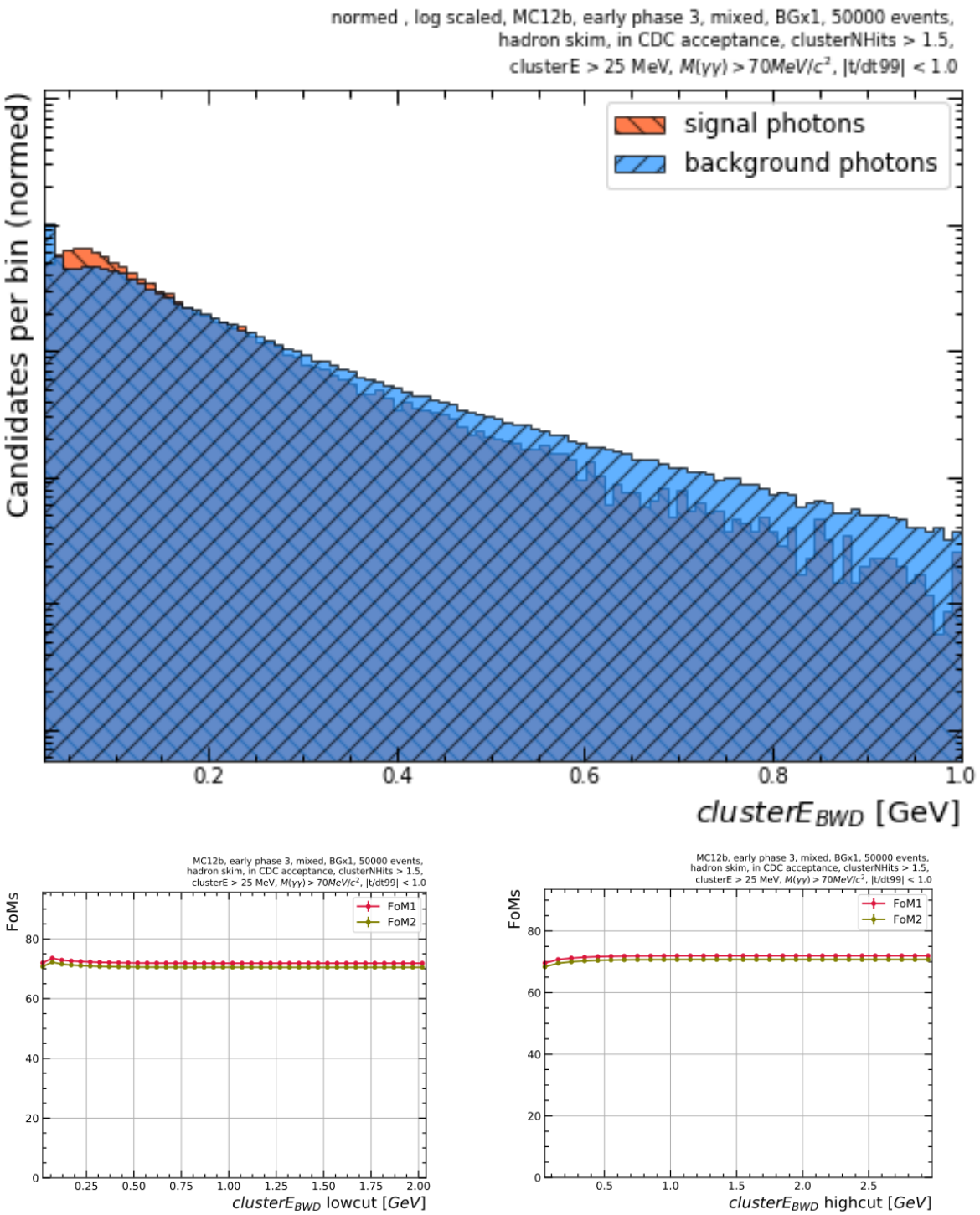

FIGURE A.14. Signal and background distributions for E_{BWD} (top). Figure of merits for E_{BWD} lowcuts (bottom left) and highcuts (bottom right).

A.2 Additional plots for Section 7.2

This Section contains the remaining plots for the comparison of data and Monte Carlo in Section 7.2. The plots for the missing variables (clusterE9E21, clusterLAT, clusterAbsZernikeMoment40, clusterAbsZernikeMoment51, and clusterZernikeMVA) for the eff30 suggestion are shown in Section A.2.1. The Sections A.2.5, A.2.4, A.2.3, and A.2.2 provide all the plots for the eff50, eff40, eff20, and eff10 suggestions, respectively.

A.2.1 eff30 suggestion plots

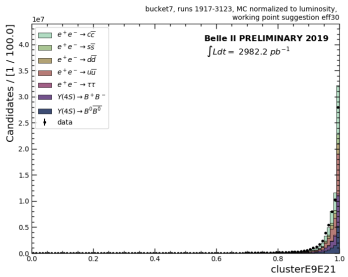

FIGURE A.15. Comparison of data and Monte Carlo for the clusterE9E21 distribution for the eff30 suggestion. Monte Carlo is normalized to data luminosity.

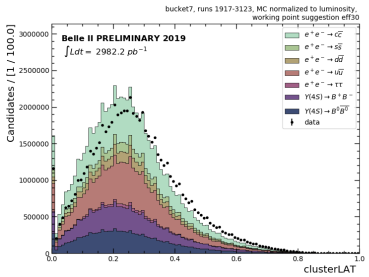

FIGURE A.16. Comparison of data and Monte Carlo for the clusterLAT distribution for the eff30 suggestion. Monte Carlo is normalized to data luminosity.

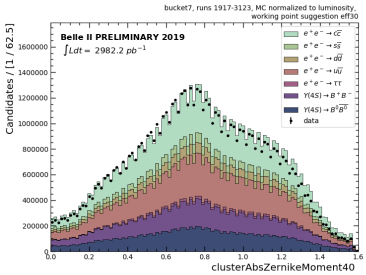

FIGURE A.17. Comparison of data and Monte Carlo for the clusterAbsZernikeMoment40 distribution for the eff30 suggestion. Monte Carlo is normalized to data luminosity.

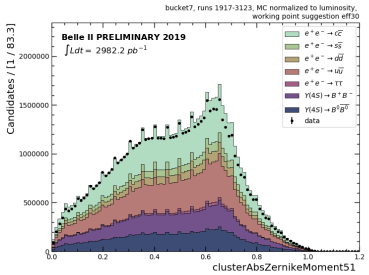

FIGURE A.18. Comparison of data and Monte Carlo for the clusterAbsZernikeMoment51 distribution for the eff30 suggestion. Monte Carlo is normalized to data luminosity.

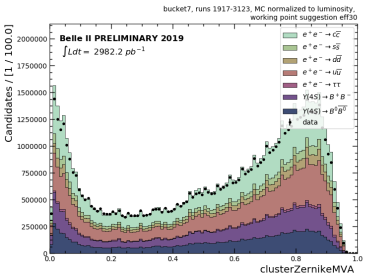

FIGURE A.19. Comparison of data and Monte Carlo for the clusterZernikeMVA distribution for the eff30 suggestion. Monte Carlo is normalized to data luminosity.

A.2.2 eff10 suggestion plots

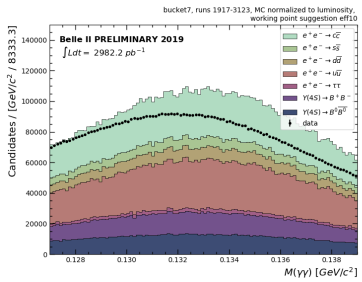

FIGURE A.20. Comparison of data and Monte Carlo for the InvM distribution for the eff10 suggestion. Monte Carlo is normalized to data luminosity.

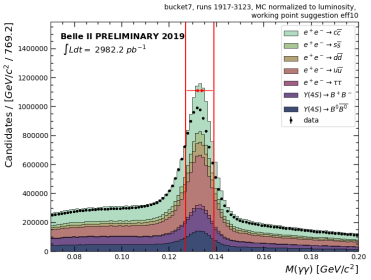

FIGURE A.21. Comparison of data and Monte Carlo for the InvM distribution for the eff10 suggestion (broader range). The InvM window of the selection is annotated in red. Monte Carlo is normalized to data luminosity.

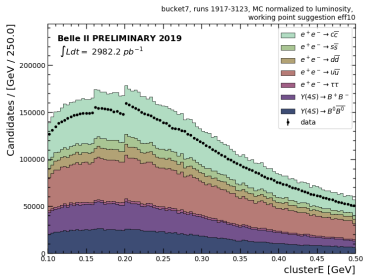

FIGURE A.22. Comparison of data and Monte Carlo for the clusterE distribution for the eff10 suggestion. Monte Carlo is normalized to data luminosity.

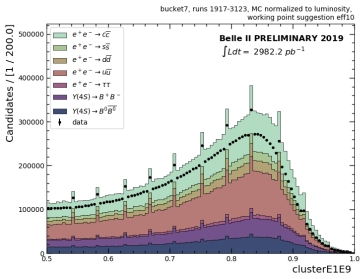

FIGURE A.23. Comparison of data and Monte Carlo for the clusterE1E9 distribution for the eff10 suggestion. Monte Carlo is normalized to data luminosity.

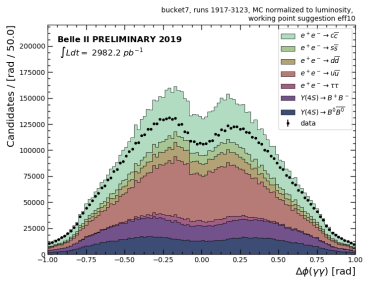

FIGURE A.24. Comparison of data and Monte Carlo for the GammasDeltaPhi distribution for the eff10 suggestion. Monte Carlo is normalized to data luminosity.

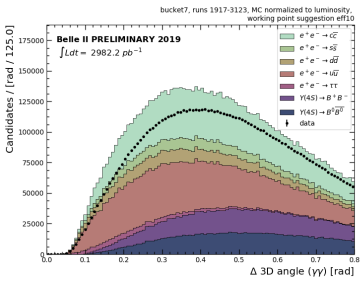

FIGURE A.25. Comparison of data and Monte Carlo for the GammasDelta3D distribution for the eff10 suggestion. Monte Carlo is normalized to data luminosity.

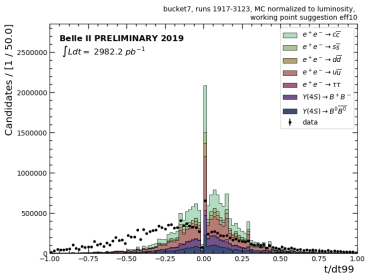

FIGURE A.26. Comparison of data and Monte Carlo for the ToDT distribution for the eff10 suggestion. Monte Carlo is normalized to data luminosity.

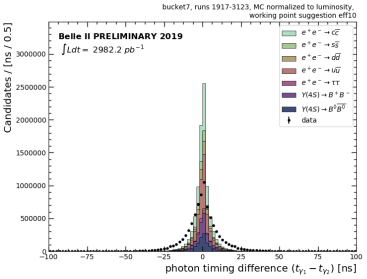

FIGURE A.27. Comparison of data and Monte Carlo for the PTD distribution for the eff10 suggestion. Monte Carlo is normalized to data luminosity.

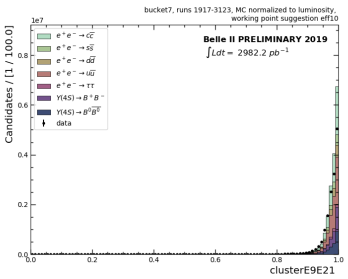

FIGURE A.28. Comparison of data and Monte Carlo for the clusterE9E21 distribution for the eff10 suggestion. Monte Carlo is normalized to data luminosity.

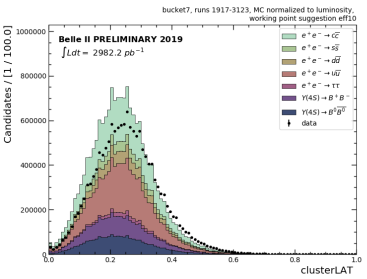

FIGURE A.29. Comparison of data and Monte Carlo for the clusterLAT distribution for the eff10 suggestion. Monte Carlo is normalized to data luminosity.

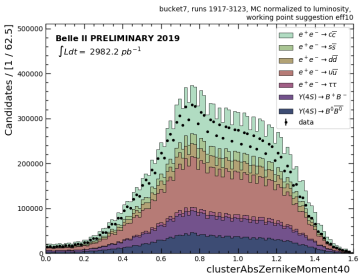

FIGURE A.30. Comparison of data and Monte Carlo for the clusterAbsZernikeMoment40 distribution for the eff10 suggestion. Monte Carlo is normalized to data luminosity.

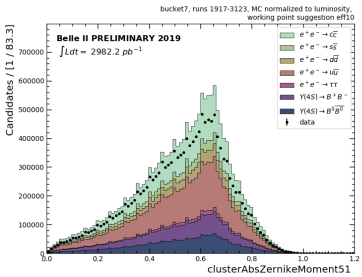

FIGURE A.31. Comparison of data and Monte Carlo for the clusterAbsZernikeMoment51 distribution for the eff10 suggestion. Monte Carlo is normalized to data luminosity.

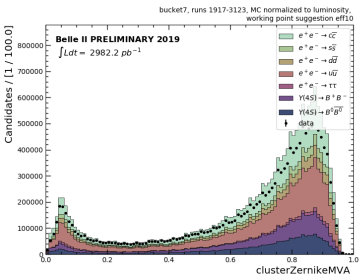

FIGURE A.32. Comparison of data and Monte Carlo for the clusterZernikeMVA distribution for the eff10 suggestion. Monte Carlo is normalized to data luminosity.

A.2.3 eff20 suggestion plots

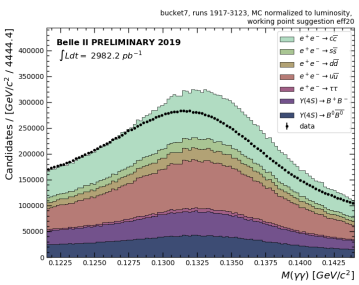

FIGURE A.33. Comparison of data and Monte Carlo for the InvM distribution for the eff20 suggestion. Monte Carlo is normalized to data luminosity.

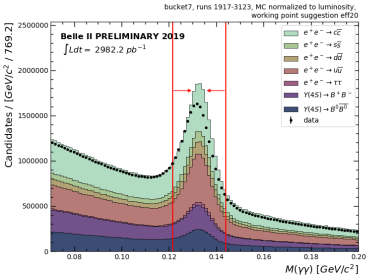

FIGURE A.34. Comparison of data and Monte Carlo for the InvM distribution for the eff20 suggestion (broader range). The InvM window of the selection is annotated in red. Monte Carlo is normalized to data luminosity.

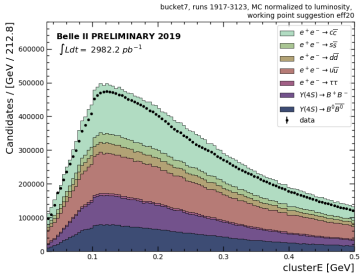

FIGURE A.35. Comparison of data and Monte Carlo for the clusterE distribution for the eff20 suggestion. Monte Carlo is normalized to data luminosity.

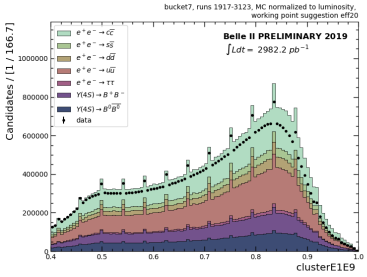

FIGURE A.36. Comparison of data and Monte Carlo for the clusterE1E9 distribution for the eff20 suggestion. Monte Carlo is normalized to data luminosity.

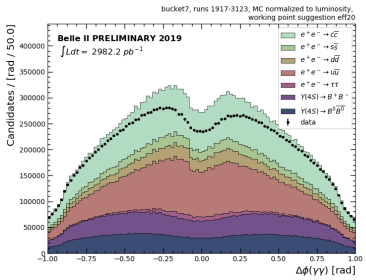

FIGURE A.37. Comparison of data and Monte Carlo for the Gammas-DeltaPhi distribution for the eff20 suggestion. Monte Carlo is normalized to data luminosity.

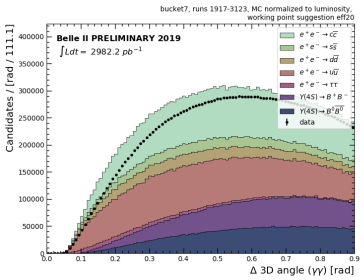

FIGURE A.38. Comparison of data and Monte Carlo for the Gammas-Delta3D distribution for the eff20 suggestion. Monte Carlo is normalized to data luminosity.

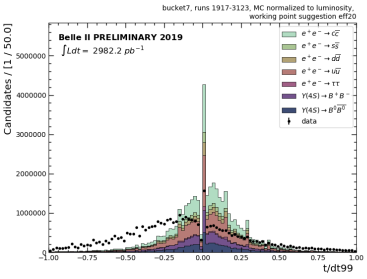

FIGURE A.39. Comparison of data and Monte Carlo for the ToDT distribution for the eff20 suggestion. Monte Carlo is normalized to data luminosity.

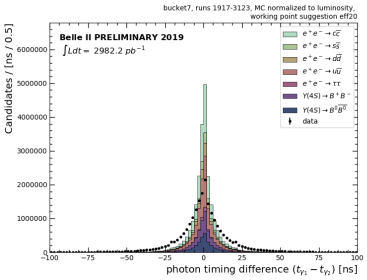

FIGURE A.40. Comparison of data and Monte Carlo for the PTD distribution for the eff20 suggestion. Monte Carlo is normalized to data luminosity.

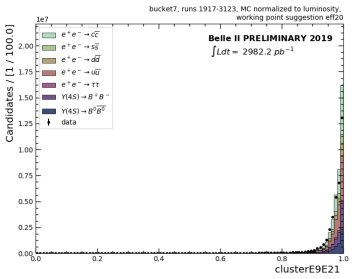

FIGURE A.41. Comparison of data and Monte Carlo for the clusterE9E21 distribution for the eff20 suggestion. Monte Carlo is normalized to data luminosity.

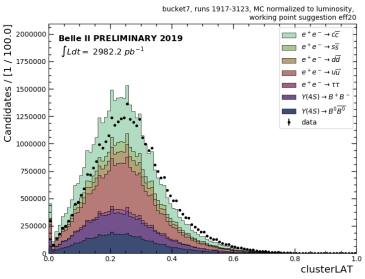

FIGURE A.42. Comparison of data and Monte Carlo for the clusterLAT distribution for the eff20 suggestion. Monte Carlo is normalized to data luminosity.

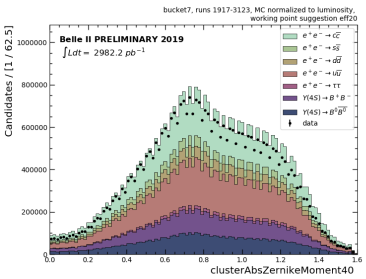

FIGURE A.43. Comparison of data and Monte Carlo for the clusterAbsZernikeMoment40 distribution for the eff20 suggestion. Monte Carlo is normalized to data luminosity.

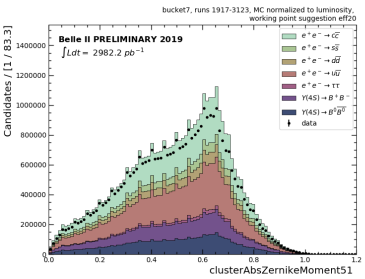

FIGURE A.44. Comparison of data and Monte Carlo for the clusterAbsZernikeMoment51 distribution for the eff20 suggestion. Monte Carlo is normalized to data luminosity.

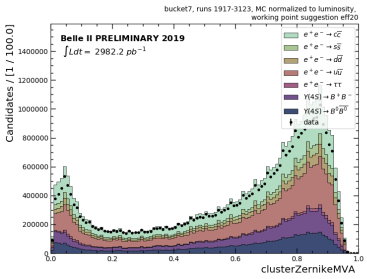

FIGURE A.45. Comparison of data and Monte Carlo for the clusterZernikeMVA distribution for the eff20 suggestion. Monte Carlo is normalized to data luminosity.

A.2.4 eff40 suggestion plots

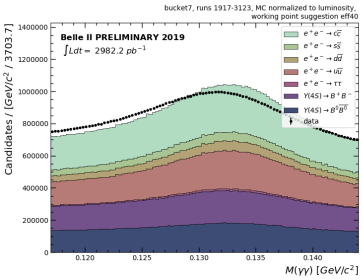

FIGURE A.46. Comparison of data and Monte Carlo for the InvM distribution for the eff40 suggestion. Monte Carlo is normalized to data luminosity.

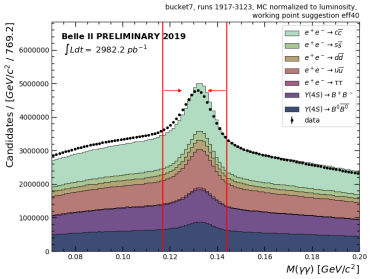

FIGURE A.47. Comparison of data and Monte Carlo for the InvM distribution for the eff40 suggestion (broader range). The InvM window of the selection is annotated in red. Monte Carlo is normalized to data luminosity.

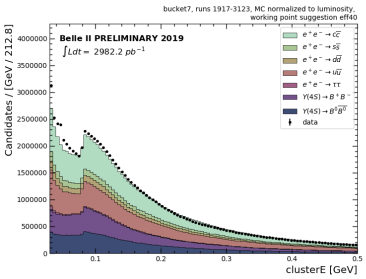

FIGURE A.48. Comparison of data and Monte Carlo for the clusterE distribution for the eff40 suggestion. Monte Carlo is normalized to data luminosity.

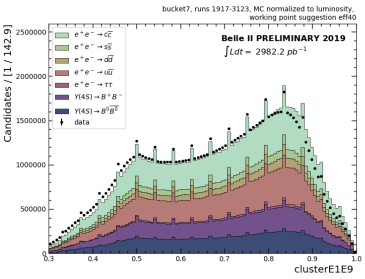

FIGURE A.49. Comparison of data and Monte Carlo for the clusterE1E9 distribution for the eff40 suggestion. Monte Carlo is normalized to data luminosity.

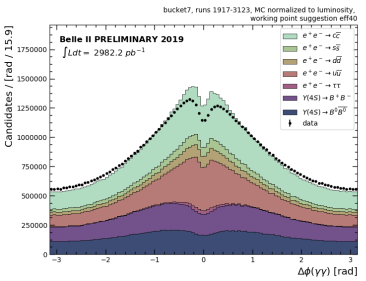

FIGURE A.50. Comparison of data and Monte Carlo for the GammasDeltaPhi distribution for the eff40 suggestion. Monte Carlo is normalized to data luminosity.

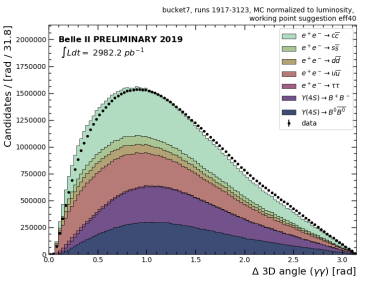

FIGURE A.51. Comparison of data and Monte Carlo for the GammasDelta3D distribution for the eff40 suggestion. Monte Carlo is normalized to data luminosity.

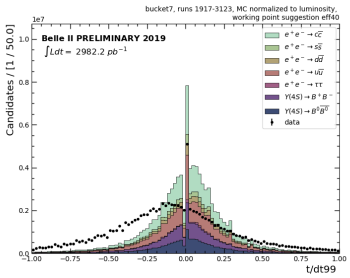

FIGURE A.52. Comparison of data and Monte Carlo for the ToDT distribution for the eff40 suggestion. Monte Carlo is normalized to data luminosity.

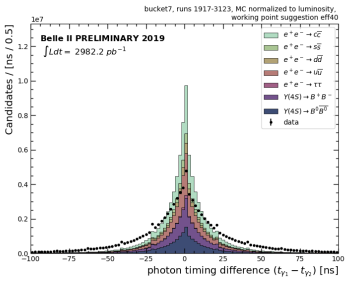

FIGURE A.53. Comparison of data and Monte Carlo for the PTD distribution for the eff40 suggestion. Monte Carlo is normalized to data luminosity.

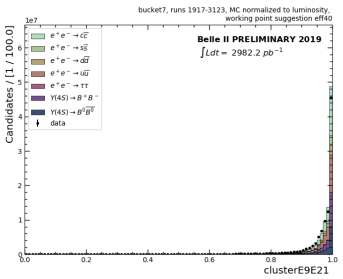

FIGURE A.54. Comparison of data and Monte Carlo for the clusterE9E21 distribution for the eff40 suggestion. Monte Carlo is normalized to data luminosity.

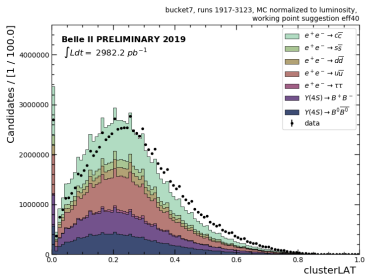

FIGURE A.55. Comparison of data and Monte Carlo for the clusterLAT distribution for the eff40 suggestion. Monte Carlo is normalized to data luminosity.

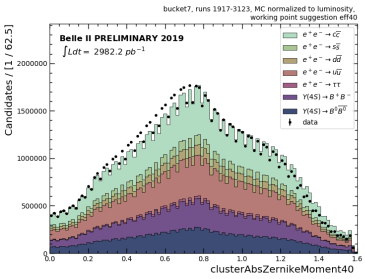

FIGURE A.56. Comparison of data and Monte Carlo for the clusterAbsZernikeMoment40 distribution for the eff40 suggestion. Monte Carlo is normalized to data luminosity.

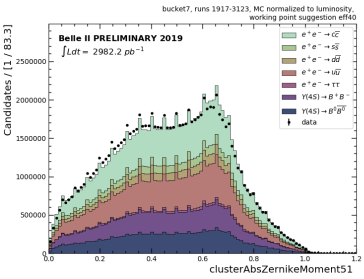

FIGURE A.57. Comparison of data and Monte Carlo for the clusterAbsZernikeMoment51 distribution for the eff40 suggestion. Monte Carlo is normalized to data luminosity.

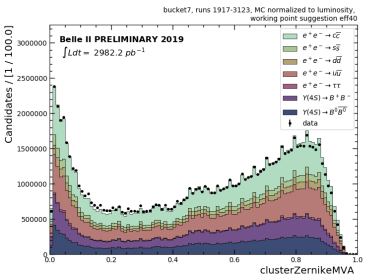

FIGURE A.58. Comparison of data and Monte Carlo for the clusterZernikeMVA distribution for the eff40 suggestion. Monte Carlo is normalized to data luminosity.

A.2.5 eff50 suggestion plots

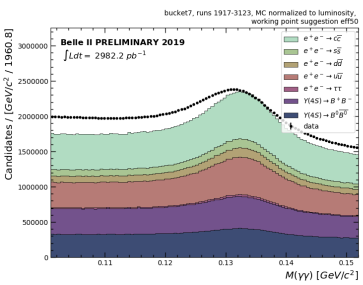

FIGURE A.59. Comparison of data and Monte Carlo for the InvM distribution for the eff50 suggestion. Monte Carlo is normalized to data luminosity.

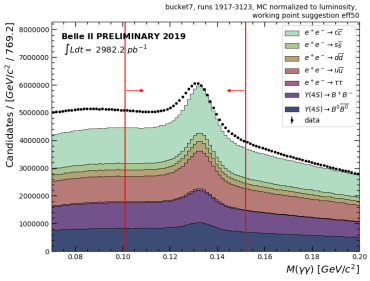

FIGURE A.60. Comparison of data and Monte Carlo for the InvM distribution for the eff50 suggestion (broader range). The InvM window of the selection is annotated in red. Monte Carlo is normalized to data luminosity.

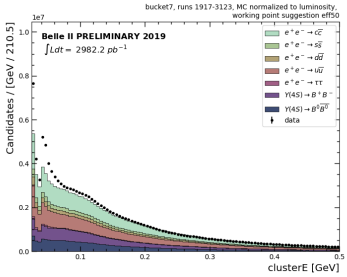

FIGURE A.61. Comparison of data and Monte Carlo for the clusterE distribution for the eff50 suggestion. Monte Carlo is normalized to data luminosity.

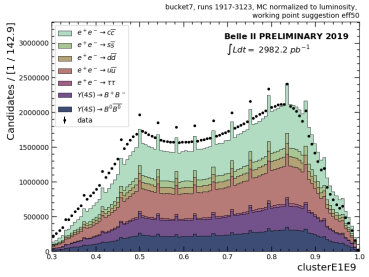

FIGURE A.62. Comparison of data and Monte Carlo for the clusterE1E9 distribution for the eff50 suggestion. Monte Carlo is normalized to data luminosity.

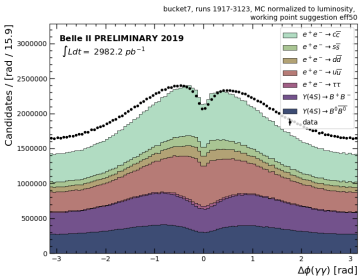

FIGURE A.63. Comparison of data and Monte Carlo for the Gammas-DeltaPhi distribution for the eff50 suggestion. Monte Carlo is normalized to data luminosity.

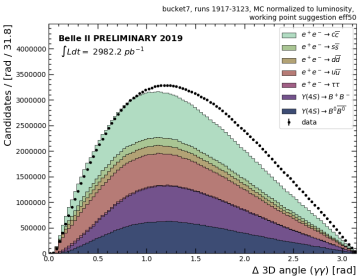

FIGURE A.64. Comparison of data and Monte Carlo for the Gammas-Delta3D distribution for the eff50 suggestion. Monte Carlo is normalized to data luminosity.

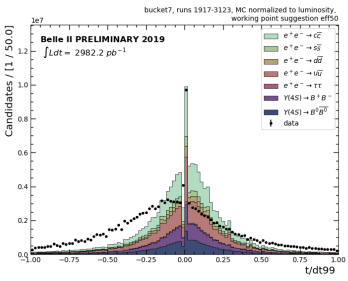

FIGURE A.65. Comparison of data and Monte Carlo for the ToDT distribution for the eff50 suggestion. Monte Carlo is normalized to data luminosity.

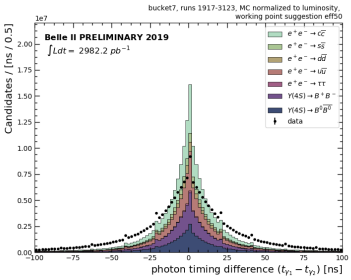

FIGURE A.66. Comparison of data and Monte Carlo for the PTD distribution for the eff50 suggestion. Monte Carlo is normalized to data luminosity.

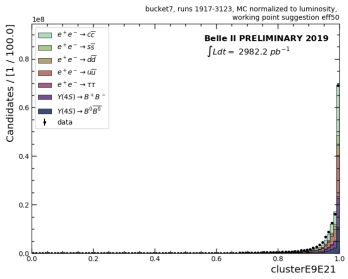

FIGURE A.67. Comparison of data and Monte Carlo for the clusterE9E21 distribution for the eff50 suggestion. Monte Carlo is normalized to data luminosity.

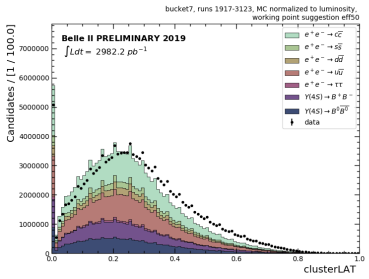

FIGURE A.68. Comparison of data and Monte Carlo for the clusterLAT distribution for the eff50 suggestion. Monte Carlo is normalized to data luminosity.

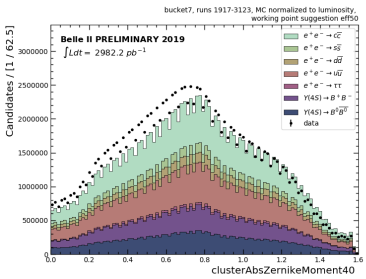

FIGURE A.69. Comparison of data and Monte Carlo for the clusterAbsZernikeMoment40 distribution for the eff50 suggestion. Monte Carlo is normalized to data luminosity.

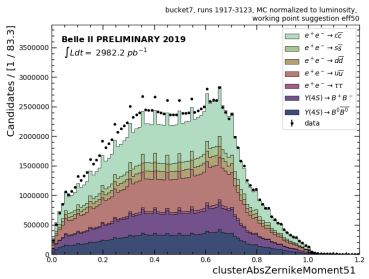

FIGURE A.70. Comparison of data and Monte Carlo for the clusterAbsZernikeMoment51 distribution for the eff50 suggestion. Monte Carlo is normalized to data luminosity.

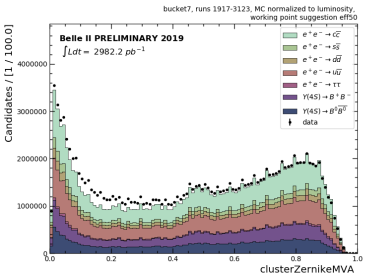

FIGURE A.71. Comparison of data and Monte Carlo for the clusterZernikeMVA distribution for the eff50 suggestion. Monte Carlo is normalized to data luminosity.

List of Figures

FIGURE **Page**

List of Tables

BIBLIOGRAPHY

[1] Pauline Gagnon.
The standard model: a beautiful but flawed theory.
https://www.quantumdiaries.org/2014/03/14/the-standard-model-a-beautiful-but-flawed-theory/
February 2019.

[2] Ahmed Ali, Christian Hambrock, and M. Jamil Aslam.
Tetraquark interpretation of the belle data on the anomalous $\Upsilon(1s)\pi^+\pi^-$ and $\Upsilon(2s)\pi^+\pi^-$ production near the $\Upsilon(5s)$ resonance.
Phys. Rev. Lett., 104:162001, Apr 2010.

[3] Amplitude analysis of $B^+ \to J/\psi\phi K^+$ decays.
Phys. Rev. D, 95:012002, Jan 2017.

[4] Observation of $J/\psi\phi$ structures consistent with exotic states from amplitude analysis of $B^+ \to J/\psi\phi K^+$ decays.
Phys. Rev. Lett., 118:022003, Jan 2017.

[5] Observation of $J/\psi p$ resonances consistent with pentaquark states in $\Lambda_b^0 \to J/\psi K^- p$ decays.
Phys. Rev. Lett., 115:072001, Aug 2015.

[6] V. C. Rubin, N. Thonnard, and W. K. Ford, Jr.
Rotational properties of 21 SC galaxies with a large range of luminosities and radii, from NGC 4605 /R = 4kpc/ to UGC 2885 /R = 122 kpc/.
Astrophys. J., 238:471, 1980.

[7] Vera C. Rubin and W. Kent Ford, Jr.
Rotation of the Andromeda Nebula from a Spectroscopic Survey of Emission Regions.
Astrophys. J., 159:379–403, 1970.

[8] Douglas Clowe, Marusa Bradac, Anthony H. Gonzalez, Maxim Markevitch, Scott W. Randall, Christine Jones, and Dennis Zaritsky.
A direct empirical proof of the existence of dark matter.
Astrophys. J., 648:L109–L113, 2006.

[9] Gianfranco Bertone.
Particle Dark Matter.
Cambridge University Press, 1 edition, 2010.

[10] Roberto D. Peccei.
The Strong CP Problem and Axions, pages 3–17.
Springer Berlin Heidelberg, Berlin, Heidelberg, 2008.

[11] M. Drewes.
The Phenomenology of Right Handed Neutrinos.
International Journal of Modern Physics E, 22:1330019–593, August 2013.

[12] J. H. Christenson, J. W. Cronin, V. L. Fitch, and R. Turlay.
Evidence for the 2π decay of the K_2^0 meson.
Phys. Rev. Lett., 13:138–140, Jul 1964.

[13] P. J. Clark.
CP violation in B decays at the BABAR experiment.
In *Proceedings, 24th International Workshop on Fundamental Problems of High Energy Physics and Field Theory: Protvino, Russia, June 27-29, 2001*, pages 54–60, 2001.

[14] Kazuo Abe et al.
Observation of large CP violation in the neutral B meson system.
Phys. Rev. Lett., 87:091802, 2001.

[15] Kazuo Abe et al.
An Improved measurement of mixing induced CP violation in the neutral B meson system.
Phys. Rev., D66:071102, 2002.

[16] K. Prasanth.
CP violation in D meson decays at Belle.
EPJ Web Conf., 164:07008, 2017.

[17] T. Abe et al.
Belle II Technical Design Report.
2010.

[18] KEK HIGH ENERGY ACCELERATOR RESEARCH ORGANIZATION.
Official website.
`http://www-superkekb.kek.jp/img/ProjectedLuminosity_v20190128.png`, Octobre 2019.

[19] P. M. Lewis et al.

First Measurements of Beam Backgrounds at SuperKEKB.
Nucl. Instrum. Meth., A914:69–144, 2019.

[20] W. Altmannshofer et al.
The Belle II Physics Book.
2018.

[21] Torben Ferber.
Electromagnetic calorimeter reconstruction in belle ii.
https://indico.cern.ch/event/708041/contributions/3269704/attachments/1809200/2954059/2019_03_11_acat_ferber_final.pdf.

[22] Hitomi Ikeda.
Development of the CsI(Tl) Calorimeter for the Measurement of CP Violation at KEK B-Factory.
PhD thesis, Nara Women's University, 01 1999.

[23] V. E. Shebalin.
Electromagnetic Calorimeter of the Belle-II Detector.
Phys. Part. Nucl., 49(4):793–798, 2018.

[24] Belle-ECL, V Aulchenko, A Bobrov, A Bondar, B G Cheon, S Eidelman, D Epifanov, Yu Garmash, Y M Goh, S H Kim, P Krokovny, A Kuzmin, I S Lee, D Matvienko, K Miyabayashi, I Nakamura, V Shebalin, B Shwartz, Y Unno, Yu Usov, A Vinokurova, V Vorobjev, V Zhilich, and V Zhulanov.
Electromagnetic calorimeter for belle II.
Journal of Physics: Conference Series, 587:012045, feb 2015.

[25] B. Shwartz and.
Electromagnetic calorimeter of the belle II detector.
Journal of Physics: Conference Series, 928:012021, nov 2017.

[26] Nils Lennart Braun.
Combinatorial Kalman Filter and High Level Trigger Reconstruction for the Belle II Experiment.
PhD thesis, Karlsruher Institut für Technologie (KIT), 12 2018.

[27] Torben Ferber.
Tutorial: The belle ii electromagnetic calorimeter.
https://confluence.desy.de/display/~scunliff/DESY+Local+Tutorial?preview=/109161565/109161569/2018_11_25_DESY_ferber.pdf.

[28] Torben Ferber and Christopher Hearty.
Design of the ecl software for belle ii.
internal BELLE2-NOTE-TE-2016-001, 2 2016.

[29] The Belle II Collaboration.
Basf2 (belle analysis framework 2), copyright(c) 2016 belle ii collaboration.
`https://stash.desy.de/projects/B2/repos/software/browse/mdst/dataobjects/include/ECLCluster.h`, 2019.

[30] Torben Ferber Alon Hershenhorn and Christopher Hearty.
Ecl shower shape variables based on zernike moments.
internal BELLE2-NOTE-TE-2017-001, 1 2017.

[31] Sarah Pohl.
Track Reconstruction at the First Level Trigger of the Belle II Experiment.
PhD thesis, Ludwig-Maximilians-Universitaet Muenchen, 12 2017.

[32] M. Tanabashi, K. Hagiwara, K. Hikasa, K. Nakamura, Y. Sumino, F. Takahashi, J. Tanaka, K. Agashe, G. Aielli, C. Amsler, M. Antonelli, D. M. Asner, H. Baer, Sw. Banerjee, R. M. Barnett, T. Basaglia, C. W. Bauer, J. J. Beatty, V. I. Belousov, J. Beringer, S. Bethke, A. Bettini, H. Bichsel, O. Biebel, K. M. Black, E. Blucher, O. Buchmuller, V. Burkert, M. A. Bychkov, R. N. Cahn, M. Carena, A. Ceccucci, A. Cerri, D. Chakraborty, M.-C. Chen, R. S. Chivukula, G. Cowan, O. Dahl, G. D'Ambrosio, T. Damour, D. de Florian, A. de Gouvêa, T. DeGrand, P. de Jong, G. Dissertori, B. A. Dobrescu, M. D'Onofrio, M. Doser, M. Drees, H. K. Dreiner, D. A. Dwyer, P. Eerola, S. Eidelman, J. Ellis, J. Erler, V. V. Ezhela, W. Fetscher, B. D. Fields, R. Firestone, B. Foster, A. Freitas, H. Gallagher, L. Garren, H.-J. Gerber, G. Gerbier, T. Gershon, Y. Gershtein, T. Gherghetta, A. A. Godizov, M. Goodman, C. Grab, A. V. Gritsan, C. Grojean, D. E. Groom, M. Grünewald, A. Gurtu, T. Gutsche, H. E. Haber, C. Hanhart, S. Hashimoto, Y. Hayato, K. G. Hayes, A. Hebecker, S. Heinemeyer, B. Heltsley, J. J. Hernández-Rey, J. Hisano, A. Höcker, J. Holder, A. Holtkamp, T. Hyodo, K. D. Irwin, K. F. Johnson, M. Kado, M. Karliner, U. F. Katz, S. R. Klein, E. Klempt, R. V. Kowalewski, F. Krauss, M. Kreps, B. Krusche, Yu. V. Kuyanov, Y. Kwon, O. Lahav, J. Laiho, J. Lesgourgues, A. Liddle, Z. Ligeti, C.-J. Lin, C. Lippmann, T. M. Liss, L. Littenberg, K. S. Lugovsky, S. B. Lugovsky, A. Lusiani, Y. Makida, F. Maltoni, T. Mannel, A. V. Manohar, W. J. Marciano, A. D. Martin, A. Masoni, J. Matthews, U.-G. Meißner, D. Milstead, R. E. Mitchell, K. Mönig, P. Molaro, F. Moortgat, M. Moskovic, H. Murayama, M. Narain, P. Nason, S. Navas, M. Neubert, P. Nevski, Y. Nir, K. A. Olive, S. Pagan Griso, J. Parsons, C. Patrignani, J. A. Peacock, M. Pennington, S. T. Petcov, V. A. Petrov, E. Pianori, A. Piepke, A. Pomarol, A. Quadt, J. Rademacker, G. Raffelt, B. N. Ratcliff, P. Richardson, A. Ringwald, S. Roesler, S. Rolli, A. Romaniouk, L. J. Rosenberg, J. L. Rosner, G. Rybka, R. A. Ryutin, C. T. Sachrajda, Y. Sakai, G. P.

Salam, S. Sarkar, F. Sauli, O. Schneider, K. Scholberg, A. J. Schwartz, D. Scott, V. Sharma, S. R. Sharpe, T. Shutt, M. Silari, T. Sjöstrand, P. Skands, T. Skwarnicki, J. G. Smith, G. F. Smoot, S. Spanier, H. Spieler, C. Spiering, A. Stahl, S. L. Stone, T. Sumiyoshi, M. J. Syphers, K. Terashi, J. Terning, U. Thoma, R. S. Thorne, L. Tiator, M. Titov, N. P. Tkachenko, N. A. Törnqvist, D. R. Tovey, G. Valencia, R. Van de Water, N. Varelas, G. Venanzoni, L. Verde, M. G. Vincter, P. Vogel, A. Vogt, S. P. Wakely, W. Walkowiak, C. W. Walter, D. Wands, D. R. Ward, M. O. Wascko, G. Weiglein, D. H. Weinberg, E. J. Weinberg, M. White, L. R. Wiencke, S. Willocq, C. G. Wohl, J. Womersley, C. L. Woody, R. L. Workman, W.-M. Yao, G. P. Zeller, O. V. Zenin, R.-Y. Zhu, S.-L. Zhu, F. Zimmermann, P. A. Zyla, J. Anderson, L. Fuller, V. S. Lugovsky, and P. Schaffner.
Review of particle physics.
Phys. Rev. D, 98:030001, Aug 2018.

[33] R. Miskimen.
Neutral pion decay.
Annual Review of Nuclear and Particle Science, 61(1):1–21, 2011.

[34] Statsoft.
Inc. (2013). electronic statistics textbook. tulsa.
`http://www.statsoft.com/textbook/`, Octobre 2019.

[35] Wikipedia.
Pearson correlation coefficient.
`https://en.wikipedia.org/wiki/Pearson_correlation_coefficient`, Octobre 2019.

[36] Torben Ferber Phillip Urquijo.
Overview of the belle ii physics generators.
internal BELLE2-NOTE-PH-2015-006, 3 2016.

DANKSAGUNG

Zuallererst möchte ich mich bei Prof. Dr. Concettina Sfienti, Dr. Carsten Niebuhr und Dr. Torben Ferber für die Möglichkeit bedanken, meine Masterarbeit als externe Arbeit am DESY Hamburg verfassen zu können. Das Jahr am DESY hat mich fachlich und persönlich immens wachsen lassen und ich werde noch lange auf diese schöne und lehrreiche Zeit zurückblicken.

Einen besonderen Dank möchte ich an dieser Stelle Torben aussprechen, der mir als Zweitgutachter und Büronachbar immer mit Rat und Tat zur Seite stand. Auf jede noch so kleine Frage wusstest Du mit Geduld und Expertise zu antworten. Vielen, vielen Dank!

Ein großes Dankeschön geht außerdem an die Belle II ECL-Gruppe am DESY, namentlich Dr. Torben Ferber, Dr. Nataliia Kovalchuk, Dr. Sam Cunliffe, Dr. Yu Hu, Michael De Nuccio, Abtin Narimani und Cedric Ly. Danke für die herzliche und lockere Atmosphäre, danke für Eure Hilfsbereitschaft und Unterstützung bei Fragen und Problemen, danke, danke, danke.

Hervorheben möchte ich hierbei Sam und Michael. Eure Hilfe habe ich besonders oft in Anspruch genommen. Vielen Dank, dass Ihr Euch immer Zeit genommen habt, auch für das Korrekturlesen von Teilen dieser Arbeit!

Zuguterletzt möchte ich mich bei meinen Eltern und Großeltern bedanken, auf deren uneingeschränkte Unterstützung ich mich vor und während der Zeit meines Studiums immer verlassen konnte. Ohne Eure Hilfe wären mein Studium und diese Arbeit nicht möglich gewesen.